DESIGN AND ANALYSIS OF FINITE ARRAYS OF CIRCUMFERENTIALLY ORIENTED PRINTED DIPOLES ON ELECTRICALLY LARGE COATED CYLINDERS

A THESIS

SUBMITTED TO THE DEPARTMENT OF ELECTRICAL AND

ELECTRONICS ENGINEERING

AND THE INSTITUTE OF ENGINEERING AND SCIENCE

OF BILKENT UNIVERSITY

IN PARTIAL FULFILLMENT OF THE REQUIREMENTS

FOR THE DEGREE OF

MASTER OF SCIENCE

By

Barış Güner

August, 2004

I certify that I have read this thesis and that in my opinion it is fully adequate, in scope and in quality, as a thesis for the degree of Master of Science.

Assist. Prof. Dr. Vakur B. Ertürk (Supervisor)

I certify that I have read this thesis and that in my opinion it is fully adequate, in scope and in quality, as a thesis for the degree of Master of Science.

Prof. Dr. Ayhan Altıntaş

I certify that I have read this thesis and that in my opinion it is fully adequate, in scope and in quality, as a thesis for the degree of Master of Science.

Assoc. Prof. Dr. Gülbin Dural

Approved for the Institute of Engineering and Science:

Prof. Dr. Mehmet B. Baray
Director of the Institute of Engineering and Science

ABSTRACT

DESIGN AND ANALYSIS OF FINITE ARRAYS OF CIRCUMFERENTIALLY ORIENTED PRINTED DIPOLES ON ELECTRICALLY LARGE COATED CYLINDERS

Barış Güner
M.S. in Electrical and Electronics Engineering
Supervisor: Assist. Prof. Dr. Vakur B. Ertürk
August, 2004

Conformal antennas and arrays are used in a wide range of applications including mobile communication systems, missiles, aircrafts and spacecrafts. In these applications, the conformality is required for aesthetic and aerodynamic constraints and reducing the radar cross-section. Antennas and arrays conformal to the cylindrical host bodies are particularly important since cylindrical geometry can be used to approximate most of the practical problems and it is a canonical geometry. However, the available design and analysis tools for antennas/arrays conformal to cylindrical host bodies are either approximate methods or restricted to small arrays. Recently, a hybrid method based on Method of Moments (MoM) combined with a Green's function in space domain is proposed to solve the aforementioned problem. In this work this method is used to analyze finite, phased arrays of circumferentially oriented printed dipoles conformal to the dielectric coated electrically large circular cylinders. The accuracy and efficiency of the method comes from the computation of the appropriate Green's function which is the kernel of the electric field integral equation to be solved via MoM. There are three different high-frequency based representations for the Green's function in the spatial domain which are valid in different but overlapping regions: Planar representation, steepest descent path (SDP) representation and the Fourier Series (FS) representation. These different representations are used interchangeably to obtain the most accurate solution that requires the least amount of computational time. Several modifications on the method are made in this work to increase the efficiency and accuracy of the solution. The effects of the array and host body parameters on the performance of the array are presented. The results are compared with a previously published spectral domain solution to show the accuracy

of the method. Also, performance comparisons with those of the cylindrical arrays of axially oriented dipoles and planar arrays are made to observe the effects of curvature and the dipole orientation on the performance of the array.

Keywords: Conformal phased arrays, Method of moments, Green's function, Coated cylinders.

ÖZET

ELEKTRİKSEL OLARAK BÜYÜK DİELEKTRİK KAPLI SİLİNDİRLER ÜZERİNDEKİ ÇEVRESEL DOĞRULTUDA FAZ DİZİLİMLİ BASKI DİPOLLERİNİN İNCELENMESİ VE TASARIMI

Barış Güner
Elektrik ve Elektronik Mühendisliği Bölümü, Yüksek Lisans
Tez Yöneticisi: Yard. Doç. Dr. Vakur B. Ertürk
Ağustos, 2004

Konformal antenler ve anten dizileri mobil iletişim sistemleri, füzeler, uçaklar ve uzay mekikleri gibi çeşitli uygulama alanlarında kullanılmaktadır. Bu uygulamalarda, estetik ve aerodinamik koşulların yerine getirilmesi ve radar kesit alanının düşürülmesi gibi amaçlarla konformal anten ve anten dizilerine ihtiyaç vardır. Silindirsel yüzeyler üzerindeki antenler ve anten dizileri pratikteki çoğu eğimli yüzeyin silindir olarak ifade edilebilmesi ve de silindir geometrisinin doğal (kanonik) bir geometri olması nedeniyle özel bir öneme sahiptir. Öte yandan, silindir yüzeyine monte edilmiş olan anten ve anten dizileri için mevcut olan tasarım ve analiz metodları ya yaklaşık tekniklerdir ya da küçük anten dizileri için geçerlidir. Buna karşılık kısa zaman önce bahsedilen problemleri çözmek üzere Momentler Metodunu (MoM) uzamsal bölgedeki Green fonksiyonu ile birleştiren karma bir metod öne sürülmüştür. Bu tezde sözü edilen karma MoM/uzamsal bölgedeki Green fonksiyonu metodu kullanılarak dielektrik kaplı dairesel silindirler üzerindeki faz dizilimli baskı dipolleri incelenmektedir. Bu metodun etkinliği ve doğruluğu momentler metoduyla çözülen integral denkleminin çekirdeğini oluşturan Green fonksiyonunun hesaplanmasına bağlıdır. Green fonksiyonunun uzamsal bölgede değişik ama kesişen bölgelerde geçerli olan üç değişik yüksek frekans tabanlı gösterimi mevcuttur: Düzlemsel gösterim, en dik eğimli yol (SDP) gösterimi ve Fourier Serisi (FS) gösterimi. Bu değişik gösterimler en doğru ve en etkin çözümü elde etmek amacıyla değişmeli olarak kullanılmaktadır. Bu çalışmada çözümün daha doğru ve etkin olması amacıyla metod üzerinde çeşitli iyileştirmeler yapılmıştır. Anten dizisinin ve üzerine monte edildiği yapının çeşitli parametrelerinin değişmesiyle sistem performansının değişimine bakılmıştır. Sonuçlar daha önce yayınlanan bir spektral

bölge methoduyla karşılaştırılarak metodun doğruluğu gösterilmiştir. Ayrıca, eksen doğrultusunda uzanan dipol anten dizileri ve düzlemsel anten dizileriyle performans karşılaştırması yapılarak kavisin ve dipol doğrultusunun anten dizisinin performansı üzerindeki etkisi incelenmiştir.

Anahtar sözcükler: Konformal faz dizilimli antenler, Momentler metodu, Green fonksiyonu, Dielektrik kaplı silindirler.

Acknowledgement

I would like to express my gratitude to Assist. Prof. Dr. Vakur B. Ertürk for his suggestions and guidance throughout the development of this thesis.

I would also like to express my thanks to Prof. Dr. Ayhan Altıntaş and Assoc. Prof. Dr. Gülbin Dural for their interest on the subject matter and accepting to read and review the thesis.

Contents

List of Figures

Chapter 1

Introduction

In the design of antennas, in addition to the the electromagnetic considerations, aerodynamic, hydrodynamic constraints as well as aesthetic worries should all be taken into account. These considerations lead to the development of conformal antennas which are defined as antennas that conform to arbitrarily-shaped host bodies. Although an arbitrarily-shaped host body term may also include a flat surface, in general the host body is assumed to be non-planar and the term "conformal" is not used for antennas on planar platforms.

Conformal antennas are used extensively in both military and civilian applications. In military applications, which include radars and shipborne, airborne and missileborne antennas, the conformality is required to reduce the radar cross section of the system, to obtain a wider scan range and to satisfy the hydrodynamic or the aerodynamic constraints. Due to the difficulties in the design and analysis of conformal antennas, most of the initial research on this field were made for military applications. However, with the emergence of powerful computers, the civilian antenna designers began to take notice of them as well. Among their other advantages, conformal antennas/arrays provide a better aesthetic look on devices which is particularly important in commercial systems. Today, they are used in a variety of civilian applications like space division multiple access (SDMA) systems, multi input multi output (MIMO) transmission links, commercial ships, aircrafts and satellites, mobile communication systems and biomedical

applications. Most of the conformal arrays are designed as phased arrays ([1]-[4]). Therefore, additional advantages coming from the flexible pattern synthesis of the phased arrays like high beamwidth, low sidelobe levels and elimination of the interfering signals are also obtained.

In the design and analysis of conformal antennas/arrays, cylindrical host body geometry has always been the subject of interest due to the fact that most practical geometries can be approximated as a cylindrical geometry. Furthermore, it acts as a canonical geometry useful toward the development of design and analysis tools for antennas/arrays on arbitrarily convex smooth platforms. Studies on antennas/arrays conformal to cylindrical surfaces date back to as early as 1940's. However, the real interest on them arose around 1970's. In [5] the mutual coupling between antennas on an array of infinitely long longitudinal slots equispaced on a conducting cylinder was found. The eigenexcitation of a single antenna, which is equal to the eigenvalues of the scattering matrix, was calculated using the symmetry of the structure and then superposition principle was applied to obtain the general result. Then, the expressions for the radiation pattern and the coupling coefficients were derived. In [6], an asymptotic expression was derived to find the mutual impedance between rectangular slots on large conducting cylinders. The Geometrical Theory of Diffraction (GTD) was used to analyze the mutual coupling for arrays on a circular conducting cylinder as well as surfaces of variable curvature in [7]. This technique was applied to full-ring arrays and finite arrays of circular cylinders. At the same year in [8] the theory along with a computer program were developed to find the far-field pattern of a conformal array on a general conducting surface including the cross-polarization component if it exists. This was probably the first analysis tool developed for the conformal arrays in the literature. It could solve problems for arrays with upto 1000 elements, and the results were presented for arrays on circular cylinders, circular arcs, cones and planes.

One common property of all these initial researches on arrays conformal to the cylindrical surfaces is that they are made for conducting cylinders without a material coating. Investigations of arrays on material coated cylinders were generally approximated with an array on a grounded planar dielectric slab during

this period. In this work, conformal phased arrays of printed dipoles (in particular, circumferentially oriented ones) on material coated, electrically large circular cylinders have been analyzed. The lack of efficient and accurate design and analysis tools for this type of antennas/arrays still remains as a problem today, which provides the primary motivation for this work. Other than the printed structures on grounded planar dielectric slabs, majority of the reported studies on this topic can be cast into three categories:

- **Approximate Models**
  - Generalized Transmission Line Model (GTLM)
  - Cavity Model
- **Pure Numerical Methods**
  - Finite Element Method (FEM)
  - Finite Domain Time Domain Method (FDTD)
- **Hybrid techniques**
  - Finite Element- Boundary Integral (FE-BI) Method
  - Hybrid Method of Moments (MOM)/Green's Function Method in the Spectral Domain
  - Hybrid MoM/Green's Function Method in the Spatial Domain

Generalized transmission line model (GTLM) and cavity model are the most popular approximate models used in the design and analysis of printed geometries on coated circular cylinders. They are fairly simple and accurate only for a limited number of cases. However, if the thickness of the substrate is not very thin and/or mutual coupling among the array elements are required, then these methods are not suitable. GTLM is applied in [9] to analyze the probe-fed cylindrical-rectangular microstrip antennas by Wong et al.. Later in [10], they analyzed cylindrical-rectangular microstrip antennas with microstrip feedline or slot coupling where the microstrip antenna was approximated with an equivalent

circuit which was, in turn, used to calculate the input impedance of the antenna. In [11] the electromagnetic cavity solution was applied to find the resonance frequencies for a cylindrical-rectangular microstrip patch antenna and compared with the results for the planar rectangular patch antenna. It was found in this work that to use planar results is reasonable when the thickness of the dielectric substrate is small compared to the curvature. This method was expanded in [12]-[13] and used to make a complete analysis of conformal arrays. However, both the GTLM and the cavity method were not very accurate to be used in applications where the precision of the results obtained from the design process was a priority. Furthermore, GTLM could only be applied to the antennas/arrays with thin substrates.

Pure numerical methods like Finite Difference Time Domain Method (FDTD) and Finite Element Method (FEM) are also used to analyze antennas/arrays conformal to material coated circular cylinders. In [14], far-field patterns of conformal patch antennas were computed using a conformal FDTD method and non-uniform mesh. The radiation patterns of microstrip patch antennas mounted on cylindrical surfaces of arbitrary cross-sections were calculated in [15], where the magnetic currents on the microstrip patch antennas were obtained using FEM, and MoM together with the reciprocity theorem were used to find the far-field pattern. However, these pure numerical methods are not suitable for electrically large problems due to the computational time and storage requirements since a fixed number of unknowns per unit electrical surface area (λ^2; λ=wavelength) or volume (λ^3) should be placed.

In hybrid techniques, several methods are combined together. Examples of the hybrid techniques include finite element-boundary integral (FE-BI) method, hybrid MoM/Green's function method in the spectral domain and hybrid MoM/Green's function method in the spatial domain. In [16], the FE-BI formulation was used for the analysis of scattering by cavity backed antennas on circular cylinders. It was shown that both curvature and cavity size affect the radar cross-section of the antenna. In [17], the impedance characteristics of microstrip patch antenna arrays mounted on planar and cylindrical surfaces were analyzed. Liu et al. ([18]) used the higher order FEM along with the boundary

integral to find the radiation pattern and mutual coupling of conformal antennas. One disadvantage of the FE-BI method is the efficiency problems encountered for thick or multilayered substrates.

In the hybrid MoM/Green's function techniques (both spectral and space domains), the appropriate Green's function contains the geometrical and electrical properties of the host body. Therefore the unkowns are only the currents on the radiating elements. Among these two methods, the hybrid MoM/Green's function method in the spectral domain has been the more widely used one due to its simplicity ([19]-[22]). In [19], MoM was used to obtain the input impedance of printed circuit dipoles on electrically small, dielectric coated circular cylinders. The far-field pattern was then found using a steepest descent path method. In 1986, a spectral domain solution was proposed to find the near fields and the input impedance of printed antennas on cylindrical substrates ([20]). In this work a MoM formulation that is based on the spectral representation of the Green's function of coated circular cylinder was used to find the unknown currents on the antennas. In [21] resonance frequencies for the cylindrical-rectangular and wraparound patches were computed using two different approaches: A vector integral equation formulation in spectral domain which was solved using Galerkin's method and a perturbation approach. Then in [22], the vector integral equation formulation was used in spectral domain to calculate the input impedance and radiation patterns for both the cylindrical-rectangular and wrap-around elements. The cylindrical microstrip antennas were excited by a probe and the vector integral equation was solved using the Method of Moments. Also a single mode approximation was employed for thin substrates. Spectral domain solution is accurate and does not have singularity problems. However, it is computationally inefficient compared to other methods and has convergence problems when the radius of the cylinder or the separation between the source and observation points is large. Although there have been attempts to improve the spectral domain solution by using suitable basis functions, these problems persisted. One other limitation is the spectral domain representation of the Green's function is not available for every arbitrary host body geometry which arises the need for more general and complete solutions.

Recently, an efficient and accurate method combining the Method of Moments with a Green's function in space domain was presented to analyze the conformal antennas/arrays on material coated circular cylinders ([23]-[25]). Using this method, which is a hybrid one combining the Method of Moments with a special Green's function in the space domain, finite phased arrays of axially directed printed dipoles on electrically large coated cylinders were analyzed ([26]), which is an extension of the work presented in [27]. The same approach was then applied to the analysis of finite phased arrays of circumferentially oriented printed dipoles on the aforementioned cylinders ([28]). In this work, as mentioned before, a complete study of cylindrical arrays of circumferentially oriented printed dipoles are performed. [28] forms a basis towards the more in-depth analysis in this work. The results are also compared with those of the cylindrical arrays of axially oriented printed dipoles and planar arrays ([27]).

In the hybrid MoM/Green's function technique ([23]) that is used here, an electric field integral equation (EFIE) is formed such that the tangential component of the electric field vanishes over the dipole surface. Then, the currents on the dipole surfaces are expanded using N basis functions, where N is an integer. Using N weighting functions which are the same with the basis functions (a Galerkin MoM approach), the integral equation is converted into a matrix equation whose order is N. The N coefficients for the expansion of the currents are found by solving this matrix equation.

The kernel of the EFIE that is used to form the MoM matrix is the appropriate Green's function. Hence, the efficiency of the method relies heavily on the computation of the Green's function, three different high frequency based asymptotic representations for the Green's function, all of which are valid in different but overlapping regions, are developed and used interchangeably to make the computations in the most accurate and efficient way.

The first representation is the planar representation of the Green's function. If the separation between the source and observation points is small, an electrically large cylinder can be considered as locally flat. Hence, for the self-term

evaluations of the impedance matrix in the Method of Moments the planar approximation is used ([27], [29]). The second representation is the Steepest Descent Path (SDP) representation of the Green's function ([23]-[24]). In this representation, the circumferentially propagating series representation of the appropriate Green's function is obtained from its radially propagating counterpart using the Watson's transform. Then, it is evaluated along the SDP on which the integrand decays most rapidly, and from which the representation takes its name. The SDP representation is fast and accurate in the off-paraxial region (away from the axis of the cylinder). In particular, in the limiting case of large separations, this method reduces to the saddle point integration considered in [30]. Furthermore, its accuracy improves as the separation between the source and the observation points increases. The final representation is the Fourier Series Representation of the Green's function ([23], [25]) which is used in the paraxial (nearly axial) region and which complements the SDP representation. This representation actually works for all regions for the cylindrical arrays of circumferentially oriented dipoles when the separation between the source and observation points is relatively small, but it loses its accuracy when the separation gets larger for certain range of angles. However, it is very fast and accurate along the paraxial region. In this method, using the periodicity of the circumferentially propagating series representation of the Green's function a Fourier Series representation for the Green's function is obtained where taking at most the first two terms of the Fourier Series gives highly accurate results.

The organization of this thesis is as follows. In chapter 2, the theoretical foundation of the thesis is given. Method of Moments (MoM) that is used to find the currents on the dipoles is explained. Then, the switching algorithm between different Green's function representations is described. Finally different high frequency based asymptotic representations for the appropriate Green's function are given for the $G_{\phi\phi}$ and G_{zz} components, along with certain modifications made on the theory of SDP representation. In chapter 3, the array concepts are explained. A brief explanation of phased arrays is given in this chapter. The performance metrics used to evaluate the array performance like reflection coefficient and input impedance, as well as scan blindness phenomenon are defined. The numerical

results in the form of currents over elements, reflection versus element position, reflection versus scan angle and far-field pattern are given in chapter 4 for various finite (phased) arrays of circumferentially oriented dipoles on different, electrically large, coated cylinders. Effects of curvature and host body parameters on the system performance metrics are observed. A comparison with the spectral-domain method is made to assess the accuracy of the solution for relatively small arrays. The performance metrics of the investigated arrays are also compared with those of finite (phased) arrays of axially oriented dipoles and planar arrays. Chapter 5 concludes this thesis and briefly explains what it brings to the scene. There are also two appendices. In Appendix A, the Fourier Series (FS) representation of the G_{zz} component of the Green's function is found. Also, the analytical evaluation of the integrals with variable ψ in the FS representation is given. Appendix B gives the approximations for the special functions used in the definition of the Green's function. IEEE convention is assumed in this thesis such that vectors are denoted with bold-face while matrices are bold-faced and overlined. An e^{jwt} time dependence is assumed and suppressed throughout this work.

Chapter 2

Hybrid MoM/Green's Function Method

2.1 Introduction

This chapter presents an overview of the hybrid MoM/Green's function method in the spatial-domain. Section 2.2 explains the Method of Moments (MoM) briefly. In the MoM solution a matrix equation is formed from an electric field integral equation (EFIE) to find the unknown currents on the dipoles. The kernel of the EFIE is the appropriate Green's function which possesses the electrical and geometrical properties of the host platform. In this work, different high frequency based Green's function representations are used interchangeably in the EFIE to obtain the most accurate and efficient solution. The switching algorithm between these different representations of Green's functions for both cylindrical arrays of circumferentially oriented dipoles and cylindrical arrays of axially oriented dipoles are discussed in 2.2.1. In 2.3, the spectral-domain formulation for the evaluation of surface fields on a coated cylinder is described. The spectral domain solution is a well-known solution in the literature ([23], [32]), and is based on expressing the integral equations, which will be solved via MoM, over a spectrum of plane waves instead of the region of space on which the basis and expansion

functions occupy. However, Green's functions in the spectral domain are not convergent for electrically large cylinders and when the separation between the source and observation points are electrically large. This necessitate the need for more accurate and efficient solutions. The Steepest Descent Path representation of the Green's function which is explained in 2.4 provides an alternative in the off-paraxial region (the region away from the axis of the cylinder). The evaluation of the integrals for the SDP representation is explained in section 2.5. In section 2.6, a detailed pole analysis for the Green's function representations is performed to develop a new numerical approach for the evaluation of the integrals used in the SDP representation of the Green's function ([36]). Finally, in 2.7 another representation of the Green's function which is valid along the paraxial region, the Fourier Series representation, is described. A Fourier Series representation that works in the off-paraxial region is also given for the $G_{\phi\phi}$ component of the Green's function in 2.7.2.

2.2 The Moment Method Solution

Assume a finite, periodic array of (2N+1)x(2M+1) identical printed dipoles mounted on the outer surface of a dielectric coated circular cylinder as shown in Figure 2.1 for an array of axially oriented dipoles, or Figure 2.2 for an array of circumferentially oriented dipoles. The inner radius of the cylinder is denoted by a, the outer radius of the cylinder is denoted by d and hence, the thickness of the dielectric coating is $t_h = (d - a)$. The cylinder is assumed to be infinitely long in the axial (z) direction, and the relative dielectric constant of the dielectric coating is $\epsilon_r > 1$. The center-to-center distance between the dipoles in the axial direction is equal to d_z and in the circumferential direction it is equal to d_{rl}. The dimensions of the dipoles are z_a in the axial direction and r_{la} in the circumferential direction. The dipoles are center-fed and their generators are assumed to be infinitesimal. The equivalent circuit for each dipole is shown in Figure 2.1.

An electric field integral equation (EFIE) can be obtained by applying the boundary condition of zero tangential electric field on the surface of the dipoles

for this geometry ([23]-[28]). To do this, the total electric field is written as a sum of incident ($\mathbf{E}^i(\mathbf{r})$) and scattered ($\mathbf{E}^s(\mathbf{r})$) fields in the presence of the scatterer (a dielectric coated PEC cylinder in this case) as follows:

$$\mathbf{E}(\mathbf{r}) = \mathbf{E}^i(\mathbf{r}) + \mathbf{E}^s(\mathbf{r}) \tag{2.1}$$

The expressions for the incident and scattered electric fields are given by

$$\mathbf{E}^i(\mathbf{r}) = \int\int_{S_{source}} \overline{\mathbf{G}}(\mathbf{r}/\mathbf{r}').\mathbf{J}^i(\mathbf{r}')ds' \tag{2.2}$$

and

$$\mathbf{E}^s(\mathbf{r}) = \int\int_{S_{dipole}} \overline{\mathbf{G}}(\mathbf{r}/\mathbf{r}').\mathbf{J}^s(\mathbf{r}')ds' \tag{2.3}$$

where $\mathbf{J}^i(\mathbf{r}')$ is the known incident current distribution and $\mathbf{J}^s(\mathbf{r}')$ is the unknown current that will be found. Applying the aforementioned boundary condition on the dipole surface one can get:

$$\int\int_{S_{dipole}} \overline{\mathbf{G}}(\mathbf{r}/\mathbf{r}').\mathbf{J}^s(\mathbf{r}')ds' = -\int\int_{S_{source}} \overline{\mathbf{G}}(\mathbf{r}/\mathbf{r}').\mathbf{J}^i(\mathbf{r}')ds' \tag{2.4}$$

The unknown current distribution $\mathbf{J^s}(\mathbf{r}')$ on the nm^{th} ($-N \leq n \leq N, -M \leq m \leq M$) dipole can be expanded as a multiplication of an unknown current coefficient A_{nm} and a piecewise sinusoidal (PWS) basis function. A single expansion mode provides the necessary accuracy for this work. Assuming the dipoles are oriented either in the circumferential direction or in the axial direction, the expression for the current on the dipoles become

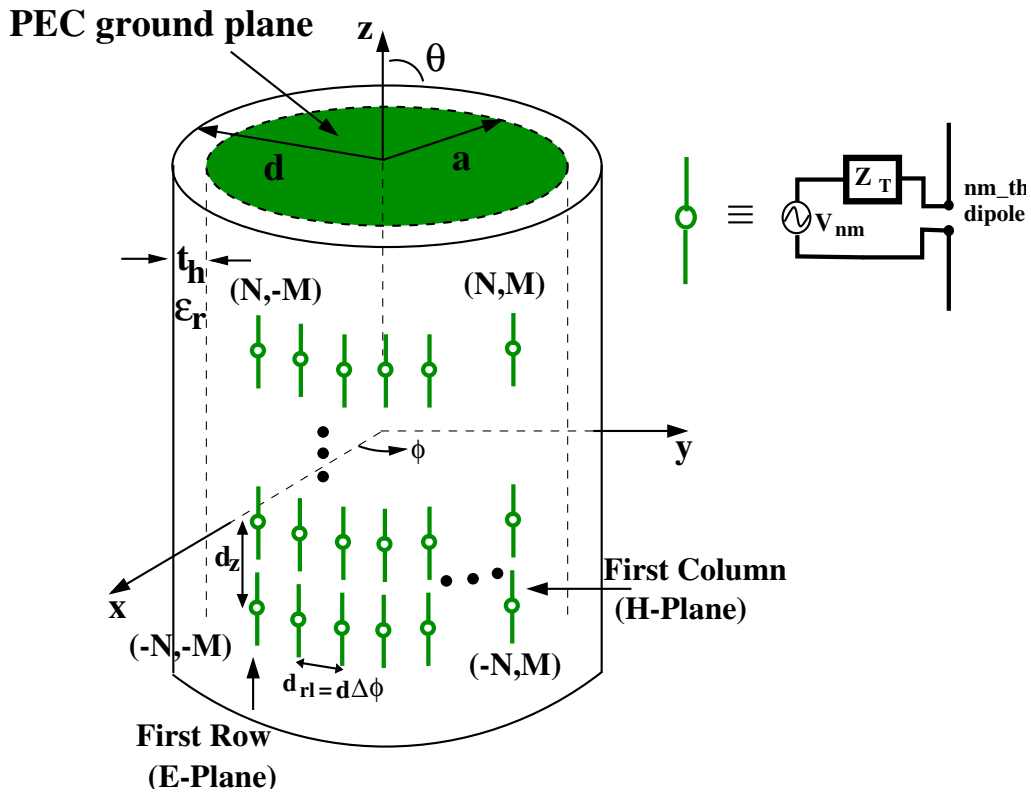

Figure 2.1: Finite (phased) array of axially oriented printed dipoles on a material coated circular cylinder, and the equivalent circuit for each dipole.

$$J^s_{nm}(z', r'_l) = A_{nm} f_{nm} = \begin{cases} A_{nm} \frac{sin[k_a(rl_a - |rl' - nd_{rl}|)]}{2z_a sin(k_a rl_a)} & \text{for } \phi\text{-directed elements} \\ A_{nm} \frac{sin[k_a(z_a - |z' - nd_z|)]}{2rl_a sin(k_a z_a)} & \text{for z-directed elements} \end{cases} \tag{2.5}$$

where the wave number k_a of the expansion mode can be written in terms of the free-space wave number k_0 and the dielectric constant of the coating of the cylinder ϵ_r as

$$k_a = k_0 \sqrt{\frac{(\epsilon_r + 1)}{2}}. \tag{2.6}$$

Using the Galerkin's MoM solution in which the basis and weighting functions are

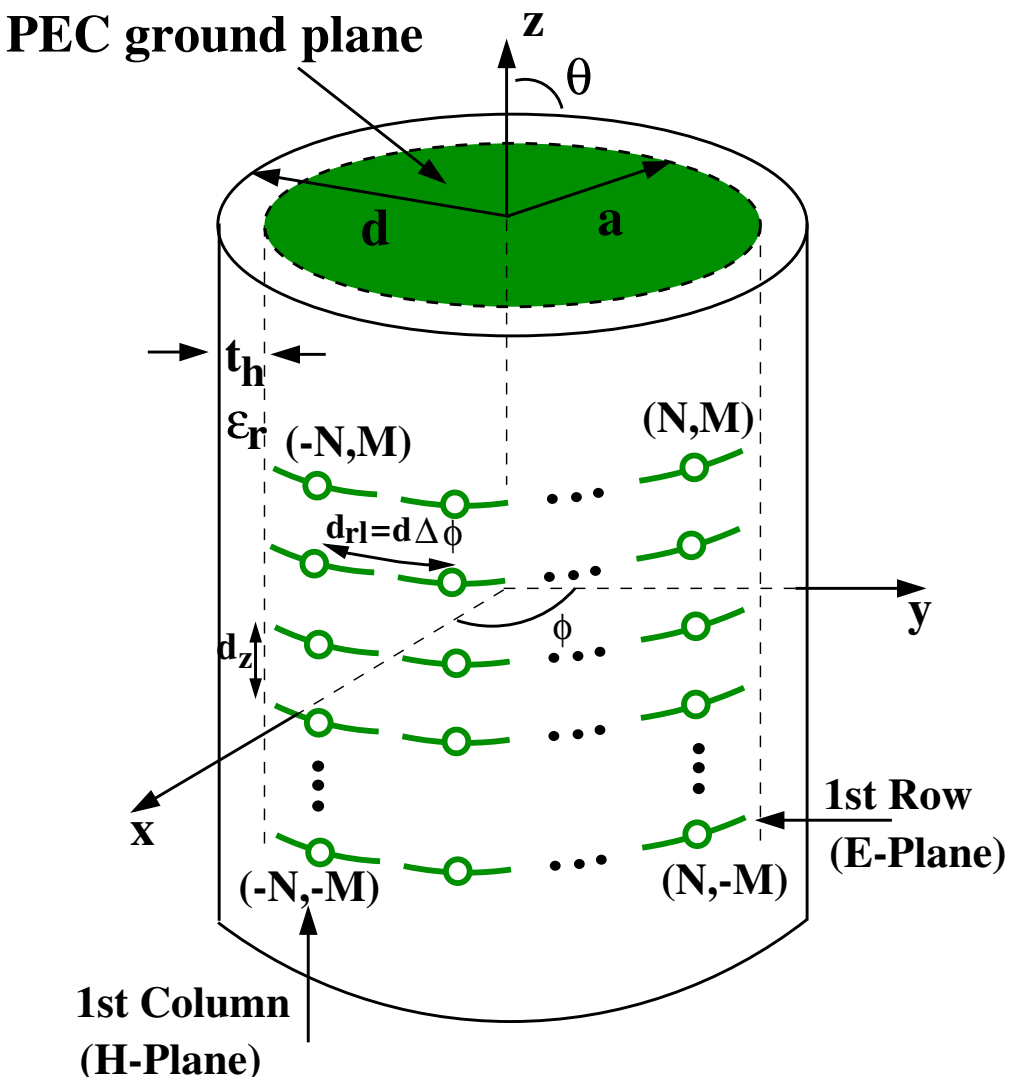

Figure 2.2: Finite (phased) array of circumferentially oriented printed dipoles on a material coated circular cylinder.

chosen to be identical (i.e. they are taken as in (2.5)), equation (2.4) is converted to a matrix equation given by

$$([\mathbf{Z}] + [\mathbf{Z_T}])\,\mathbf{I} = \mathbf{V}. \tag{2.7}$$

Here $[\mathbf{Z_T}]$ is the generator terminating impedance matrix which is a diagonal matrix. In this work, the forced excitation case is inspected where $[\mathbf{Z_T}] = \mathbf{0}$

but the method can also handle the free excitation case where $[\mathbf{Z_T}] \neq \mathbf{0}$. The elements of the impedance matrix $[\mathbf{Z}]$ are given by

$$Z_{nm,pq} = \int_{S_{pq}} ds_{pq} f_{pq}(\mathbf{r}_{pq}) \left(\int_{S_{nm}} ds'_{nm} G_{lu}(\mathbf{r}_{pq}/\mathbf{r}'_{nm}) f_{nm}(\mathbf{r}'_{nm}) \right) \tag{2.8}$$

which is equal to the mutual coupling between the pq^{th} and the nm^{th} ($-N \leq p,\ n \leq N,\ -M \leq q,\ m \leq M$) elements if $pq \neq nm$, or the self-term if $pq = nm$. G_{lu} is the appropriate component of the Green's function. For cylindrical arrays of circumferentially oriented dipoles, which is the main focus of this thesis, the $G_{\phi\phi}$ component of the Green's function is necessary to obtain the coupling between two ϕ-directed dipoles. Similarly, for a cylindrical array of axially oriented dipoles whose performance is compared with that of the cylindrical array of circumferentially oriented dipoles, the G_{zz} component of the Green's function is needed. Other components of the Green's function are not used and hence they are not mentioned in this thesis. The Green's function is the kernel of the integral equation that gives the coupling, hence the accuracy and the efficiency of the method depends on the evaluation of the Green's function representation. Different Green's function representations are used interchangeably to achieve this goal. The switching algorithm between different Green's function representations are presented in 2.2.1.

The elements of the voltage vector are given by the following equation:

$$V_{pq} = -\int\int_{S_{pq}} ds_{pq} \mathbf{f}(\mathbf{r}_{pq}).\mathbf{E}^i(\mathbf{r}_{pq}) \tag{2.9}$$

Here, the incident electric field $\mathbf{E}^i$ can be selected according to the needs of the application. In this work the elements of the array are excited to form a scanning array such that the maximum radiation is in the (θ_i, ϕ_i) scan direction as follows:

$$V_{pq} = e^{-jk_0 sin\theta_i dcos(\phi_i - p\Delta\phi)} e^{-jk_0 cos\theta_i q d_z}. \tag{2.10}$$

Finally, the current matrix $[\mathbf{I}]$ has the unknown current coefficients (A_{nm})

as its elements which are found by solving the matrix equation. The Toeplitz property of the matrix [**Z**] is used to reduce the computational time and LU-decomposition method is applied in the solution.

2.2.1 Switching Algorithms

Three different Green's function representations in the spatial domain are used interchangeably in this thesis. These Green's function representations are valid in different but overlapping regions of the coated cylinder surface. As previously mentioned, the accuracy and efficiency of this hybrid method relies on using the computationally optimum Green's function representation available throughout the whole solution region.

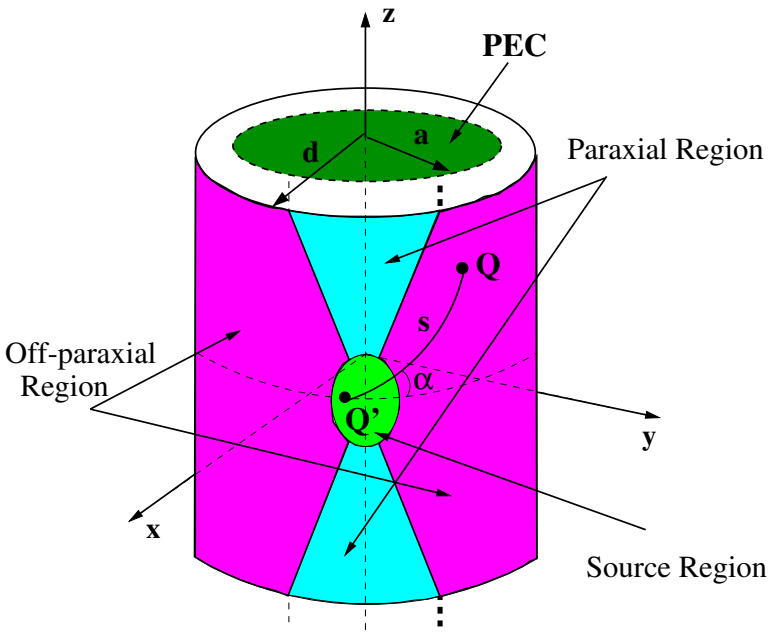

Figure 2.3: The regions where different representations of the Green's function are used for cylindrical arrays of z-directed printed dipoles.

The first representation is the planar representation which is used for the self-term evaluations in the source region as illustrated in Figures 2.3 and 2.4. It is based on an efficient integral representation of the planar microstrip dyadic

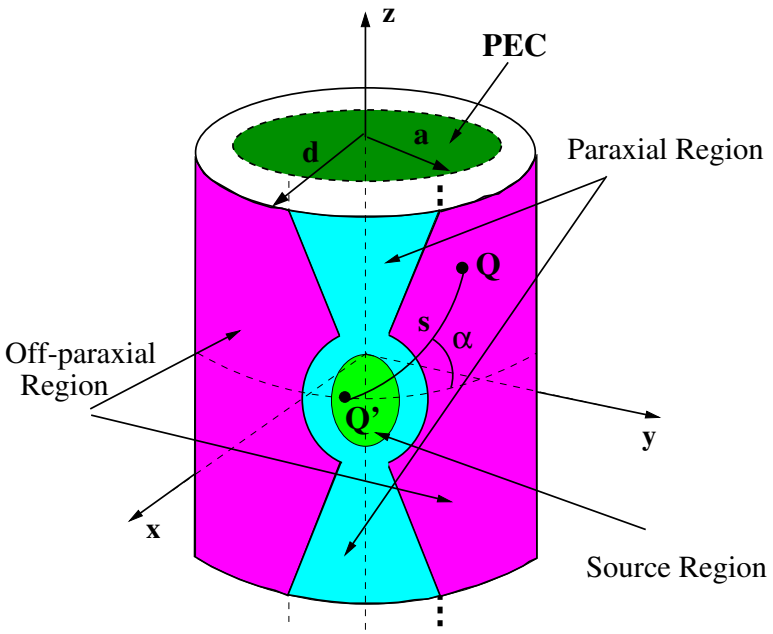

Figure 2.4: The regions where different representations of the Green's function are used for cylindrical arrays of ϕ-directed printed dipoles.

Green's function ([27], [29]). It is implemented under the assumption that for an electrically large coated cylinder small separations can be considered as locally flat. The second one is the steepest descent path (SDP) representation of the Green's function ([23]-[24]) which is explained in section 2.4. Briefly, this representation is valid at the off-paraxial region and is based on evaluating the circumferentially propagating series representation of the appropriate Green's function efficiently along an SDP on which the integrand decays most rapidly. The final representation is the Fourier series (FS) representation of the Green's function ([23], [25]) and is explained in detail in 2.7. Briefly, in this representation, the Green's function components are expanded into Fourier Series using their periodicity in one of their variables. FS representation is valid at the off-paraxial region as well for the $G_{\phi\phi}$ component, though its accuracy gets worse for large separation at certain range of angles between the ray path and the circumferential axis (i.e. certain α values as depicted in Figure 2.3 and Figure 2.4) . On the other hand, for the G_{zz} component of the Green's function the FS representation is only available for the paraxial region.

Since FS representation, available for the off-paraxial region for the $G_{\phi\phi}$ component of the Green's function, is very efficient and accurate especially for small separations between the source and the observation points, different switching algorithms for the cylindrical arrays of axially oriented printed dipoles and cylindrical arrays of circumferentially oriented printed dipoles are used as shown in the Figures 2.3 and 2.4, respectively. The switching algorithm for the $G_{\phi\phi}$ component of the Green's function for ($t_h = 0.06\lambda_0$, $\epsilon_r = 3.25$) can be written as follows:

$$G_{\phi\phi} = \begin{cases} \text{Planar Representation} & \text{For self-term evaluations} \\ \text{FS Representation} & \text{If } \alpha \geq 65^\circ \text{ or if } s < 2.3\lambda_0 \text{ for } \alpha < 65^\circ \\ \text{SDP Representation} & \text{Else} \end{cases} \tag{2.11}$$

It can be seen from these figures that the SDP representation is still used for large separations between the source and observation points in the off-paraxial region for cylindrical arrays of circumferentially oriented dipoles. The reason for this is that SDP representation tends to get more efficient and accurate as the separation increases as explained in section 2.4. Also it should be noted that the regions where these representations are accurate may change with the change of array and host body parameters. For example, as the thickness of the dielectric substrate decreases, SDP representation becomes valid in a larger region while the region where the FS representation is valid gets smaller. However, the change of the radius of the cylinder does not affect the regions where different representations remain accurate much. The switching algorithm for the $G_{\phi\phi}$ component of the Green's function for ($t_h = 0.02\lambda_0$, $\epsilon_r = 3.25$) is

$$G_{\phi\phi} = \begin{cases} \text{Planar Representation} & \text{For self-term evaluations} \\ \text{FS Representation} & \text{If } \alpha \geq 60^\circ, \text{ if } s < 1.5\lambda_0 \text{ for } 60^\circ > \alpha \geq 40^\circ \\ & \text{or } s < 0.8\lambda_0 \text{ for } \alpha < 40^\circ \\ \text{SDP Representation} & \text{Else} \end{cases} \tag{2.12}$$

2.3 Formulation of the Surface Fields on a Large Coated Cylinder in Spectral Domain

The cylindrical Fourier transform $F(n, k_z)$ of a function $f(\phi, z)$ is defined as ([32]-[33])

$$\tilde{F}(n, k_z) = \frac{1}{2\pi} \int_0^{2\pi} \int_{-\infty}^{\infty} f(\phi, z) e^{-jk_z z} e^{-jn\phi} dz d\phi \tag{2.13}$$

and the inverse transform is given by

$$f(\phi, z) = \frac{1}{2\pi} \sum_{-\infty}^{\infty} e^{jn\phi} \left\{ \int_{-\infty}^{\infty} \tilde{F}(n, k_z) e^{jk_z z} dk_z \right\}. \tag{2.14}$$

Assuming a tangential surface current located at $\rho' = d$ on a coated cylinder

$$\mathbf{J} = \mathbf{P_e} \frac{\delta(\phi - \phi')\delta(z\text{-}z')}{\rho'} \tag{2.15}$$

where $P_e = P_e^z \hat{z} + P_e^\phi \hat{\phi}$, its cylindrical Fourier Transform using (2.13) is given by

$$\tilde{J} = \frac{P_e}{2\pi d} e^{jk_z z'} e^{jn\phi'}. \tag{2.16}$$

The electric field due to this generic current distribution is given by

$$E_l(\phi,z)=\frac{1}{2\pi}\sum_{n=-\infty}^{\infty}e^{-jn(\phi-\phi')}\int_{-\infty}^{\infty}\frac{\tilde{G}_{lu}(n,k_z)P_e^u}{2\pi d}e^{jk(z-z')}dk_z \tag{2.17}$$

where $\hat{u}$ ($\hat{u}=\hat{\phi}$ or $\hat{z}$) represents the source direction and $\hat{l}$ ($\hat{l}=\hat{\phi}$ or $\hat{z}$) represents the observation direction. $\tilde{G}_{lu}(n,k_z)$ is the corresponding component of the appropriate dyadic Green's function in the spectral-domain. The components of the appropriate Green's function , which include the electrical and geometrical properties of the coated cylinder are found by applying the boundary conditions. Namely;

- The tangential components of the electric field are zero at the conductor surface ($\rho=a$),
- The tangential components of the electric field are continuous at the air-dielectric interface ($\rho=d$),
- The tangential components of the magnetic field are discontinuous by an amount of $\mathbf{J}$ at the air-dielectric interface ($\rho=d$),
- Fields satisfy the radiation condition (i.e. fields vanish as $\rho\to\infty$).

Applying the boundary conditions, $G_{\phi\phi}$ and G_{zz} components of the Green's function are given ([23]) for the case where the source and observation points are both at the air-dielectric interface of the coated cylinder ($\rho=\rho'=d$) as follows:

$$\tilde{G}_{\phi\phi}(n,k_z)=\frac{jZ_0}{k_0}\left\{\left[\frac{k_0^2k_{t0}}{k_{t1}^2}\right]\frac{R_nC_n^eT_m}{T}-k_{t0}\frac{R_nT_c^2}{(\epsilon_r-1)T}-\left[\frac{nk_z}{dk_{t1}}\right]^2\frac{C_n^e-k_{t0}R_n}{T}\right\} \tag{2.18}$$

and

$$\tilde{G}_{zz}(n,k_z)=\frac{jZ_0}{k_0}k_{t0}^2\frac{T_e}{T} \tag{2.19}$$

where k_{t0} is the transverse propagation constant in the free-space and k_{t1} is the transverse propagation constant inside the dielectric, which are given by

$$k_{t0}^2 = k_0^2 - k_z^2; \quad k_0 = w\sqrt{\epsilon_0 \mu_0} \tag{2.20}$$

$$k_{t1}^2 = k_1^2 - k_z^2; \quad k_1 = w\sqrt{\epsilon_1 \mu_1} \tag{2.21}$$

The special functions used in equations (2.18) and (2.19) are defined in the following equations:

$$T = T_e T_m - T_c^2 \tag{2.22}$$

$$T_e = k_{t0} R_n - \frac{k_{t0}^2}{k_{t1}^2} C_n^e \tag{2.23}$$

$$T_m = k_{t0} R_n - \epsilon_r \frac{k_{t0}^2}{k_{t1}^2} C_n^m \tag{2.24}$$

$$T_c = \frac{k_0(\epsilon_r - 1)}{k_{t1}^2} \frac{n k_z}{d} \tag{2.25}$$

$$R_n = \frac{H_n^{(2)'}(k_{t0} d)}{H_n^{(2)}(k_{t0} d)} \tag{2.26}$$

$$C_n^e = k_{t1} \frac{J_n'(k_{t1}a) Y_n'(k_{t1}d) - J_n'(k_{t1}d) Y_n'(k_{t1}a)}{J_n'(k_{t1}a) Y_n(k_{t1}d) - J_n(k_{t1}d) Y_n'(k_{t1}a)} \tag{2.27}$$

$$C_n^m = k_{t1} \frac{J_n(k_{t1}a) Y_n'(k_{t1}d) - J_n'(k_{t1}d) Y_n(k_{t1}a)}{J_n(k_{t1}a) Y_n(k_{t1}d) - J_n(k_{t1}d) Y_n(k_{t1}a)}. \tag{2.28}$$

Here $(')$ denotes the derivative with respect to the argument of the functions. The evaluation of these special functions are explained in Appendix B.

A major problem with the spectral-domain (eigenfunction) representation of the Green's function is that it has convergence problems for electrically large cylinders and large separations between the source and observation points. This can be seen by looking at the limiting values of the Green's function components for large n and k_z values. The results for the $G_{\phi\phi}$ and G_{zz} components of the Green's function are given as ([33]):

$$\lim_{n\to\infty} G_{\phi\phi}(n, k_z) = C_1\, n \tag{2.29}$$

$$\lim_{k_z\to\infty} G_{zz}(n, k_z) = C_2\, k_z \tag{2.30}$$

where C_1 and C_2 are constants. This numerical problem can be handled for electrically small cylinders and small separations between source and observation points by using carefully chosen basis functions which yield a spectral decay of $\frac{1}{n^2}$ or $\frac{1}{k_z^2}$ in a MoM based solution. However, the rate of convergence for the product of Green's function and basis functions is still slow (in particular, for electrically large cylinders) which arises the need for more computationally efficient solutions.

2.4 Steepest Descent Path (SDP) Representation of the Green's Function

This representation is based on the efficient numerical evaluation of a circumferentially propagating series representation of the appropriate Green's function ([23]-[24]). The numerical evaluation is performed along a steepest descent path on which the integrands decay most rapidly.

To obtain the SDP representation, one first should apply the Watson's transform to the equation (2.17). The result is:

$$E_l(\phi,z) = \frac{1}{4\pi^2 d}\int_{-\infty}^{\infty} dk_z e^{-jk_z(z-z')} \left\{\int_{-\infty-j\epsilon}^{\infty-j\epsilon} G_{lu}(k_z,\nu)P_e^u\left(\sum_{p=-\infty}^{\infty} e^{-j\nu[(\phi-\phi')-2\pi p]}\right)d\nu\right\}. \quad (2.31)$$

The original integration contour C in the ν-domain that is used to evaluate this integral ([23]-[24]) is $C = C_1+C_2$ as shown in Figure 2.5. However, the integration contour is deformed towards the third quadrant to obtain the modified contour $\tilde{C} = \tilde{C}_1 + C_2$ for the faster convergence of the integrands with the assumption that there are no branch cuts or poles in the third quadrant. In equation (2.31), the electric field can be interpreted as a sum of infinite number of rays in the circumferential direction. For an electrically large cylinder, in general the effect of multiple wave encirclements is negligible since they lose their strength as they travel on the surface of the cylinder. Therefore, taking only the term corresponding to $p = 0$ is enough for most cases. The resulting expression for the electric field is given by:

$$E_l(\phi,z) = \frac{1}{4\pi^2 d}\int_{-\infty}^{\infty} dk_z e^{-jk_z(z-z')} \left\{\int_{-\infty-j\epsilon}^{\infty-j\epsilon} G_{lu}(k_z,\nu)P_e^u e^{-j\nu(\phi-\phi')}d\nu\right\}. \quad (2.32)$$

Note that for some cases the second ray contribution (which travels in the opposite direction) is included as well. Performing a Fock's type substitution and employing the polar transformations which are given as:

$$\nu = k_{t0}d + m_t\tau \quad (2.33)$$

where

$$m_t = \left(\frac{k_{t0}d}{2}\right)^{\frac{1}{3}} \quad (2.34)$$

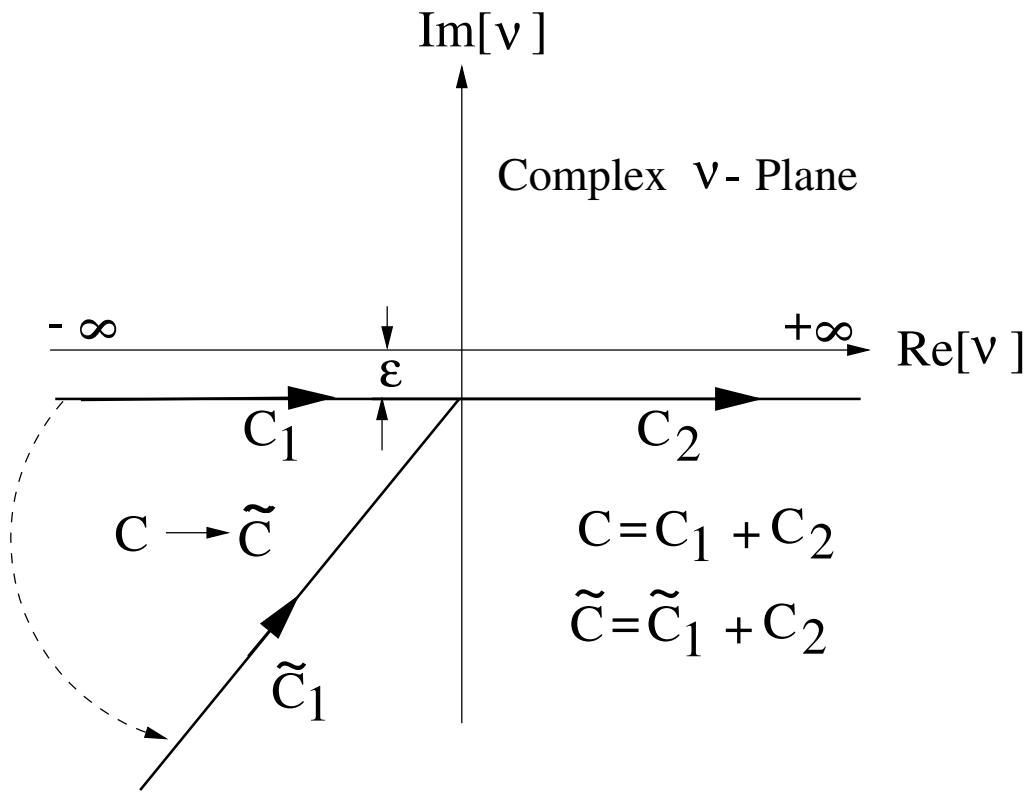

Figure 2.5: Integration contour in the ν-domain

$$k_z = k_0 sin\psi \tag{2.35}$$

$$k_{t0} = k_0 cos\psi \tag{2.36}$$

and using the geometrical relations, shown in Figure 2.6, given by

$$z - z' = ssin\alpha \tag{2.37}$$

$$d(\phi - \phi') = scos\alpha \tag{2.38}$$

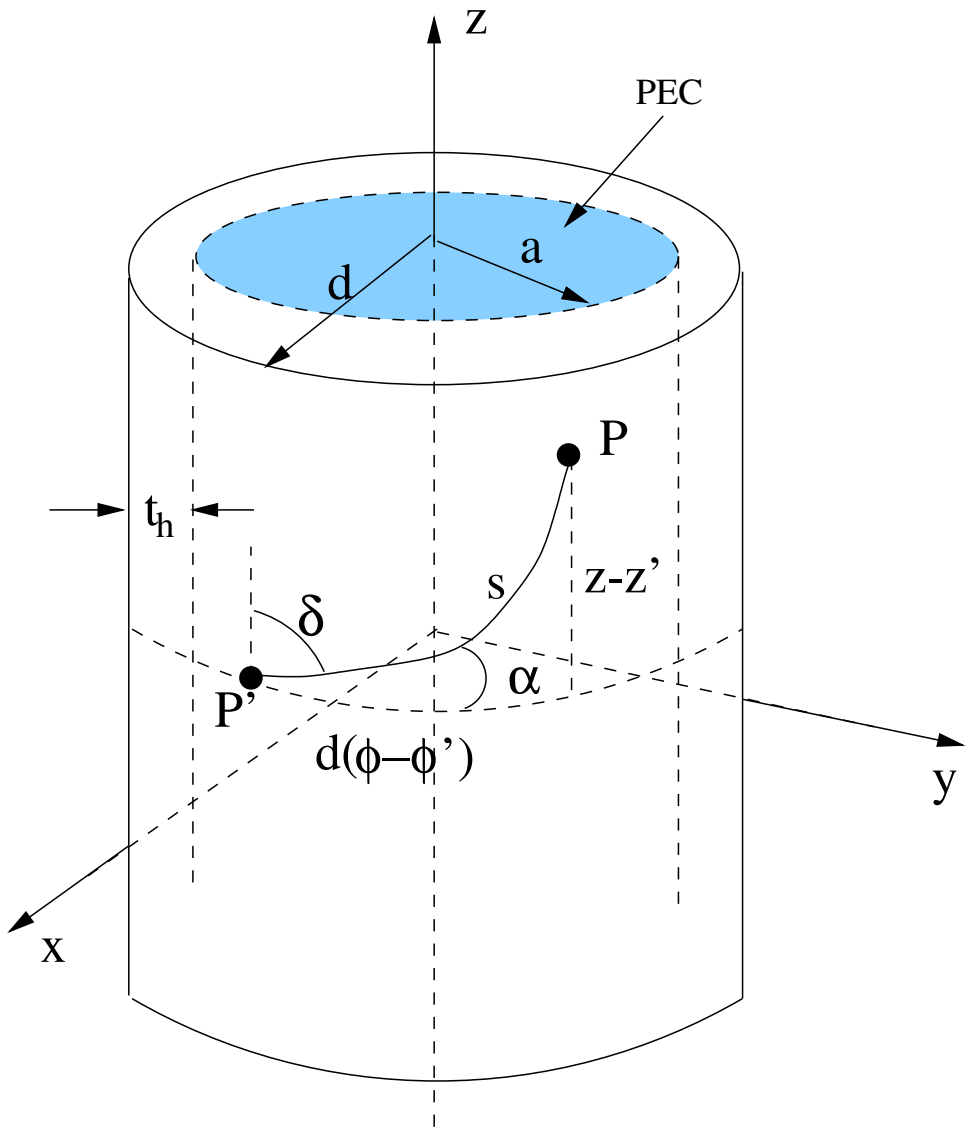

Figure 2.6: The cylindrical geometry

with s being the arc length of the geodesic path on the surface of the coating between source and observation points, and α being the angle between s and the circumferential axis, the following expression for the electric field is obtained:

$$E_l(\alpha, s) \approx \frac{1}{4\pi^2 d} \int_{C_\Psi} d\psi k_0 cos\psi e^{-jk_0 s sin\psi sin\alpha}$$

$$\left(\int_{C_\tau} G_{lu}(\psi,\tau) P_e^u e^{-jk_0 s cos\psi cos\alpha} e^{-jm_t\tau(\phi-\phi')} m_t d\tau\right). \quad (2.39)$$

The integration in the contour C_Ψ can be transformed into an integration in the steepest descent path where the integrand decays most rapidly as described in [23]. The result is given by

$$E_l(\alpha,s) \approx \frac{\sqrt{2}e^{-j3\pi/4}}{4\pi^2 d}\frac{e^{-jk_0 s}}{\sqrt{k_0 s}}\int_{-\infty}^{\infty} d_t e^{-t^2}\tilde{F}(\alpha,s,t) \quad (2.40)$$

where

$$\tilde{F}(\alpha,s,t) = \frac{k_0 cos\psi(t)}{cos\left(\frac{\alpha-\psi(t)}{2}\right)}\int_{C_\tau(t)} G_{lu}(\tau,t) P_e^u m_t e^{-j\xi\tau} d\tau \quad (2.41)$$

$$\psi(t) = \alpha - 2arcsin\left(\frac{te^{j\pi/4}}{\sqrt{2}\sqrt{k_0 s}}\right) \quad (2.42)$$

and

$$\xi = m_t(\phi-\phi'). \quad (2.43)$$

In (2.40) and (2.41), $l = u$ and $G_{lu} = G_{\phi\phi}$ or G_{zz} given by (2.18) and (2.19) with n is replaced by ν which is related to τ by (2.33). The rate of convergence of the resulting expression is much faster than that of the spectral-domain representation. Also, when the separation between the source and observation points is large, the only contribution on the SDP path comes from the saddle point. Hence, the evaluation of the integration gets even faster for large s values. In the limiting case (when only the saddle point integration is required), the SDP method recovers the UTD-based surface fields due to a tangential surface current given by equation (2.15). However, in the paraxial region the SDP representation fails due to the Fock-type substitution given by equation (2.33). Therefore, another representation is needed for the evaluation of the surface fields in the paraxial region, which is explained in detail in 2.7.

2.5 Numerical evaluation of the Integrals for the SDP Representation

The surface wave expressions given by (2.40) and (2.41) have two integrals in the t and τ domains that have to be evaluated numerically in most cases. However, evaluation of these integrals introduce some numerical problems which will be discussed in this section. In the t domain, the integration is performed using a Gauss-Hermit Quadrature algorithm, whereas in the τ domain, Filon's algorithm is used in conjunction with a Gaussian Quadrature integration algorithm, and a proper tail is added when necessary. Furthermore, the contour of integration in the τ domain is dependent upon the value of t. Therefore, the outer integral is the t-domain integral. In other words, for each t value a new contour $C_\tau(t)$ should be defined and the τ-domain integral should be evaluated on this $C_\tau(t)$ contour.

2.5.1 Integration in the t-domain: Gauss-Hermit Quadrature Algorithm

The integration in the t-domain is evaluated using the Gauss-Hermite Integration Algorithm ([23]) which is described by the following equation:

$$\int_{-\infty}^{\infty} e^{-x^2} f(x)dx = \sum_{j=1}^{N} w_j f(x_j). \tag{2.44}$$

In equation (2.44), x_j are the roots of the Hermite polynomials H_j which are given by the iterative formula ([34])

$$H_{j+1} = 2xH_j - 2jH_{j-1} \tag{2.45}$$

where $H_0(x) = 1$, $H_1(x) = 2x$ and rest of the Hermite polynomials can be found by iteration from the equation (2.45). The weights w_j are found using ([34])

$$w_j = \frac{2}{(\sqrt{2j}\tilde{H}_{j-1})^2} \tag{2.46}$$

where $\tilde{H}_j$ is an orthonormal polynomial slightly different than H_j, and $\tilde{H}_j$ can be found using the recursion relation ([34])

$$\tilde{H}_{j+1} = x\sqrt{\frac{2}{j+1}}\tilde{H}_j - \sqrt{\frac{j}{j+1}}\tilde{H}_{j-1}. \tag{2.47}$$

Here $\tilde{H}_{-1} = 0$ and $\tilde{H}_0 = \frac{1}{\pi^{1/4}}$ ([34]). By substituting these results in equations (2.40) and (2.41), the tangential components of the electric fields are found as:

$$\begin{aligned} E_\phi(\alpha, s) \approx & \frac{\sqrt{2}e^{-j3\pi/4}}{4\pi^2 d}\frac{e^{-jk_0 s}}{\sqrt{k_0 s}}\sum_{q=1}^{Q} w_q \frac{k_0 cos\psi(t_q) m_t}{cos(\frac{\alpha-\psi(t_q)}{2})} \\ & \left[\int_{C_{\tau(t_q)}} (G_{\phi\phi}(\tau, t_q)P_e^\phi + G_{\phi z}(\tau, t_q)P_e^z)e^{-j\xi\tau}d\tau\right] \end{aligned} \tag{2.48}$$

$$\begin{aligned} E_z(\alpha, s) \approx & \frac{\sqrt{2}e^{-j3\pi/4}}{4\pi^2 d}\frac{e^{-jk_0 s}}{\sqrt{k_0 s}}\sum_{q=1}^{Q} w_q \frac{k_0 cos\psi(t_q) m_t}{cos(\frac{\alpha-\psi(t_q)}{2})} \\ & \left[\int_{C_{\tau(t_q)}} (G_{z\phi}(\tau, t_q)P_e^\phi + G_{zz}(\tau, t_q)P_e^z)e^{-j\xi\tau}d\tau\right] \end{aligned} \tag{2.49}$$

In the case when $Q = 1$, the only contribution comes from the saddle point. As mentioned above, the integration contour in the τ domain depends on the value of t, hence it changes for different t_q values. This is illustrated in Figure 2.7 for a 3-point Gaussian-Hermite algorithm.

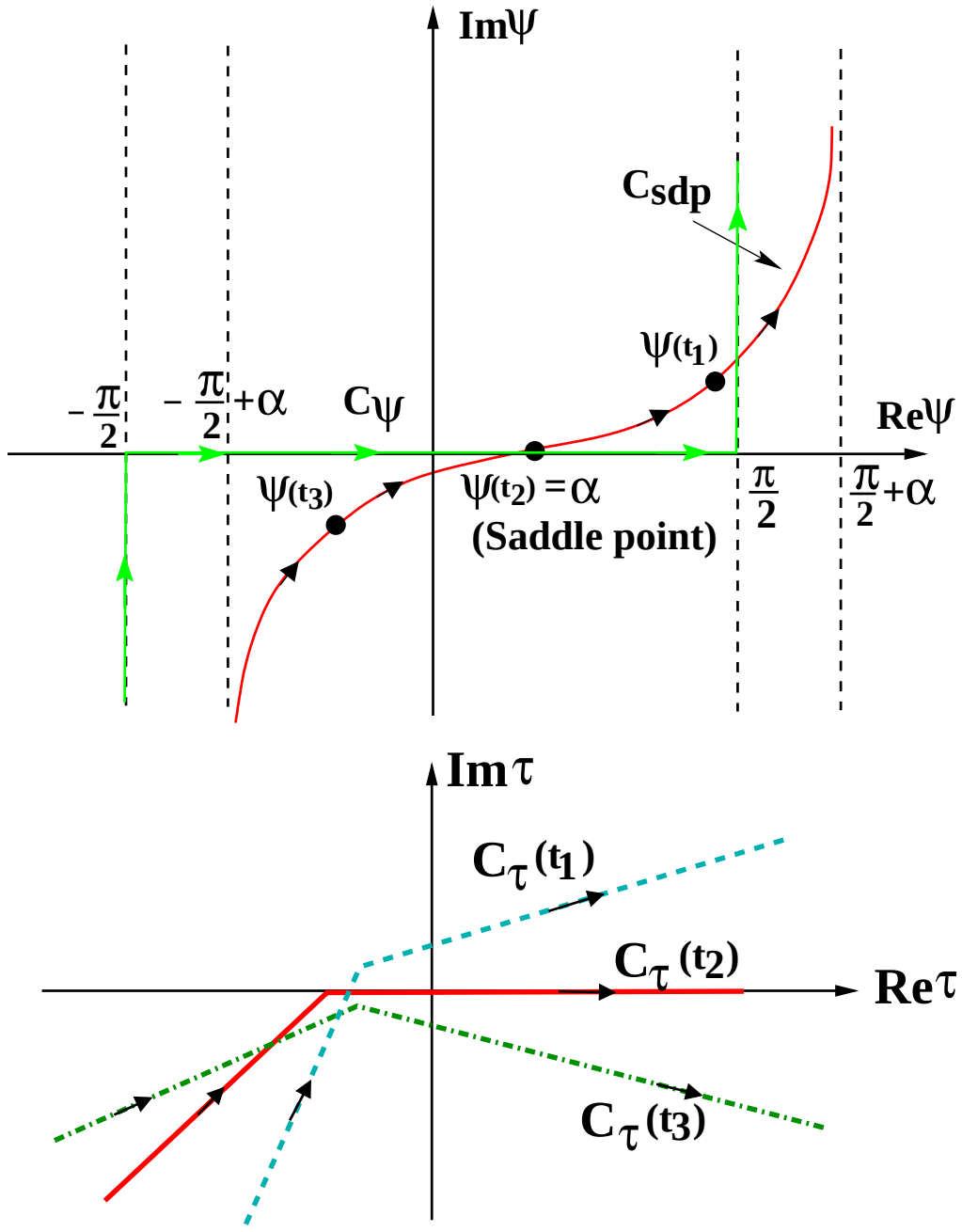

Figure 2.7: Integration contours along the SDP and in the τ-domain

2.5.2 Integration in the τ -domain and the Tail Contributions

The integration in the τ -domain is highly oscillatory. Filon's algorithm is used to handle this oscillatory nature along with a Gaussian-quadrature algorithm to evaluate the integrals. Also, the limiting values of the Green's function components $G_{\phi\phi}$ and G_{zz} as $\tau \to \infty$ are not absolutely convergent ([23]) as seen in the equations (2.50)-(2.51). This necessitates the use of a tail integration, which is obtained making use of the limiting values of G_{zz} and $G_{\phi\phi}$ for large τ values given by ([23])

$$\lim_{\tau\to\infty} G_{zz}(t_q,\tau) = \frac{B_1}{\tau} \tag{2.50}$$

$$\lim_{\tau\to\infty} G_{\phi\phi}(t_q,\tau) = B_2\tau + B_3 \tag{2.51}$$

where B_1, B_2 and B_3 are constants whose values are given in ([23]). For the G_{zz} component of the Green's function, the integral with respect to τ can be written as ([23])

$$I_1 = C_1 \int_{C_\tau(t_q)} G_{zz}(t_q,\tau) P_e^z e^{-j\xi\tau} d\tau. \tag{2.52}$$

The integration contour $C_\tau(t_q)$ can be divided into three regions as shown in Figure 2.8 which leads to the following equation:

$$\begin{aligned} I_1 &= C_1 \Bigg[\int_{C_\tau^-(t_q)} G_{zz}(t_q,\tau) P_e^z e^{-j\xi\tau} d\tau + \int_{\tilde{\tau}}^{\tau'} G_{zz}(t_q,\tau) P_e^z e^{-j\xi\tau} d\tau \\ &\quad + \int_{\tau'}^{\hat{p}_q\infty} \frac{B_1}{\tau} P_e^z e^{-j\xi\tau} d\tau \Bigg]. \end{aligned} \tag{2.53}$$

In this equation, $\hat{p}_q$ is the unit vector denoting the direction of the contour $C_\tau^+(t_q)$

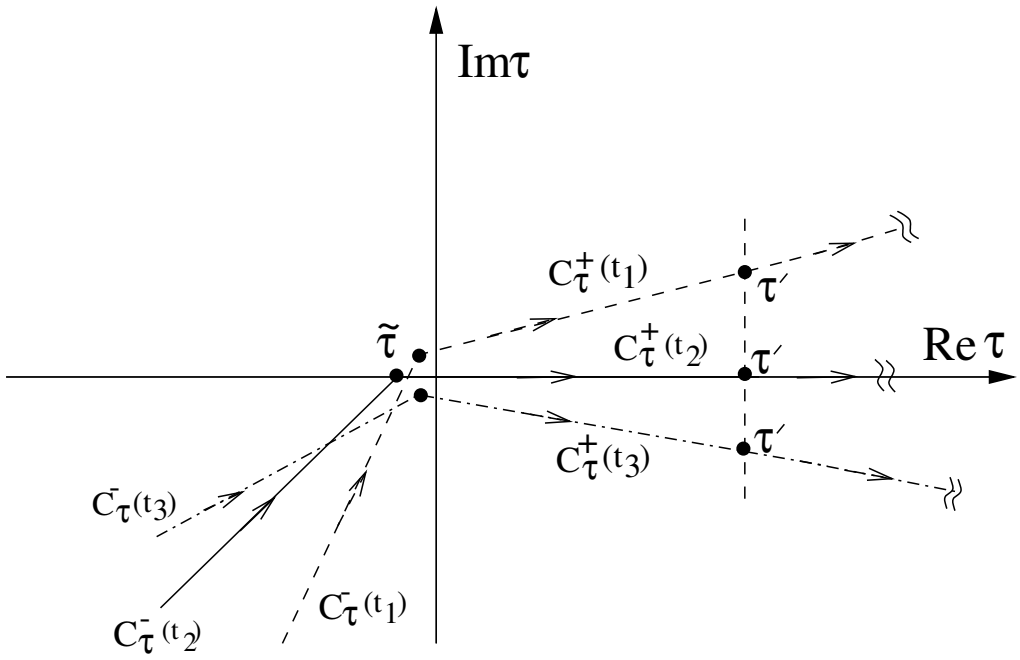

Figure 2.8: Integration contour in the τ-domain

that corresponds to a t_q value found from the Gaussian-Hermite integration algorithm. In the contour C_τ^- and in the segment of the contour C_τ^+ between $\tilde{\tau}$ and τ', the integrals are evaluated using Filon's algorithm. The tail contribution is taken between τ' and $\hat{p}_q\infty$ which can be written as

$$F_1(\tau') = \int_{\tau'}^{\hat{p}_i\infty} \frac{B_1}{\tau} e^{-j\xi\tau} d\tau. \tag{2.54}$$

The tail contribution is evaluated in [23] using the first order stationary phase method by taking only the end-point contributions since there is not a saddle point in this integration interval. The result is given by

$$F_1(\tau') \approx B_1 \frac{e^{-j\xi\tau'}}{j\xi\tau'}. \tag{2.55}$$

Similarly, the $G_{\phi\phi}$ component of the Green's function can be expressed as

$$I_2 = C_1\Bigg[\int_{C_\tau^-(t_q)} G_{\phi\phi}(t_q,\tau)P_e^\phi e^{-j\xi\tau}d\tau + \int_{C_\tau^+(t_q)} \left(G_{\phi\phi}(t_q,\tau) - B_2\tau - B_3\right) P_e^\phi e^{-j\xi\tau}d\tau$$
$$+ \int_{C_\tau^+(t_q)} B_2\tau P_e^\phi e^{-j\xi\tau}d\tau + \int_{C_\tau^+(t_q)} B_3 P_e^\phi e^{-j\xi\tau}d\tau\Bigg]. \tag{2.56}$$

The last term of the integral which is given by

$$F_2(\tau') = \int_{\tau'}^{\hat{p}_i\infty} B_3 e^{-j\xi\tau}d\tau \tag{2.57}$$

can also be evaluated using first order stationary-phase method, and the result is given by

$$F_2(\tau') \approx B_3\frac{e^{-j\xi\tau'}}{j\xi}. \tag{2.58}$$

The term with the constant B_2 was evaluated as the Fourier transform of a unit-ramp function in [23] and evaluated as:

$$\int_{C_\tau^+(tq)} B_2\tau e^{-j\xi\tau}d\tau = -B_2\frac{1}{\xi^2}. \tag{2.59}$$

This approximation assumes that $\tilde{\tau} \approx 0$ as it is evident from the definition of the Fourier transform. However, since $\tilde{\tau}$ is not exactly 0, some error is introduced when this equation is used. Actually, the tail integral for this case can be evaluated using direct integration unlike the other tail integrals. The result is as follows:

$$\begin{aligned}\int_{\tilde{\tau}}^{\infty} B_2\tau e^{-j\xi\tau}d\tau &= B_2\left[\frac{j\xi\tau e^{-j\xi\tau} + e^{-j\xi\tau}}{\xi^2}\right]_{\tilde{\tau}}^{\infty} \\ &= -B_2\left[\frac{j\xi\tilde{\tau}e^{-j\xi\tilde{\tau}} + e^{-j\xi\tilde{\tau}}}{\xi^2}\right]\end{aligned} \tag{2.60}$$

which gives a different but more accurate result than (2.59). The use of this final expression in the tail computation for the $G_{\phi\phi}$ component increased the accuracy of the method significantly. This is illustrated in Figure 2.9 for the mutual coupling between two circumferentially oriented dipoles with respect to s. The dimensions are $l_{dip} = 0.39\lambda_0$ and $w_{dip} = 0.01\lambda_0$ with host body parameters $a = 3\lambda_0$, $t_h = 0.06\lambda_0$, $\epsilon_r = 3.25$ at $\alpha = 15°$.

2.6 Pole Location Analysis and the Discussion of a New Numerical Approach

The SDP integration technique for the computation of the Green's function developed in [23]-[24] is also used in [35] to calculate the surface fields of aperture antennas on large coated cylinders. Since the denominators of the Green's functions are the same for both cases, the contour deformation depicted in Figure 2.5 is also applied in [35]. Later, in [36], it is reported that the accuracy and the computation time can be improved by analyzing the pole locations of the Green's functions and changing the integration contour accordingly. This work also showed that in some cases the poles in the second quadrant of the complex ν-plane may move into the third quadrant (the poles in the fourth quadrant moves to first quarter as well due to symmetry) hence the contour deformation depicted in Figure 2.5 may not be mathematically correct.

The main aim in [36] was to perform a contour deformation for C_2 similar to the contour deformation done for C_1 to obtain an exponential decay in the integrand. To accomplish this task, a complete pole analysis is necessary. Some of the results in [36] is reproduced here in Figures 2.10, 2.11. In Figure 2.10, the trajectory of the ψ-values, where the SDP integral is evaluated using a 9-point Gauss-Hermite integration algorithm as α changes from 0° to 55° and $s = 5\lambda_0$, is shown. Figure 2.11.a shows the dominant pole locations for $a = 5.65\lambda_0$, $d = 0.05\lambda_0$, $\epsilon_r = 2$, $s = 5\lambda_0$ and $\alpha = 5° \rightarrow 55°$ (for greater α-values SDP method loses its accuracy) and Figure 2.11.b shows the first higher order pole locations for the same case. In both figures (2.11.a and 2.11.b) a 9-point SDP integration

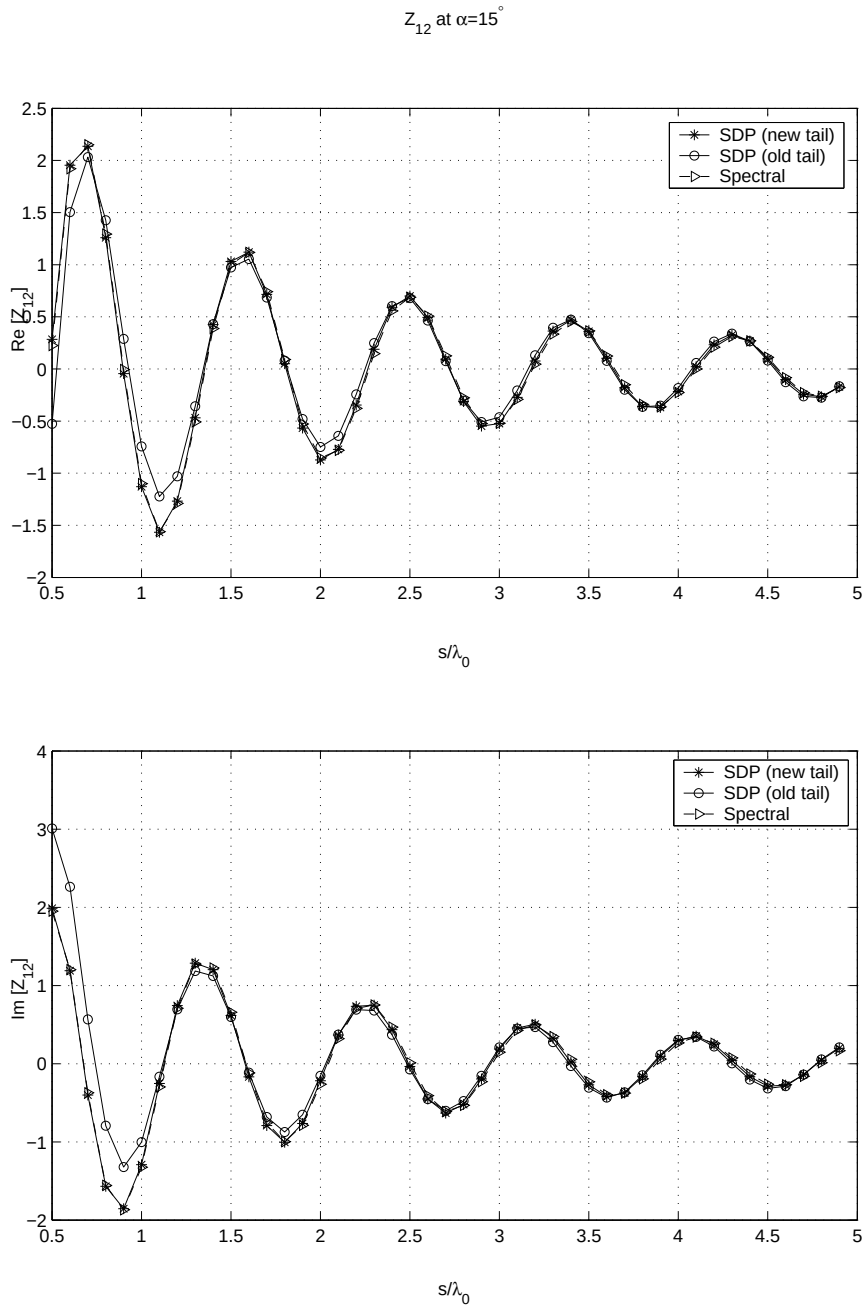

Figure 2.9: Real and imaginary parts of the mutual coupling between two circumferentially oriented dipoles versus separation using SDP method with the new and old tail contribution expressions and spectral domain method at $\alpha = 15°$. ($l_{dip} = 0.39\lambda_0$, $w_{dip} = 0.01\lambda_0$, $a = 3\lambda_0$, $t_h = 0.06\lambda_0$ and $\epsilon_r = 3.25$).

is used. The trajectory of the dominant and first higher-order pole locations with respect to the change of α and ψ-values, given by Figure 2.10, shows the problem of poles moving from the second/fourth quadrants to the third/first quadrants for some values of α and ψ.

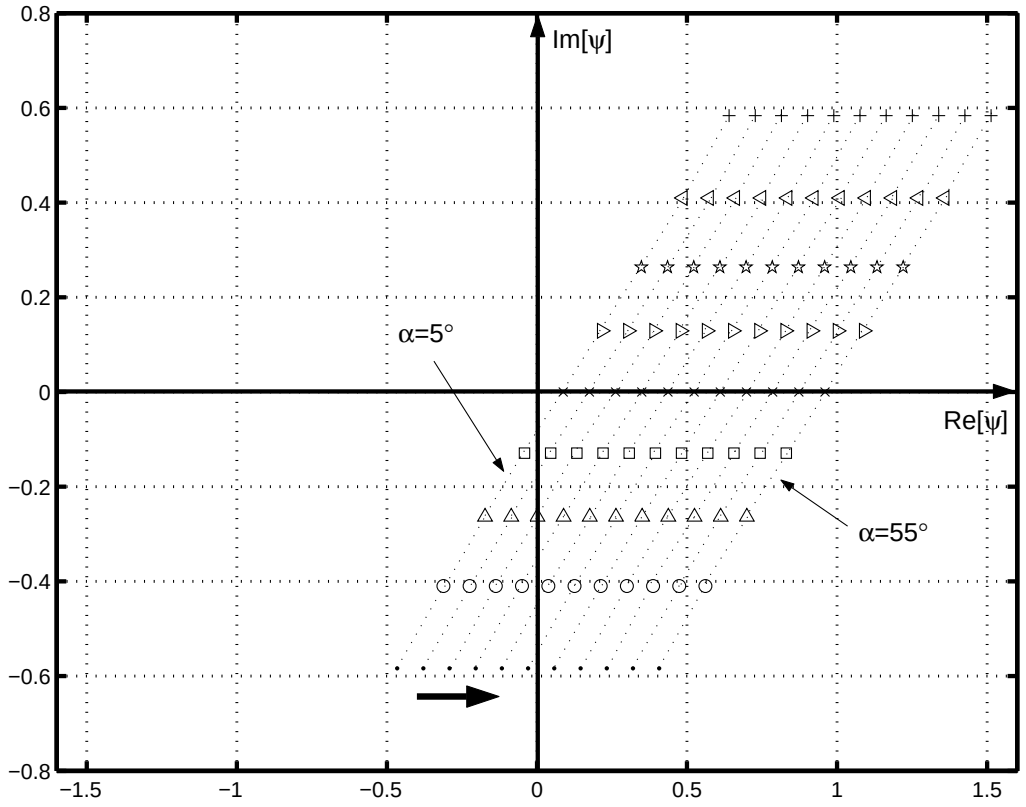

Figure 2.10: The location of the ψ-values used in a 9-point SDP Integration for $\alpha = 5^\circ \rightarrow 55^\circ$ and $s = 5\lambda_0$

Hence, in [36] it is noted that the deformed contour $\tilde{C}_1$ may exclude some poles which, in turn, may yield erroneous results.

It should be noted here that in [23] and [24] different definitions are used for the special functions, which are defined in Appendix B. On the other hand in [36] only uniform representations of these functions, as defined in [37], are used. This change in the representations of the special functions prevent the exclusion of the poles for all the cases tested in ([23]-[24]). Hence, from a practical viewpoint, both methods can be used. However, numerically they may give slightly different

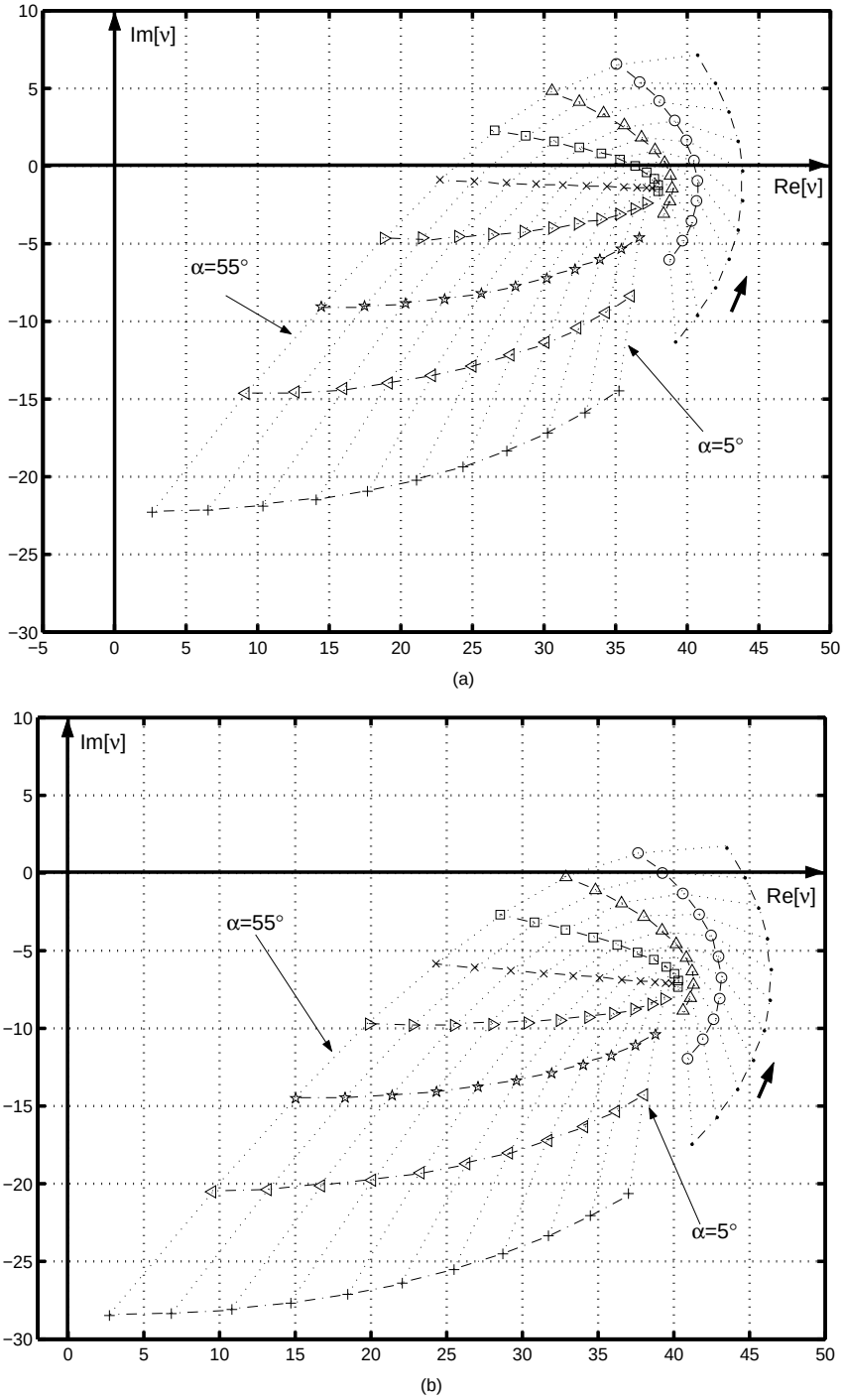

Figure 2.11: The dominant and the first higher-order pole locations as a function of α for a 9-point SDP integration ($a = 5.65\lambda_0$, $d = 0.05\lambda_0$, $\epsilon_r = 2$ and $\alpha = 5^\circ \rightarrow 55^\circ$, $s = 5\lambda_0$).

results for different problems. Also, the deformation of the contour C_2 may provide better computational efficiency, hence it is a good idea to examine this method further. To do the contour deformation, one must be sure that no poles will be excluded when the new contour is used. Fortunately, for a constant value of ψ, the pole locations lie on a line with the dominant pole location close to the $\pm k_{t0}b$ as illustrated in Figure 2.12, where $a = 5.65\lambda_0$, $d = 0.05\lambda_0$, $\epsilon_r = 2$ and $\alpha = 55°$.

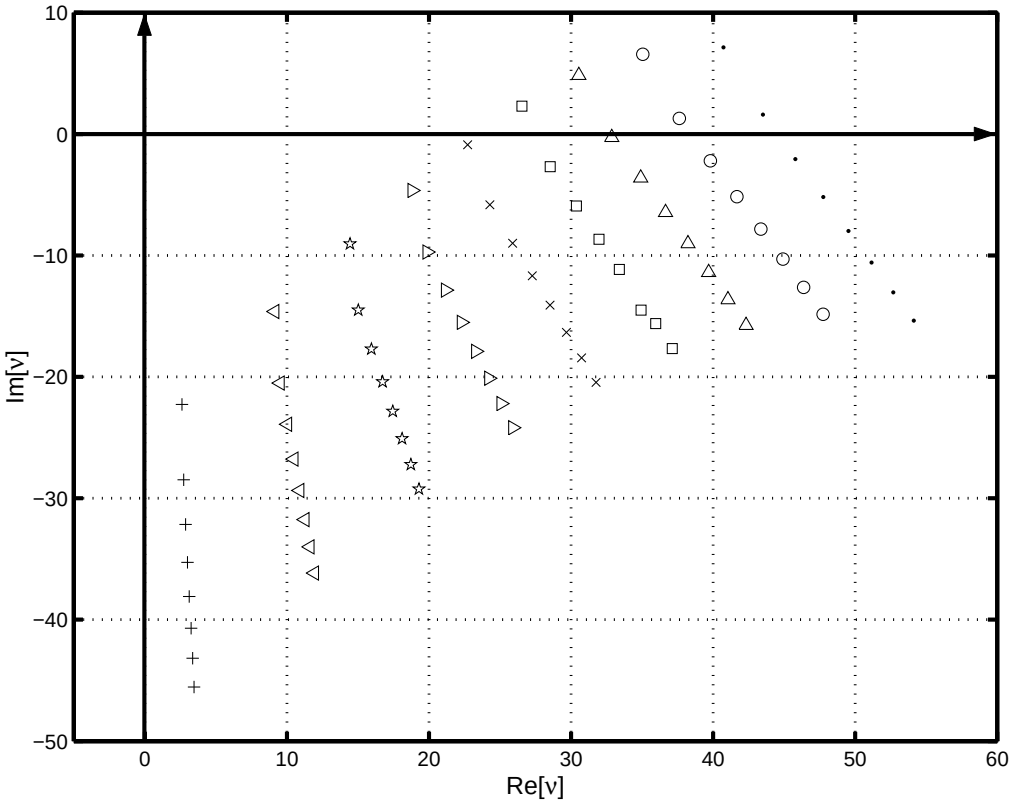

Figure 2.12: The dominant and first 7 higher order pole locations at $\alpha = 55°$ for a 9-point SDP integration ($a = 5.65\lambda_0$, $d = 0.05\lambda_0$ and $\epsilon_r = 2$, $s = 5\lambda_0$).

Thus, when $Re[\nu] > CRe[k_{t0}b]$, the integration contour may be deformed where C is a constant larger than 1 and generally chosen as 1.5. The same contour deformation is also done in the third quarter, i.e $Re[\nu] < CRe[-k_{t0}b]$. Furthermore, one must pay attention not to cross any poles and redeform the contour if a pole lies close to the original contour. In Figure 2.13, the case when

there is a dominant pole in the fourth quarter close to the integration contour and lies inside the integration domain is illustrated. The integration contour is deformed as a half-circle towards the first quadrant such that the dominant pole stays inside the integration domain. Practically, finding only the dominant pole and modifying the integration contour accordingly would be enough if the radius of the deformation is not very large such that any higher order pole is not crossed.

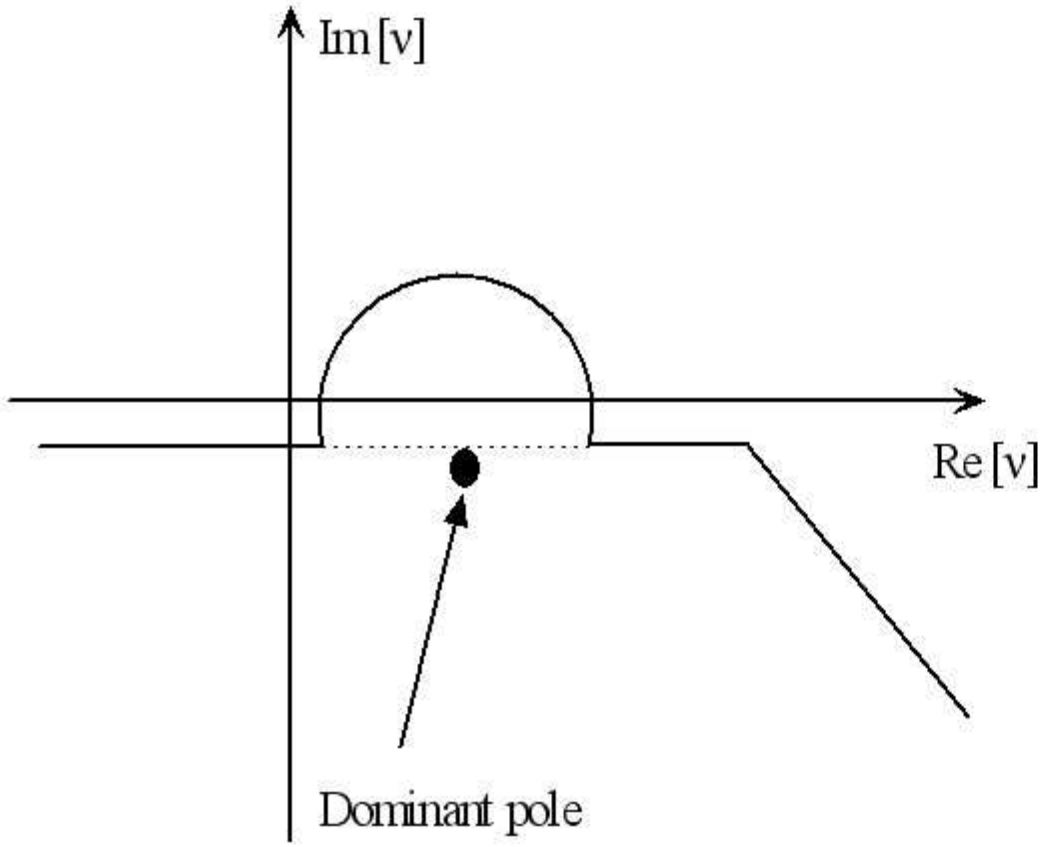

Figure 2.13: Redeformed contour in the ν-plane for the case when a pole lies close to the integration contour.

This new numerical approach presented in [36] is more compact, does not need a tail integration and computationally slightly more efficient than the previous method (although the difference in the computational time is not great). However, in most cases (especially for the $G_{\phi\phi}$ component which is the main focus in this thesis) the original method gives more accurate results. Consequently, the

integration contour given in Figure 2.5 together with the SDP method presented in [23] with the proper tail given by (2.60) is used in this thesis for the SDP representation of the Green's function.

2.7 Fourier Series Representation of Green's Functions

2.7.1 Expressions in the Paraxial Region

To find an expression that works in the paraxial region, the following transformations are applied to (2.32) instead of the Fock's substitutions [33]:

$$k_z = -\zeta cos\psi; \;\; \nu = \mu d \;\; and \;\; \mu = -\zeta sin\psi \tag{2.61}$$

and

$$r_l = d(\phi - \phi') = ssin\delta; \;\; (z - z') = scos\delta \tag{2.62}$$

where $\delta = (90 - \alpha)$. The resulting equation is given by

$$E_l(s, \delta) \approx \frac{1}{2\pi} \int_0^{2\pi} \int_0^{\infty} \frac{G_{lu}(\zeta, \psi)}{2\pi} e^{j\zeta scos(\psi - \delta)} \zeta d\zeta d\psi. \tag{2.63}$$

Also, the zz and $\phi\phi$ components of the Green's function (G_{zz} and $G_{\phi\phi}$) are periodic with respect to ψ with a period π ([23]) such that

$$G_{zz}(\zeta, \psi) = G_{zz}(\zeta, \psi + \pi) \tag{2.64}$$

$$G_{\phi\phi}(\zeta, \psi) = G_{\phi\phi}(\zeta, \psi + \pi). \tag{2.65}$$

Using this periodicity, G_{zz} and $G_{\phi\phi}$ can be approximated by a Fourier series. Since, the main concern of this thesis is the analysis of cylindrical arrays with circumferentially oriented dipoles, the expansion of the G_{zz} component using Fourier Series is explained in Appendix A. The $G_{\phi\phi}$ component is not expanded as a Fourier Series directly since the achieved accuracy is not satisfactory in this case. Instead, it is written as a sum of a planar component $G^{p}_{uu}(\zeta,\psi)$, where u can represent either x or y direction, and $G^{cc}_{\phi\phi}(\zeta,\psi)$ which represents the curvature correction term ([23], [25]) as given by the following equation:

$$G_{\phi\phi}(\zeta,\psi) \approx G^{p}_{uu}(\zeta,\psi) + G^{cc}_{\phi\phi}(\zeta,\psi). \tag{2.66}$$

The planar term which is given by

$$G^{p}_{uu}(\zeta,\psi) = G^{p1}_{uu}(\zeta) - G^{p2}_{uu}(\zeta)\left(\frac{1-cos2\psi}{2}\right)\zeta^2 \tag{2.67}$$

is already in the form of a two-term Fourier Series. Therefore, only the curvature correction term is expanded in a Fourier Series. The resulting Green's function is approximated as ([23])

$$\begin{aligned} G_{\phi\phi}(\zeta,\psi) \;\approx\; & G^{p1}_{uu}(\zeta) + \frac{1}{2}G^{cc}_{\phi\phi}(\zeta,\psi=0) + \Big\{ -\zeta^2 G^{p2}_{uu}(\zeta) \\ & + \frac{1}{2}\left[G^{cc}_{\phi\phi}(\zeta,\psi=\frac{\pi}{2}) - G^{cc}_{\phi\phi}(\zeta,\psi=0)\right]\Big\}\left(\frac{1-cos2\psi}{2}\right). \end{aligned} \tag{2.68}$$

The explicit expressions for curvature correction terms are given in ([23]-[25]). Substituting this Green's function component into (2.63), the surface electric field can be written as

$$E_{\phi\phi}(\delta,s) \;\approx\; \frac{1}{2\pi}\Bigg[\int_0^{\infty} G^{p1}_{uu}(\zeta)\left\{\int_0^{2\pi}\frac{e^{j\zeta scos(\psi-\delta)}}{2\pi}d\psi\right\}\zeta d\zeta$$

$$
\begin{aligned}
&- \int_0^{\infty} G_{uu}^{p2}(\zeta)\zeta^2 \left\{ \int_0^{2\pi} \frac{1-cos2\psi}{4\pi} e^{j\zeta scos(\psi-\delta)} d\psi \right\} \zeta d\zeta \\
&+ \frac{1}{2} \int_0^{\infty} G_{\phi\phi}^{cc}(\zeta, \psi = 0) \left\{ \int_0^{2\pi} \frac{e^{j\zeta scos(\psi-\delta)}}{2\pi} d\psi \right\} \zeta d\zeta \\
&+ \frac{1}{2} \int_0^{\infty} \left[G_{\phi\phi}^{cc}(\zeta, \psi = \frac{\pi}{2}) - G_{\phi\phi}^{cc}(\zeta, \psi = 0) \right] \\
&\left\{ \int_0^{2\pi} \left(\frac{1-cos2\psi}{4\pi} \right) e^{j\zeta scos(\psi-\delta)} d\psi \right\} \zeta d\zeta \Bigg].
\end{aligned} \tag{2.69}
$$

As explained in Appendix A, the integrals with respect to ψ can be evaluated analytically. Substituting these closed-form results (equation (A.7)-(A.10)) into the equations (2.69) and (A.6), the final expressions for both $E_{\phi\phi}$ and E_{zz} components of the electric field are found as follows:

$$
E_{zz}(\delta, s) \approx \frac{-Z_0}{2\pi k_0} \left\{ k_0^2 P(s) + \frac{\partial^2}{\partial z^2} [P(s) - Q(s)] \right\} \tag{2.70}
$$

$$
\begin{aligned}
E_{\phi\phi}(\delta, s) \approx\ & \frac{-Z_0}{2\pi k_0} \left\{ k_0^2 U(s) + \frac{\partial^2}{\partial r_l^2} \left[U(s) - \frac{\epsilon_r - 1}{\epsilon_r} W(s) \right] \right\} \\
& + \frac{jZ_0}{4\pi k_0} \left\{ S(s) + \frac{\partial^2}{\partial r_l^2} T(s) \right\}.
\end{aligned} \tag{2.71}
$$

The special functions $P(s)$, $Q(s)$, $U(s)$, $W(s)$, $S(s)$ and $T(s)$ are explicitly given in [23]. The integrals in these expressions do not cause numerical problems like the integrations in the SDP representation of the Green's function and hence they are easily evaluated along the real axis using a Gaussian-quadrature algorithm.

2.7.2 Expressions in the Off-paraxial Region for $G_{\phi\phi}$ component of the Green's function

In Appendix A, it is mentioned that the Fourier Series coefficients are approximated via the trapezoidal rule such that the results are accurate in the paraxial

region. However, it is possible to use different approximations for the Fourier Series coefficients to obtain results that are accurate in regions other than the paraxial region [23]. It should be noted that since these equations are based on approximations, to find an accurate representation requires extensive numerical testing. The off-paraxial results for the Fourier Series representation of the Green's function is currently not available for $G_{zz}(\zeta, \psi)$ component.

For $\delta \rightarrow \pi/2$, the following approximate expression for the curvature correction term of the $G_{\phi\phi}$ component of the Green's function is obtained ([23]);

$$\begin{aligned} G^{cc}_{\phi\phi}(\zeta, \psi) &\approx G^{cc}_{\phi\phi}(\zeta, \psi = 0) \\ &\quad + \left[G^{cc}_{\phi\phi}(\zeta, \psi = \frac{\pi}{2}) - G^{cc}_{\phi\phi}(\zeta, \psi = 0)\right] \left(\frac{1 - cos2\psi}{2}\right) \end{aligned} \quad (2.72)$$

As $\delta \rightarrow \pi/4$, based on some numerical experimentation ([23]), accurate results are obtained if the expression given by

$$\begin{aligned} G^{cc}_{\phi\phi}(\zeta, \psi) &\approx \frac{3}{4}\Bigg\{G^{cc}_{\phi\phi}(\zeta, \psi = 0) \\ &\quad + \left[G^{cc}_{\phi\phi}(\zeta, \psi = \frac{\pi}{2}) - G^{cc}_{\phi\phi}(\zeta, \psi = 0)\right] \left(\frac{1 - cos2\psi}{2}\right) \Bigg\}, \end{aligned} \quad (2.73)$$

is used for the curvature correction term. The Fourier Series representation of the Green's function gets more accurate for small separations between the source and the observation points. Also, since the integration is only with respect to the variable ζ, it is computationally very efficient. Hence, it is preferable to use the Fourier Series representation of the Green's function even in the off-paraxial region for small separations when it is available instead of the SDP representation of the Green's function.

Chapter 3

Array Concepts

3.1 Introduction

In this chapter, array related concepts and definitions are given. In section 3.2, a general introduction to phased arrays is made. Their benefits and application fields are explained. Some basic performance metrics that are used to analyze the performance of arrays are defined in section 3.3. Among these basic performance metrics, input impedance and active reflection coefficient of the dipoles can be found directly by using the results obtained from the MoM procedure. However, for the calculation of the far-field pattern additional theoretical knowledge is required. Hence, a method based on stationary phase method for the evaluation of the far-field pattern ([38]) is explained in this section. Finally, in section 3.4 scan blindness phenomenon is discussed. Scan blindness, if happens, limits the scan range of the array which is an important concern in the design of arrays.

3.2 Phased Arrays

According to the American Federal Standard 1037C ([39]) a phased array is defined as "A group of antennas in which the relative phases of the respective signals

feeding the antennas are varied in such a way that the effective radiation pattern of the array is reinforced in a desired direction and suppressed in undesired directions. The relative amplitudes of, and constructive and destructive interference effects among, the signals radiated by the individual antennas determine the effective radiation pattern of the array. A phased array may be used to point a fixed radiation pattern, or to scan rapidly in azimuth or elevation."

Phased arrays have a wide range of applications in both military and civilian life ([1]-[4]). For example, it is desirable for a radar to be able to scan different directions. If a conventional antenna would be used for such a purpose, a rotatory system would be required to direct the maximum radiation at a desired scan angle. This solution would not be cost effective and the mechanical rotation system would introduce a delay that is not desirable. However, in a phased array by changing the excitations of the individual elements this goal is easily achieved. That is why the phased arrays are also called "scanning arrays". The ease in changing the radiation pattern of the phased array provides many opportunities. It is possible to adjust the beamwidth, bandwidth and polarization, to form multiple beam networks, reduce sidelobe level or eliminating the interference like the military jammer signals with the deep nulls in the pattern.

As discussed in section 2.2, in the case of an array on a cylinder, for scanning in the (θ_i, ϕ_i) direction, the voltage excitation of the pq^{th} dipole is given by:

$$V_{pq} = e^{-jk_0 sin\theta_i dcos(\phi_i - p\Delta\phi)} e^{-jk_0 cos\theta_i q d_z}. \tag{3.1}$$

3.3 Basic Performance Metrics

An antenna or an array is designed under some constraints to meet specific needs. Hence, to analyze the performance of the array and to see how its performance changes with the change of array and host body parameters have a primary importance.

An important point of interest for an array is its radiation characteristics. The antennas are generally used for receiving information from or transmitting information to long distances. Thus, the far-field approximations may be used in the pattern calculations. The far-field pattern of a single dipole can be found using the methods described in either [38] where asymptotic techniques are used or [40] where a reciprocity approach is used. Using the stationary phase method described in [38], the components of the electric field due to a current distribution tangential to a coated cylinder can be written as follows:

$$E_\theta(r,\theta,\phi) = -j\eta_0 k_0 \frac{e^{-jk_0 r}}{\pi r} sin\theta \sum_{n=-\infty}^{\infty} j^n e^{jn\phi} C_m(n,k_z)$$

$$E_\phi(r,\theta,\phi) = -jk_0 \frac{e^{-jk_0 r}}{\pi r} sin\theta \sum_{n=-\infty}^{\infty} j^n e^{jn\phi} C_e(n,k_z) \tag{3.2}$$

where η_0 is the intrinsic impedance of free-space. $C_m(n,k_z)$ and $C_e(n,k_z)$ are found from the following matrix relation:

$$\begin{bmatrix} C_m(n,k_z) \\ C_e(n,k_z) \end{bmatrix} = \overline{\mathbf{M}}^{-1}(n,k_z) \begin{bmatrix} \tilde{J}_{sz}(n,k_z) \\ \tilde{J}_{s\phi}(n,k_z) \end{bmatrix} \tag{3.3}$$

$\tilde{J}_{sz}(n,k_z)$ and $\tilde{J}_{s\phi}(n,k_z)$ are related to the components of current in the z- and ϕ-directions and given by

$$\tilde{J}_{sz}(n,k_z) = b \int\int_{S'} J_z(z',\phi') e^{-jn\phi'} e^{jk_z z} d\phi' dz'$$

$$\tilde{J}_{s\phi}(n,k_z) = b \int\int_{S'} J_\phi(z',\phi') e^{-jn\phi'} e^{jk_z z} d\phi' dz'. \tag{3.4}$$

Also in (3.3)

$$\overline{\mathbf{M}} = \begin{bmatrix} M_{11} & M_{12} \\ M_{21} & M_{22} \end{bmatrix} \tag{3.5}$$

with

$$M_{11}(n,k_z) = \beta_m T'_m - k_{\rho 2} H_n^{(2)'}(k_{\rho 2} b) - \frac{n k_z}{j\eta_0 k_0 b} T_e \gamma_m \tag{3.6}$$

$$M_{12}(n,k_z) = \frac{n k_z}{j\eta_0 k_0 b}\left[H_n^{(2)}(k_{\rho 2} b) - T_e \gamma_e\right] \tag{3.7}$$

$$M_{21}(n,k_z) = \frac{k_{\rho 1}^2}{j\eta_0 k_0} T_e \gamma_m \tag{3.8}$$

$$M_{22}(n,k_z) = \frac{1}{j\eta_0 k_0}\left[k_{\rho 1}^2 T_e \gamma_e - k_{\rho 2}^2 H_n^{(2)}(k_{\rho_2} b)\right] \tag{3.9}$$

where

$$k_{\rho 1} = k_0\sqrt{\epsilon_r - cos^2\theta} \;\text{ and }\; k_{\rho 2} = k_0 sin\theta \tag{3.10}$$

$$\beta_m = \frac{\epsilon_r k_{\rho 2}^2}{k_{\rho 1}^2}\frac{H_n^{(2)}(k_{\rho 2} b)}{T_m} \tag{3.11}$$

$$\gamma_m = \frac{\eta_0 k_0(\epsilon_r - 1)}{jb}\frac{n k_z}{k_{\rho 1}^2}\frac{H_n^{(2)}(k_{\rho 2} b)}{T'_e} \tag{3.12}$$

$$\gamma_e = k_{\rho 2}\frac{H_n^{(2)'}(k_{\rho 2} b)}{T'_e} \tag{3.13}$$

$$T_e = H_n^{(1)}(k_{\rho 1} b) - \alpha_e H_n^{(2)}(k_{\rho 1} b) \tag{3.14}$$

$$T'_e = k_{\rho 1}\left[H_n^{(1)'}(k_{\rho 1} b) - \alpha_e H_n^{(2)'}(k_{\rho 1} b)\right] \tag{3.15}$$

$$T_m = H_n^{(1)}(k_{\rho 1}b) - \alpha_m H_n^{(2)}(k_{\rho 1}b) \tag{3.16}$$

$$T'_m = k_{\rho 1}\left[H_n^{(1)'}(k_{\rho 1}b) - \alpha_m H_n^{(2)'}(k_{\rho 1}b)\right] \tag{3.17}$$

with

$$\alpha_m = \frac{H_n^{(1)}(k_{\rho 1}a)}{H_n^{(2)}(k_{\rho 1}a)}, \quad \alpha_e = \frac{H_n^{(1)'}(k_{\rho 1}a)}{H_n^{(2)'}(k_{\rho 1}a)}. \tag{3.18}$$

To find the electric field due to a single element of a finite, phased array of circumferentially or axially oriented printed dipoles on an electrically large, coated cylinder ($E^d(\overrightarrow{r})$), the suitable one of the basis functions defined in (2.5) is used as the current source. The far-field pattern of the array is then obtained by superposing the far-fields of the individual elements using the mode currents that are found from the MoM procedure as follows:

$$E(\overrightarrow{r}) = \sum_{n=-N}^{N} \sum_{m=-M}^{M} A_{nm} E^d(\overrightarrow{r}). \tag{3.19}$$

Another performance metric is the input impedance of a dipole on the array. The input impedance is, according to the IEEE Std 145-1983 ([41]), "the impedance presented by an antenna at its terminals or the ratio of the voltage to current at a pair of terminals or the ratio of appropriate components of the electric to magnetic fields at a point". In an infinite phased array, since the input impedance of all the elements is the same and changes with the scan angle, it may be named as the "scan impedance" [1]. In this work the ratio of the voltage to current at the antenna terminals is used to calculate the input impedance. Hence the input impedance of the nm^{th} dipole is given by:

$$Z_{in}^{nm}(\theta, \phi) = \frac{V_{nm}}{I_{nm}} \tag{3.20}$$

where V_{nm} is the voltage excitation of the nm^{th} dipole given by (2.10) and I_{nm} is the current on the nm^{th} dipole which is found via the MoM.

Final performance metric that will be addressed here is the active reflection coefficient of a dipole. Reflection results due to a mismatch between two different impedances. If the array is conjugate matched to the broadside scan impedance of the middle element of the array, the active reflection of the nm^{th} dipole is defined as ([27]):

$$R_{nm}(\theta,\phi) = \frac{Z_{in}^{nm}(\theta,\phi) - Z_{in}^{mid}(\theta = 90^{\circ}, \phi = 0^{\circ})}{Z_{in}^{nm}(\theta,\phi) + Z_{in}^{mid*}(\theta = 90^{\circ}, \phi = 0^{\circ})} \tag{3.21}$$

In this equation, Z_{in}^{mid} is the input impedance of the middle element of the array and "$*$" denotes the complex conjugate. The reason for this matching is to be consistent with the infinite array case. In the infinite array case, the active reflection coefficient is the same for all elements since the input impedance does not vary for different array elements. However, in the finite array case the input impedance is not constant which necessitates choosing one of the array elements as a reference. The edge effects on the middle element of the array is minimal, thus its input impedance is closest to the infinite array case. Therefore, in order to compare the performances of infinite arrays and finite arrays, choosing the middle element as the reference for the finite arrays makes the most sense. Lowering the active reflection coefficient will result in better radiation efficiency and hence it is an important concern in the design of the antennas. The active reflection coefficient is also used to determine the scan blindness, which is explained in section 3.4.

3.4 Scan Blindness

Scan blindness is a phenomenon that seriously degrades a system's performance by reducing the scan range. Therefore, to prevent scan blindness or at least moving it away from the broadside is very important in an array design.

The studies on scan blindness (for antennas on grounded dielectric slab) have begun for infinite planar printed dipole arrays ([42]). For the infinite array case, at scan blindness no real power enters or leaves the array. Therefore the active reflection coefficient of all the elements are same and equal to unity at scan blindness. Due to the conservation of power, at the scan blindness angles "forced surface waves" are created instead of radiated/scattered fields. Therefore, an array should be on or near a structure that can support a surface wave like the dielectric coating in our case for the scan blindness to occur. Physically, in an infinite planar array at scan blindness, the surface waves are confined in the structure forever which explains the unity reflection coefficient for all array elements. Hence, scan blindness can be defined as a phase matching between the phase progression of a surface wave (β_{sw}) on the dielectric substrate and the phase progression of a certain transverse Floquet mode. Mathematically, this can be written as follows:

$$\left(\frac{\beta_{sw}}{k_0}\right)^2 = \left(\frac{n\lambda_0}{d_x} + u\right)^2 + \left(\frac{m\lambda_0}{d_y} + v\right)^2 \tag{3.22}$$

where m and n are integers representing a Floquet mode, d_x and d_y are the center-to center distance between the elements of the array and u and v are given by

$$u = sin\theta cos\phi; \quad v = sin\theta sin\phi. \tag{3.23}$$

The situation for a finite planar array is explored in [27]. For finite arrays, the active reflection coefficient is not the same for all elements. Hence, in scan blindness some elements may have active reflection coefficients of magnitude greater than unity while others have it less than unity. From a conservation of power perspective, the power of other elements must be transferred to the elements with active reflection coefficients' greater than unity at this situation. Those elements then return some of the power to their generators, which may cause the system to break down or burn. Practically, this situation may happen even before the scan blindness which further shows the importance of the scan blindness analysis.

In finite arrays, at scan blindness some power is still transmitted or received by the array unlike the infinite array case. However, a big dip in gain is generally observed. In Figure 3.1, a result presented in [27] is reproduced to show the difference between the reflection coefficient magnitude of a 19x19 planar dipole array and an infinite planar dipole array in E- and H- planes. The geometry of a finite, phased array of printed dipoles on a coated planar array is given in Figure 3.2. The reflection coefficient of the finite array is computed at the broadside scan for the center element. The center-to-center distances between the dipoles in x- and y-directions, d_x and d_y, are equal to $0.5\lambda_0$, the thickness of the substrate is $t_h = 0.19\lambda_0$, the dimensions of each dipole is $l_{dip} = 0.39\lambda_0$ to $w_{dip} = 0.01\lambda_0$ and the dielectric constant of the substrate is $\epsilon_r = 2.55$. This figure shows that the reflection coefficient magnitude of the finite array is greater than unity at the scan blindness which occurs at about $\theta = 46^\circ$ in the E-plane. In H-plane scan blindness does not occur. Physically, this is due to the strong coupling of the surface waves in the E-plane.

One property of the scan blindness is it happens before the onset of the grating lobe [43]. For a phased array antenna the onset of the grating lobe is given by the equation

$$\frac{S}{\lambda_0} = \frac{1}{1 + |sin\theta_m|} \tag{3.24}$$

where

S=element separation
λ_0=free-space wavelength
θ_m=maximum angular scan .

From this equation it can be seen that decreasing the element spacing may increase the scan range. Although the maximum angular scan term used here describes only the scan area where there are no grating lobes and does not take scan blindness into account, it still gives insight on where the scan blindness may occur and how the scan range may be improved.

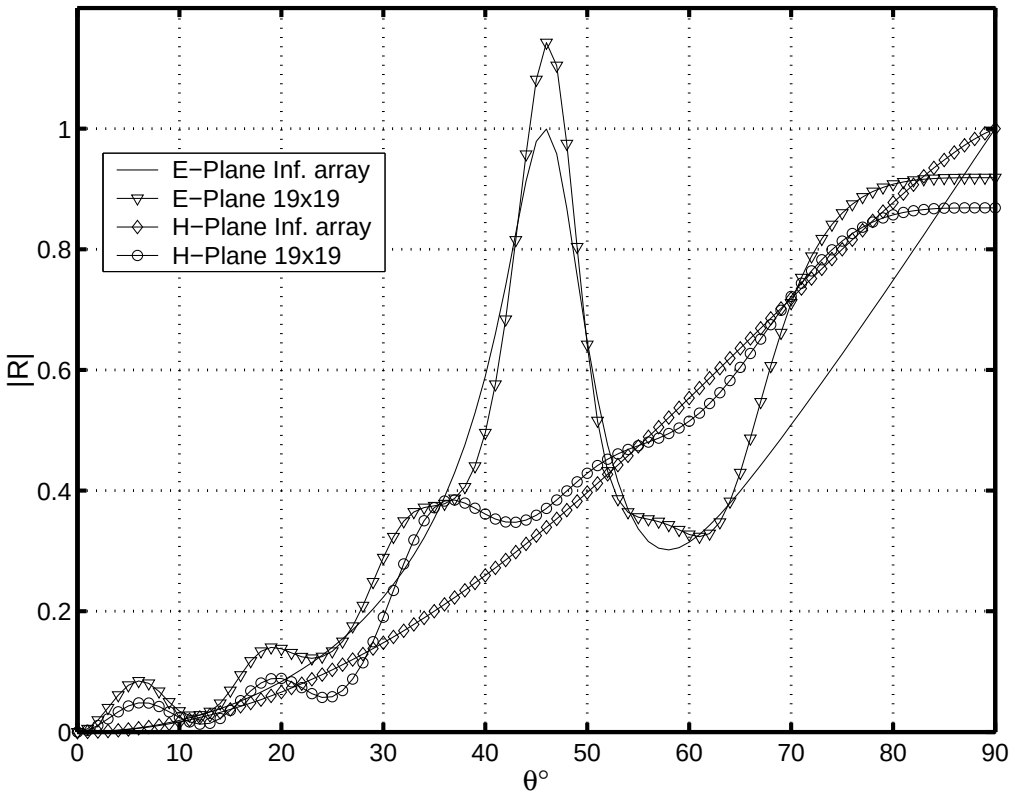

Figure 3.1: Reflection coefficient magnitude of the middle element vs. scan angle for a 19x19 planar array and an infinite planar array in E- and H- planes. ($d_x = d_y = 0.5\lambda_0$, $t_h = 0.19\lambda_0$, $l_{dip} = 0.39\lambda_0$, $w_{dip} = 0.01\lambda_0$, $\epsilon_r = 2.55\lambda_0$).

The works on scan blindness for planar arrays have shown that scan blindness is affected by substrate and array parameters like t_h, ϵ_r, d_x, d_y and the number of elements. However, a study of scan blindness for finite, phased arrays of printed dipoles on electrically large, coated cylinders have not been made before. The results of this work have revealed the importance of the curvature on the scan blindness. Due to the curvature of the cylinder, finite phased arrays of circumferentially and axially oriented printed dipoles on an electrically large, coated cylinder and a finite planar phased array of printed dipoles show very different behavior in terms of scan blindness. Several numerical examples for various array and host body parameters like thickness of the substrate, array size and cylinder radius are presented and discussed in chapter 4.

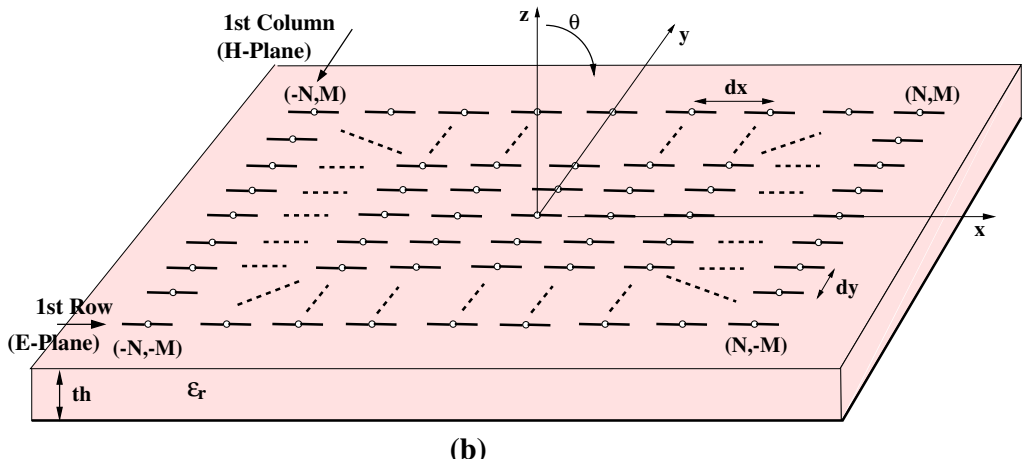

Figure 3.2: The geometry of a finite, phased array of printed dipoles on a grounded dielectric slab.

Chapter 4

Numerical Results

4.1 Introduction

In this chapter, numerical results are presented to explain and support the theory presented in the previous chapters. The aim of this part is twofold:

- To assess the accuracy of the spatial-domain method.
- To analyze the effects of several array and host body parameters on the performance metrics of the cylindrical arrays of circumferentially oriented dipoles and compare it with those of the cylindrical arrays of axially oriented dipoles and planar arrays.

The results, in terms of induced current envelope, mutual coupling, active reflection coefficient and far-field pattern, are presented and discussed. Special attention is given to the active reflection coefficient results to be able to analyze the scan blindness phenomenon thoroughly. The array geometries are given in Figures 2.1, 2.2 for the cylindrical arrays and in Figure 3.2 for the planar array. The parameters that are common for all of the results in this chapter are the length of the dipoles $l_{dip} = 0.39\lambda_0$, width of the dipoles $w_{dip} = 0.01\lambda_0$, the periodicity of the arrays in circumferential and axial directions (x- and y- directions

for the planar array) $d_z = d_{rl} = d_x = d_y = 0.5\lambda_0$ for the array results and relative dielectric constant of the dielectric coating $\epsilon_r = 3.25$. It should be noted that some of the results in this chapter are presented in several conferences ([46]-[49]).

4.2 Mutual Coupling and Accuracy of the Hybrid/MoM Green's Function Method

The first set of results presented in this section are mutual coupling results between two circumferentially oriented dipoles on an electrically large coated cylinder that compares Green's function representations in spatial domain to Green's function representation in the spectral domain. As discussed in section 2.2, the accuracy and efficiency of the moment method solution depends on the computation of the Green's function. Therefore, the Green's function representations must be accurate for arbitrary source and observation points. In Figures 4.1-4.4, the real and imaginary parts of mutual coupling results for the FS representation, SDP representation and spectral domain representation of the Green's function are compared at $\alpha = 0°$, $\alpha = 30°$, $\alpha = 45°$ and $\alpha = 60°$, respectively (α is the angle between the geodesic path connecting the two dipoles and the circumferential direction as shown in Figure 2.6), $a = 3\lambda_0$ and $t_h = 0.06\lambda_0$. In Figure 4.5, only FS and spectral representations are compared since SDP representation does not work in this region. The parameters are same as the ones used in 4.1-4.4. The FS representation is very accurate around $\alpha = 0°$, $\alpha = 45°$ and $\alpha = 90°$ but in the transition regions and when the separation s is large it tends to get less accurate. On the other hand, SDP representation is very accurate in the off-paraxial region. Although this representation loses its accuracy as $\alpha \rightarrow 90°$, it is still accurate when s is large at $\alpha = 60°$ where FS does not give very good results. Hence, these two representations complement each other very well to obtain a valid solution on the whole solution region.

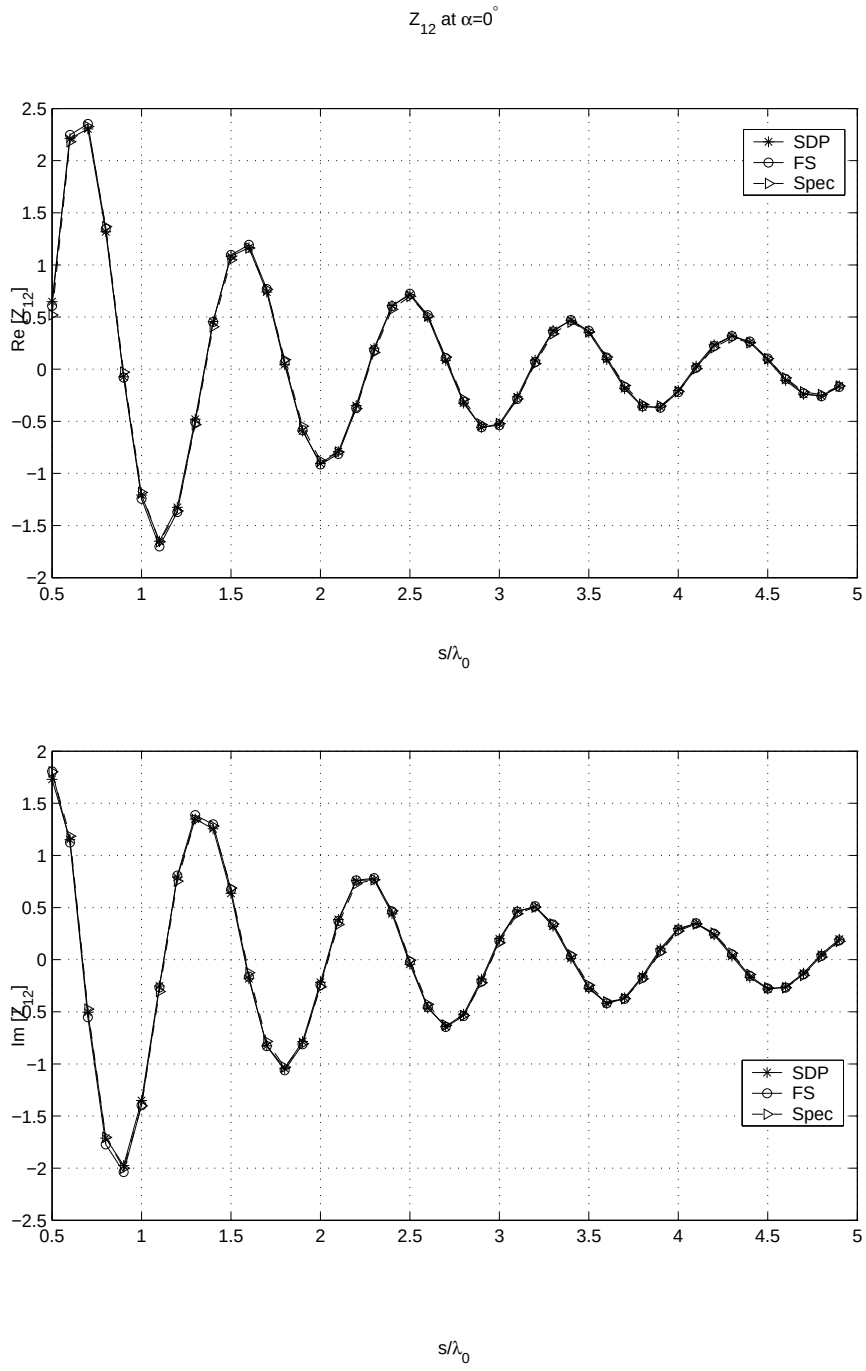

Figure 4.1: Real and imaginary parts of the mutual coupling between two circumferentially oriented printed dipoles versus separation using the SDP method (with the new tail contribution), FS method and spectral domain method at $\alpha = 0°$ ($l_{dip} = 0.39\lambda_0$, $w_{dip} = 0.01\lambda_0$, $d_z = d_{rl} = 0.5\lambda_0$, $a = 3\lambda_0$, $t_h = 0.06\lambda_0$, $\epsilon_r = 3.25$).

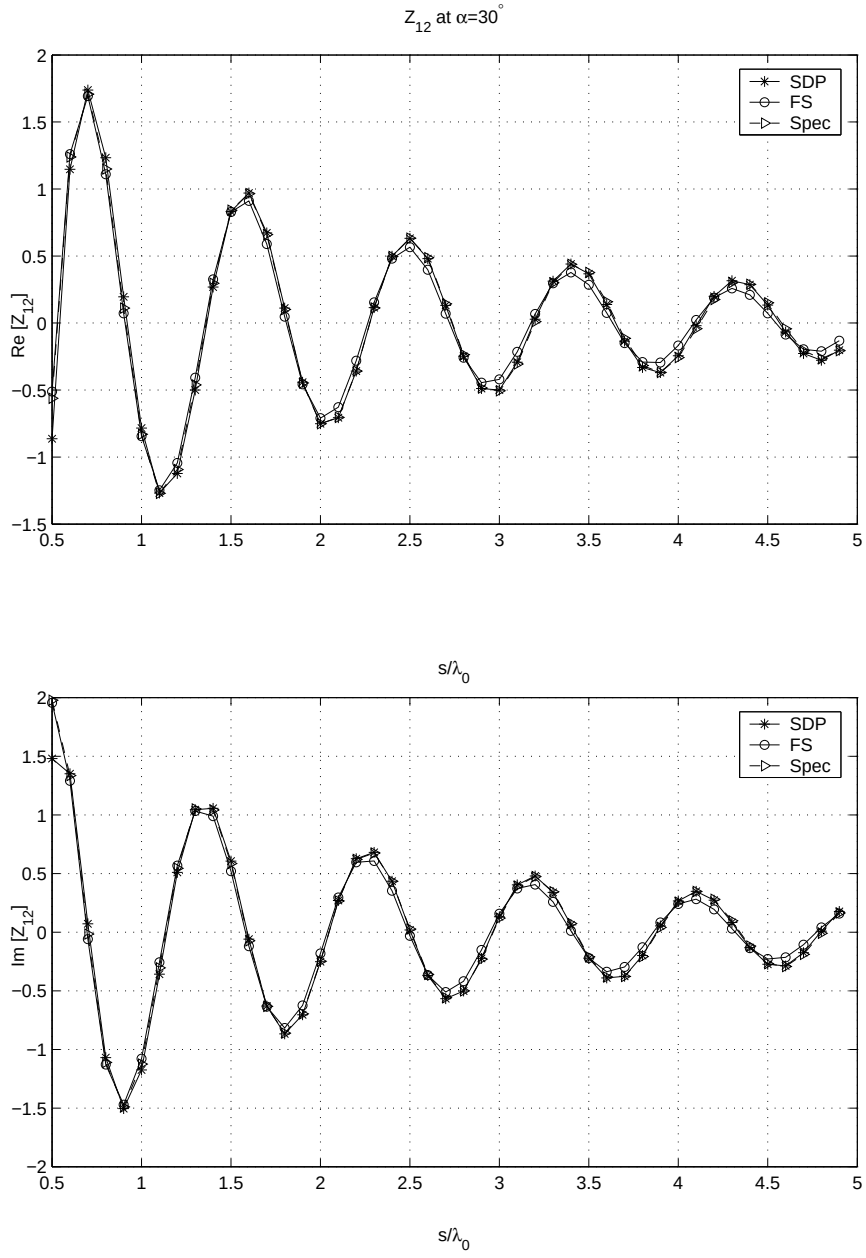

Figure 4.2: Real and imaginary parts of the mutual coupling between two circumferentially oriented printed dipoles versus separation using the SDP method (with the new tail contribution), FS method and spectral domain method at $\alpha = 30°$ ($l_{dip} = 0.39\lambda_0$, $w_{dip} = 0.01\lambda_0$, $d_z = d_{rl} = 0.5\lambda_0$, $a = 3\lambda_0$, $t_h = 0.06\lambda_0$, $\epsilon_r = 3.25$).

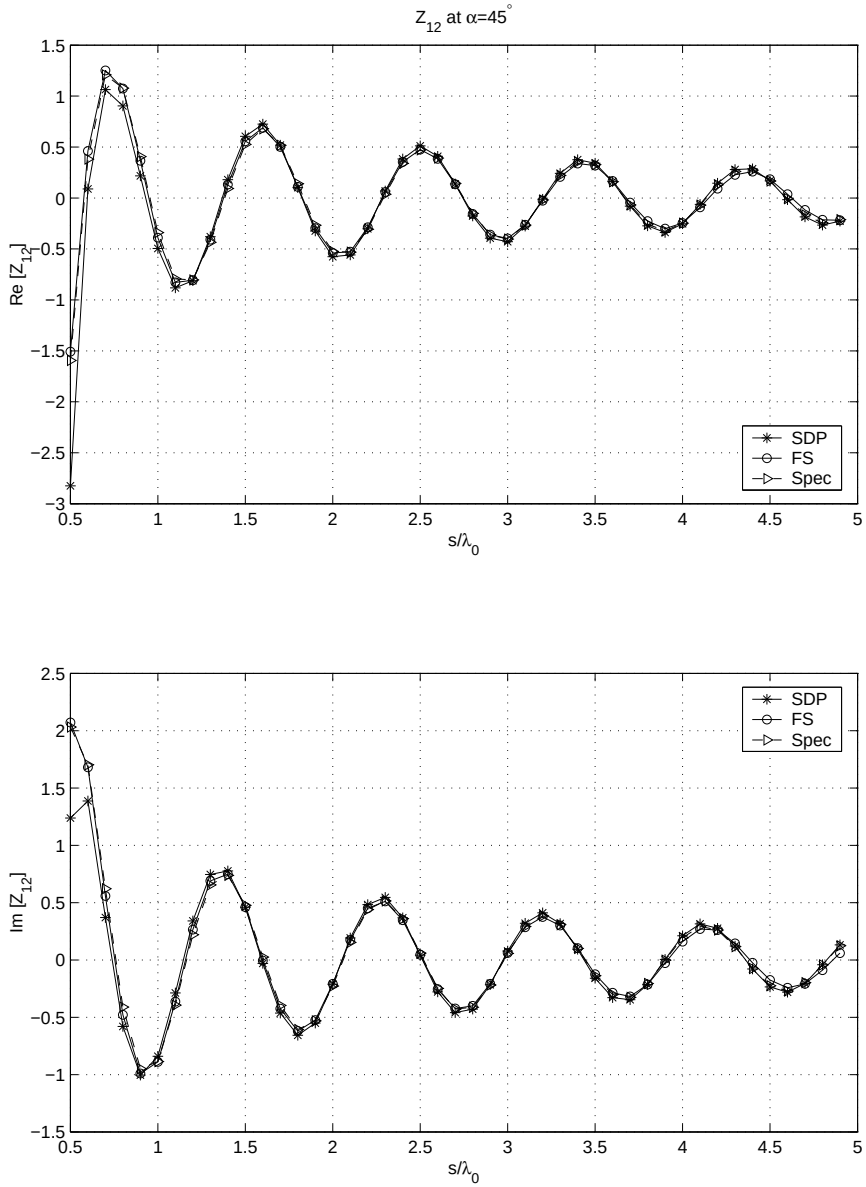

Figure 4.3: Real and imaginary parts of the mutual coupling between two circumferentially oriented printed dipoles versus separation using the SDP method (with the new tail contribution), FS method and spectral domain method at $\alpha = 45°$ ($l_{dip} = 0.39\lambda_0$, $w_{dip} = 0.01\lambda_0$, $d_z = d_{rl} = 0.5\lambda_0$, $a = 3\lambda_0$, $t_h = 0.06\lambda_0$, $\epsilon_r = 3.25$).

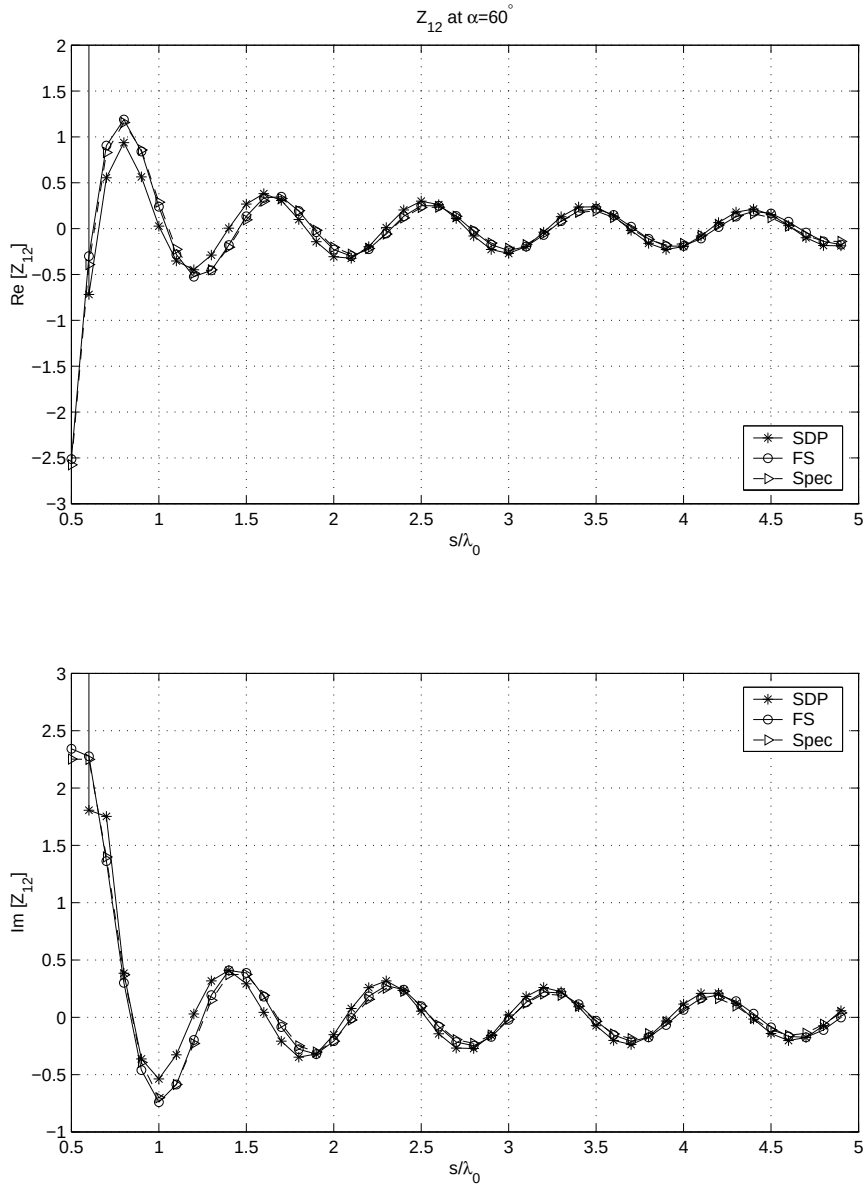

Figure 4.4: Real and imaginary parts of the mutual coupling between two circumferentially oriented printed dipoles versus separation using the SDP method (with the new tail contribution), FS method and spectral domain method at $\alpha = 60^\circ$ ($l_{dip} = 0.39\lambda_0$, $w_{dip} = 0.01\lambda_0$, $d_z = d_{rl} = 0.5\lambda_0$, $a = 3\lambda_0$, $t_h = 0.06\lambda_0$, $\epsilon_r = 3.25$).

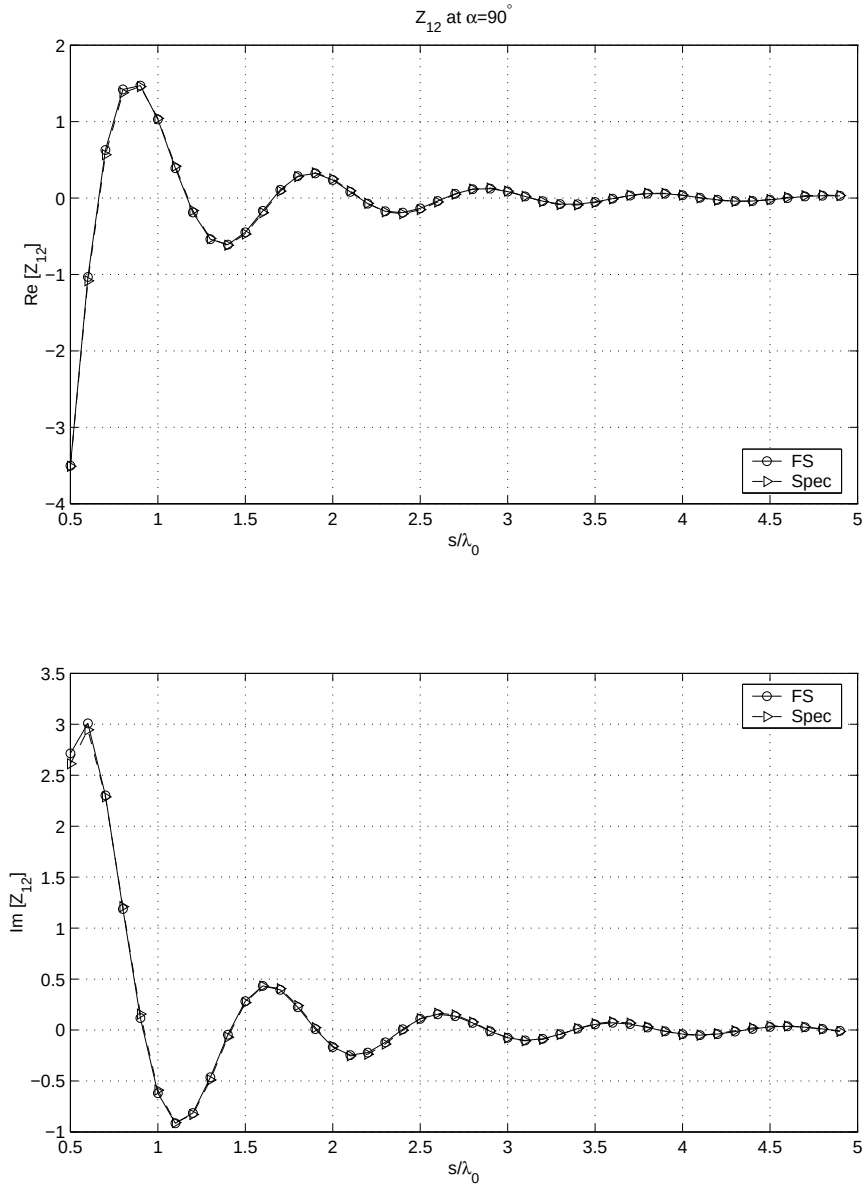

Figure 4.5: Real and imaginary parts of the mutual coupling between two circumferentially oriented printed dipoles versus separation using the FS method and spectral domain method at $\alpha = 90^\circ$ ($l_{dip} = 0.39\lambda_0$, $w_{dip} = 0.01\lambda_0$, $d_z = d_{rl} = 0.5\lambda_0$, $a = 3\lambda_0$, $t_h = 0.06\lambda_0$, $\epsilon_r = 3.25$).

Figures 4.6 and 4.7 show the mutual coupling results between two dipoles which are circumferentially and axially oriented, respectively versus the center-to-center separation between the dipoles s for cylinders with different radii. These results are also compared with planar results. In the spatial domain results, the second ray contribution corresponding to $p = 1$ in equation (2.31) is also considered. This contribution gets bigger as the separation between the dipoles increases. The interference of these two rays is seen as an oscillation in the figures. Another point to be noted is the coupling in the H-plane is dominated by the space waves. The space waves are initially bigger in magnitude than the surface waves when the separation s is small, but they decay at a higher rate when s becomes larger. As a result, the coupling in H-plane is very weak for large separations. However, in the E-plane surface waves are dominant. Hence, there is a strong coupling even for the large separations. Also, the coupling for the planar and circumferentially oriented dipoles cases are very close in the H-plane while the coupling of the cylindrical array is much weaker in the E-plane compared to planar array. Similarly, for the axially oriented dipoles the coupling is a little stronger than planar case in E-plane while it is much weaker in H-plane. This is because in the circumferential direction (which corresponds to E-plane for the circumferentially oriented dipoles and H-plane for the axially oriented dipoles) shedding occurs due to the curvature effect which reduces the surface fields' strength. However, similar to a water arc in the fluid dynamics, the fields are confined better than the planar case in the axial direction hence the coupling on the cylinder is stronger in this direction.

The next results presented are comparisons of induced current envelopes (A_{nm} in equation 2.5) between spectral and spatial methods case for the first and middle rows and first and middle columns of a 5x5 cylindrical array. Figure 4.8-a shows the results when the dipoles in the array are circumferentially oriented and Figure 4.8-b shows the case when the dipoles are axially oriented. The radius of the cylinder is $a = 4\lambda_0$ and the thickness of the dielectric coating is $t_h = 0.06\lambda_0$. In these figures, a uniform excitation is assumed for the array elements such that $V_{pq} = 1$ in equation (2.10) with the aim of comparing the accuracy of the solution for both uniform and phased excitation. It can be seen that the results are nearly

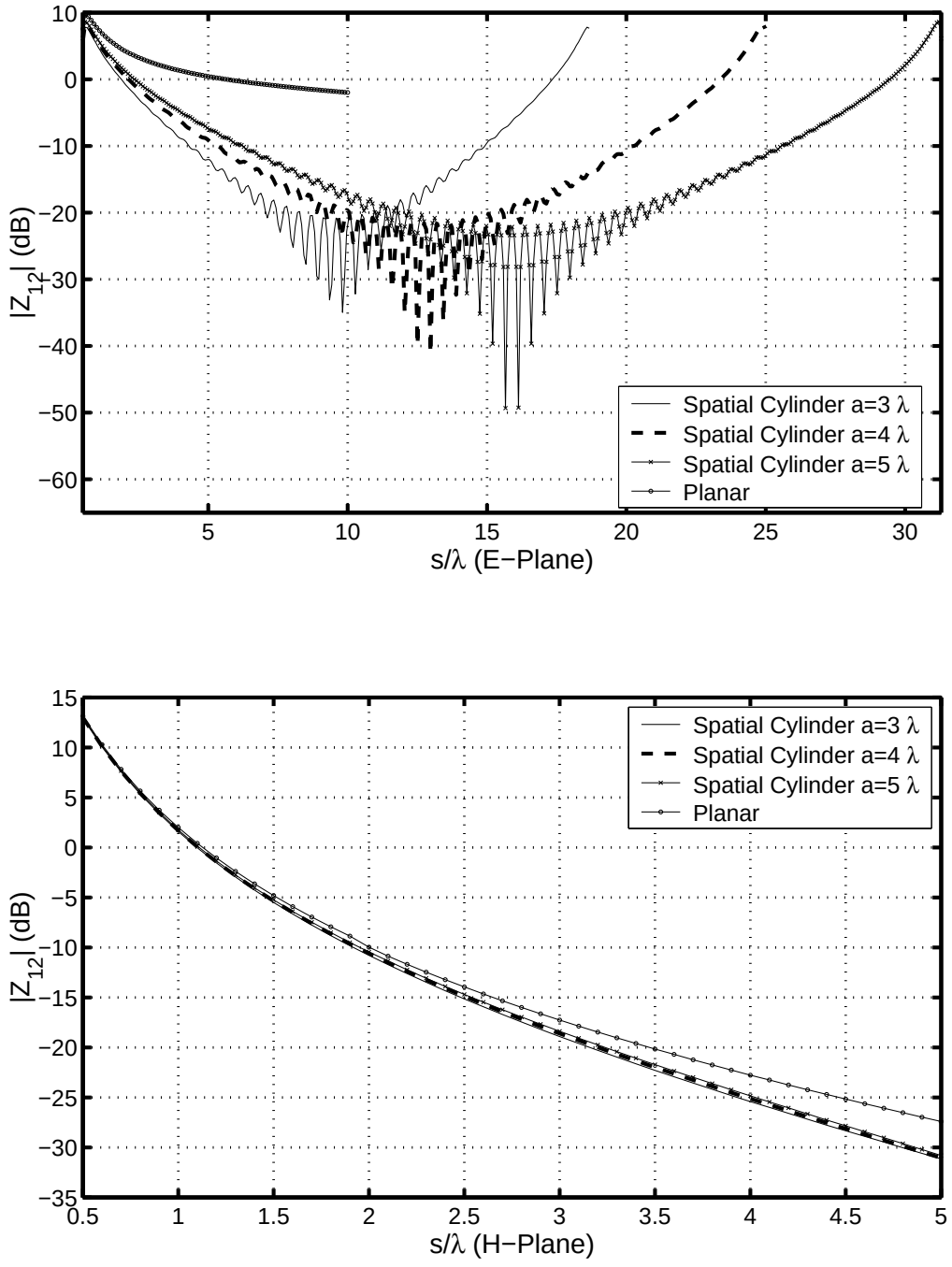

Figure 4.6: Mutual coupling between two circumferentially oriented dipoles versus separation s for different radii and comparison with the planar case ($l_{dip} = 0.39\lambda_0$, $w_{dip} = 0.01\lambda_0$, $d_z = d_{rl} = d_x = d_y = 0.5\lambda_0$, $t_h = 0.06\lambda_0$, $\epsilon_r = 3.25$).

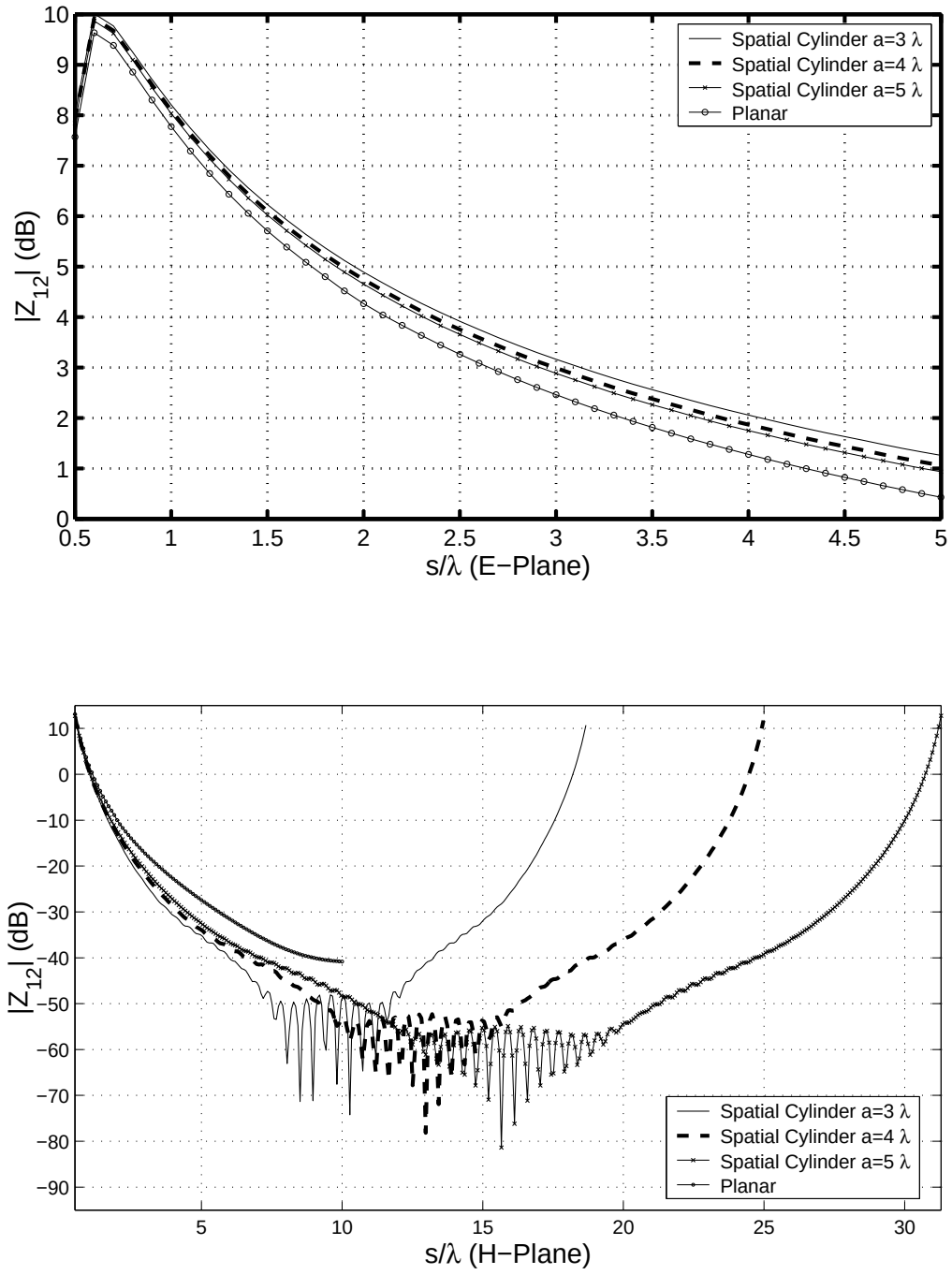

Figure 4.7: Mutual coupling between two axially oriented dipoles versus separation s for different radii and comparison with the planar case ($l_{dip} = 0.39\lambda_0$, $w_{dip} = 0.01\lambda_0$, $d_z = d_{rl} = d_x = d_y = 0.5\lambda_0$, $t_h = 0.06\lambda_0$, $\epsilon_r = 3.25$).

identical for the spectral and spatial methods.

Figures 4.9-a and 4.9-b compares the induced current envelopes for the spatial and spectral domain solutions in the first row, first column, middle row and the middle column of a 7x7 cylindrical array of circumferentially and axially oriented dipoles, respectively for $a = 3\lambda_0$ and $t_h = 0.06\lambda_0$. The phase excitation of equation (2.10) is used in this figure. Again the results are close. For larger arrays, the spectral domain solution begins to show convergence problems. Therefore, for the rest of the results in this chapter only spatial domain MoM/Green's function technique results are presented, since it is more accurate and more efficient (approximately 10 times) than the spectral domain results. Furthermore, as the radius of the cylinder and/or the number of elements increase, the difference in the fill-time of the impedance matrix strongly favors the spatial domain technique ([28]).

In Figure 4.10 the induced current envelope comparison between a 11x11 cylindrical array and a 11x11 planar array is shown for the first row, first column, middle row and the middle column of the array for $a = 3\lambda_0$ and $t_h = 0.06\lambda_0$. There is a considerable amount of difference between the magnitudes of current for planar and cylindrical arrays which shows the importance of the curvature. Therefore, approximations of cylindrical arrays using planar arrays, which is a common practice in the design of cylindrical arrays, may lead to unsatisfactory results for applications where accuracy is a primary concern.

4.3 Performance of the Cylindrical Arrays of Circumferentially Oriented Dipoles

In this section the performance of finite, phased array of circumferentially oriented dipoles on electrically large, coated cylinders are compared with those of arrays of axially oriented dipoles and planar arrays. The results are given in terms of active reflection coefficient versus scan angle, active reflection coefficient versus element number and far-field pattern. The phase excitation given by (2.10) is used in all the results. In Figure 4.11-a, the magnitude of the active reflection coefficients in

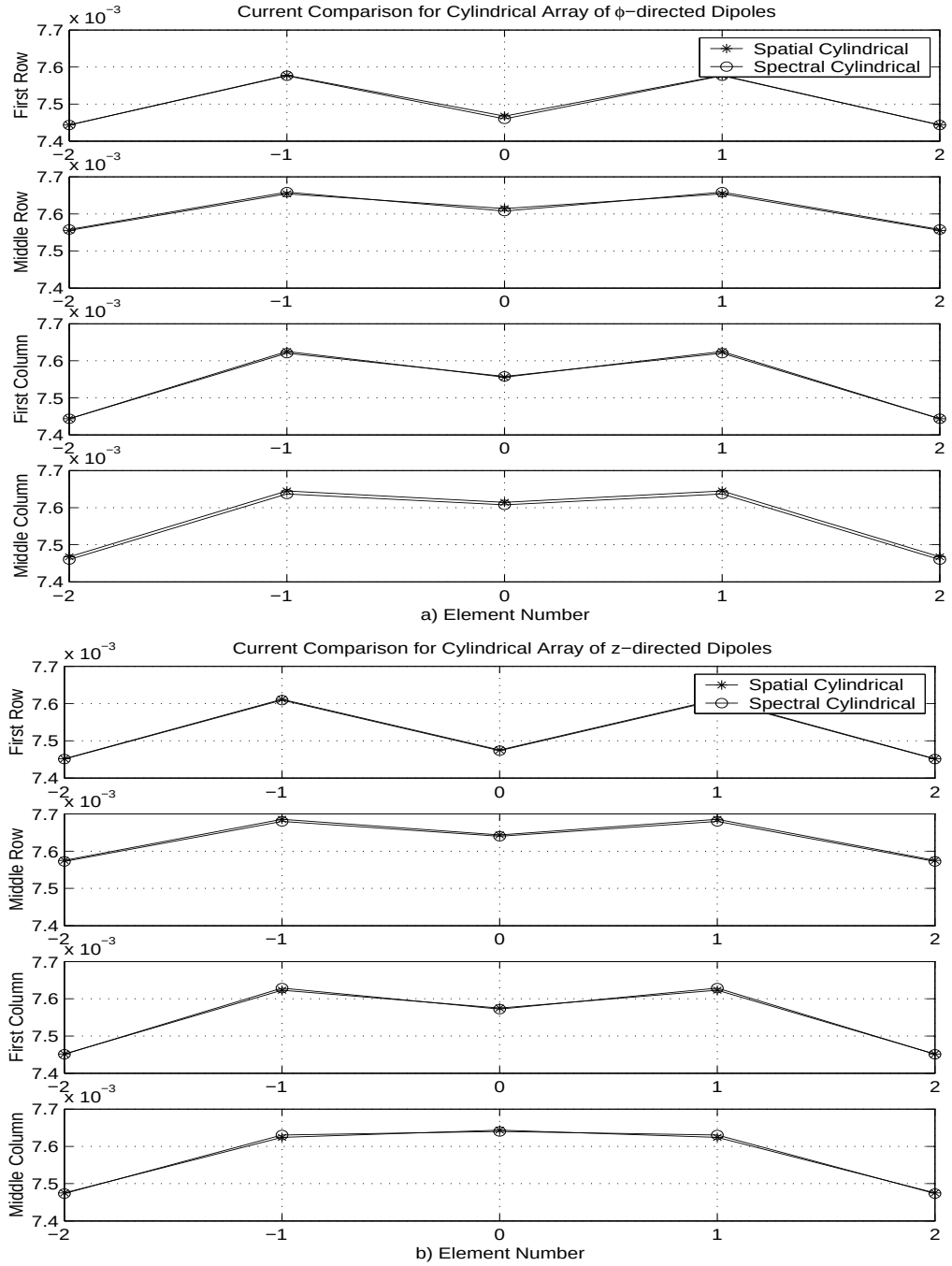

Figure 4.8: Current comparison between spectral and spatial methods for a 5x5 cylindrical array of a) circumferentially oriented dipoles, b) axially oriented dipoles ($l_{dip} = 0.39\lambda_0$, $w_{dip} = 0.01\lambda_0$, $d_z = d_{rl} = d_x = d_y = 0.5\lambda_0$, $a = 4\lambda_0$, $t_h = 0.06\lambda_0$, $\epsilon_r = 3.25$).

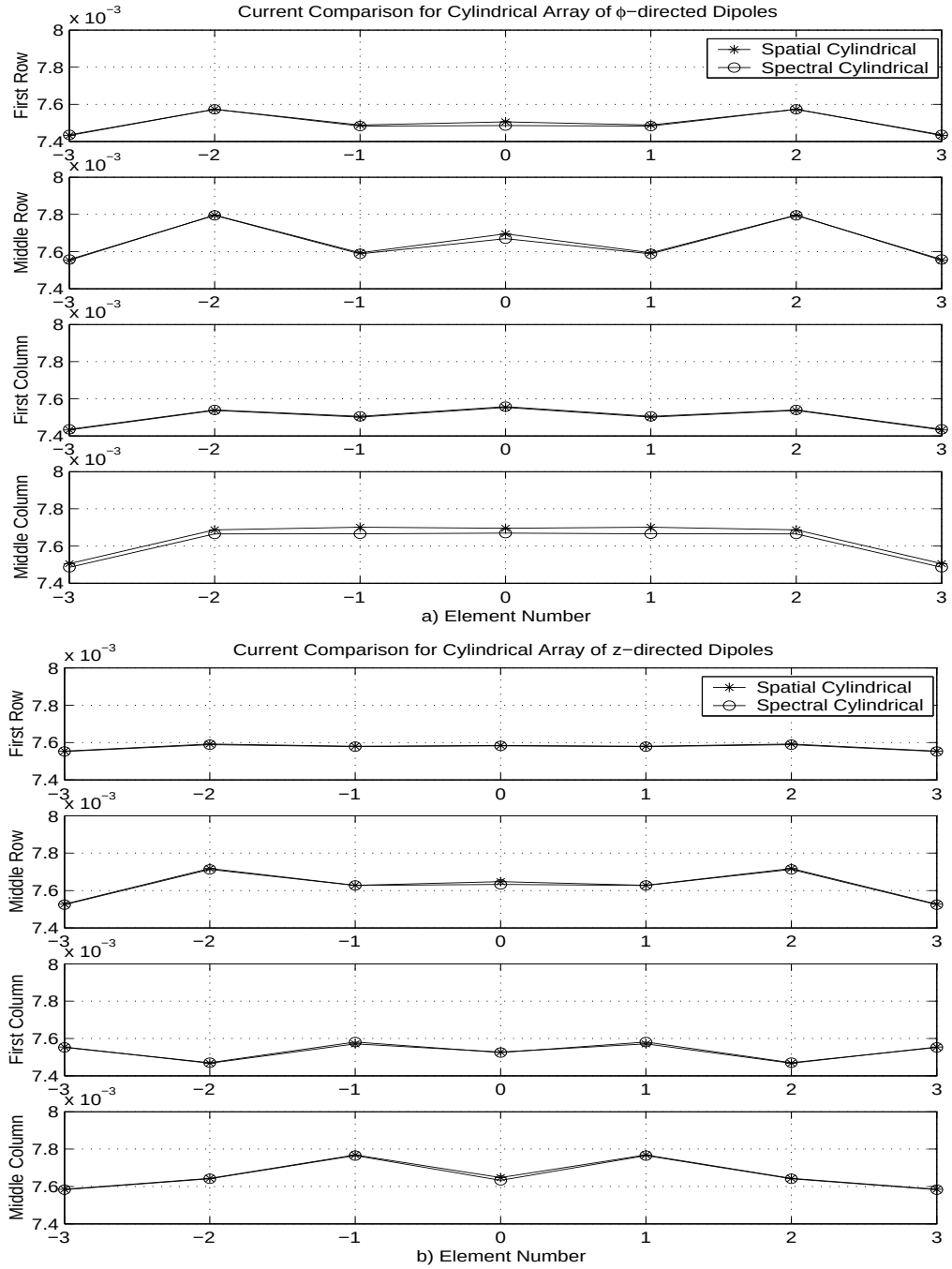

Figure 4.9: Current comparison between spectral and spatial methods for a 7x7 cylindrical array of a) circumferentially oriented dipoles, b) axially oriented dipoles ($l_{dip} = 0.39\lambda_0$, $w_{dip} = 0.01\lambda_0$, $d_z = d_{rl} = d_x = d_y = 0.5\lambda_0$, $a = 3\lambda_0$, $t_h = 0.06\lambda_0$, $\epsilon_r = 3.25$).

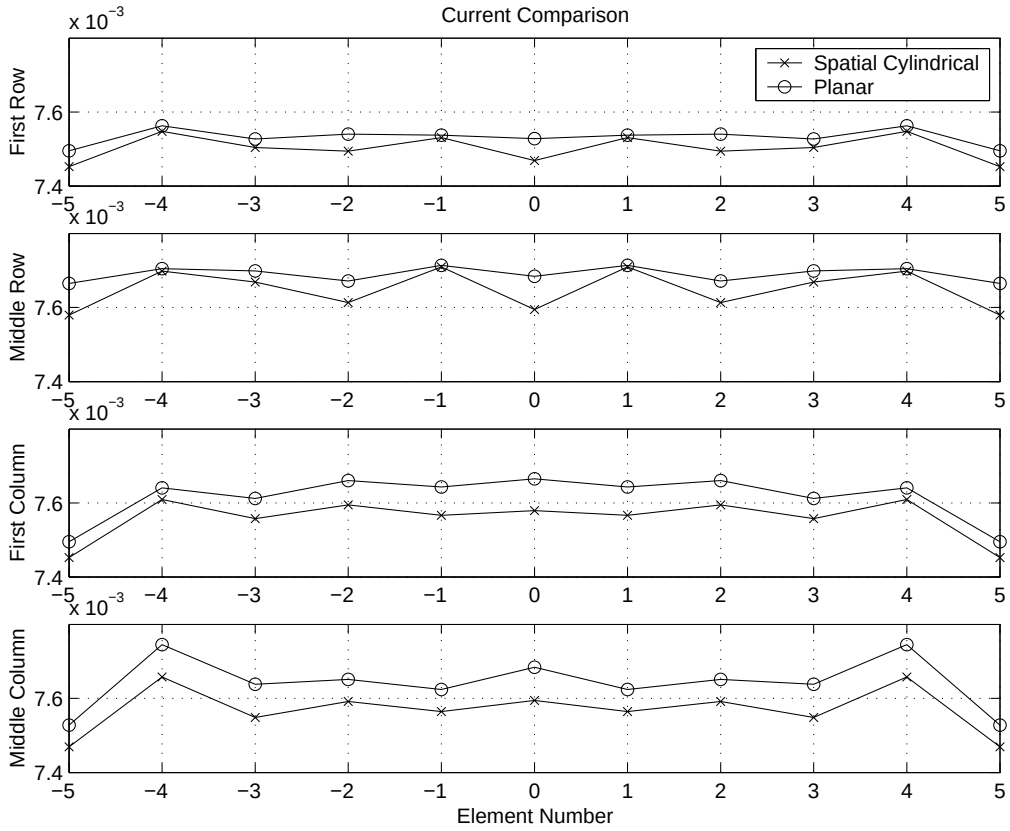

Figure 4.10: Current comparison between a 11x11 cylindrical array of circumferentially oriented dipoles and a 11x11 planar array ($l_{dip} = 0.39\lambda_0$, $w_{dip} = 0.01\lambda_0$, $d_z = d_{rl} = d_x = d_y = 0.5\lambda_0$, $a = 3\lambda_0$, $t_h = 0.06\lambda_0$, $\epsilon_r = 3.25$).

the E-plane between 11x11 cylindrical array of circumferentially directed dipoles, 11x11 cylindrical array of axially directed dipoles and 11x11 planar array are compared for the middle elements of the arrays. The radius of the cylinder for cylindrical arrays is $a = 3\lambda_0$ and thickness of the dielectric coating is $t_h = 0.06\lambda_0$. In 4.11-b the same comparison is made in the H-plane. It should be noted here that for scanning in the E-Plane

- For the cylindrical array of circumferentially oriented dipoles $\theta = 90^\circ$ and ϕ is changing,
- For the cylindrical array of axially oriented dipoles $\phi = 0^\circ$ and $(90 - \theta)$ (since the direction of the scan is from the broadside towards the end-fire)

is changing,

- For the planar array $\phi = 0°$ and θ is changing.

Similarly, for scanning in the H-plane,

- For the cylindrical array of circumferentially oriented dipoles $\phi = 0°$ while $(90 - \theta)$ is changing,
- For the cylindrical array of axially oriented dipoles $\theta = 90°$ and ϕ is changing,
- For the planar array $\phi = 90°$ and θ is changing.

Also in E-plane, while scan blindness occurs for the cylindrical arrays of axially oriented dipoles, cylindrical arrays of circumferentially oriented dipoles do not exhibit scan blindness due to the shedding which reduces the surface waves' strength. Therefore, the orientation of the dipoles also affects the scan blindness unlike the planar array case ([27],[42])

Figure 4.12-a shows the active reflection coefficient versus scan angle results in the E-Plane for 11x11 cylindrical arrays of circumferentially oriented printed dipoles mounted on coated cylinders with radii $3\lambda_0$, $4\lambda_0$ and $5\lambda_0$ and $t_h = 0.06\lambda_0$. The results are also compared with that of a 11x11 planar array in the E-plane. The same result is shown in Figure 4.12-b for a cylindrical array of axially oriented dipoles. As the radius of the cylinder increases results for the cylindrical arrays more closely resemble those of the planar arrays which is a further proof to the accuracy of the spatial method since in the limiting case where the radius of the cylinder goes to infinity a planar array is obtained. Scan blindness phenomenon is observed at approximately $(90 - \theta) = 49°$ for cylindrical array of axially oriented dipoles when $a = 3\lambda_0$. For arrays with $a = 4\lambda_0$, $a = 5\lambda_0$ and planar array, although the reflection coefficient's magnitude tend to get very big at this angle, exact scan blindness is not observed. This is due to the fact that when the radius of the cylinder is smaller, the fields are better confined in the axial direction as mentioned before. However, for the cylindrical arrays of circumferentially

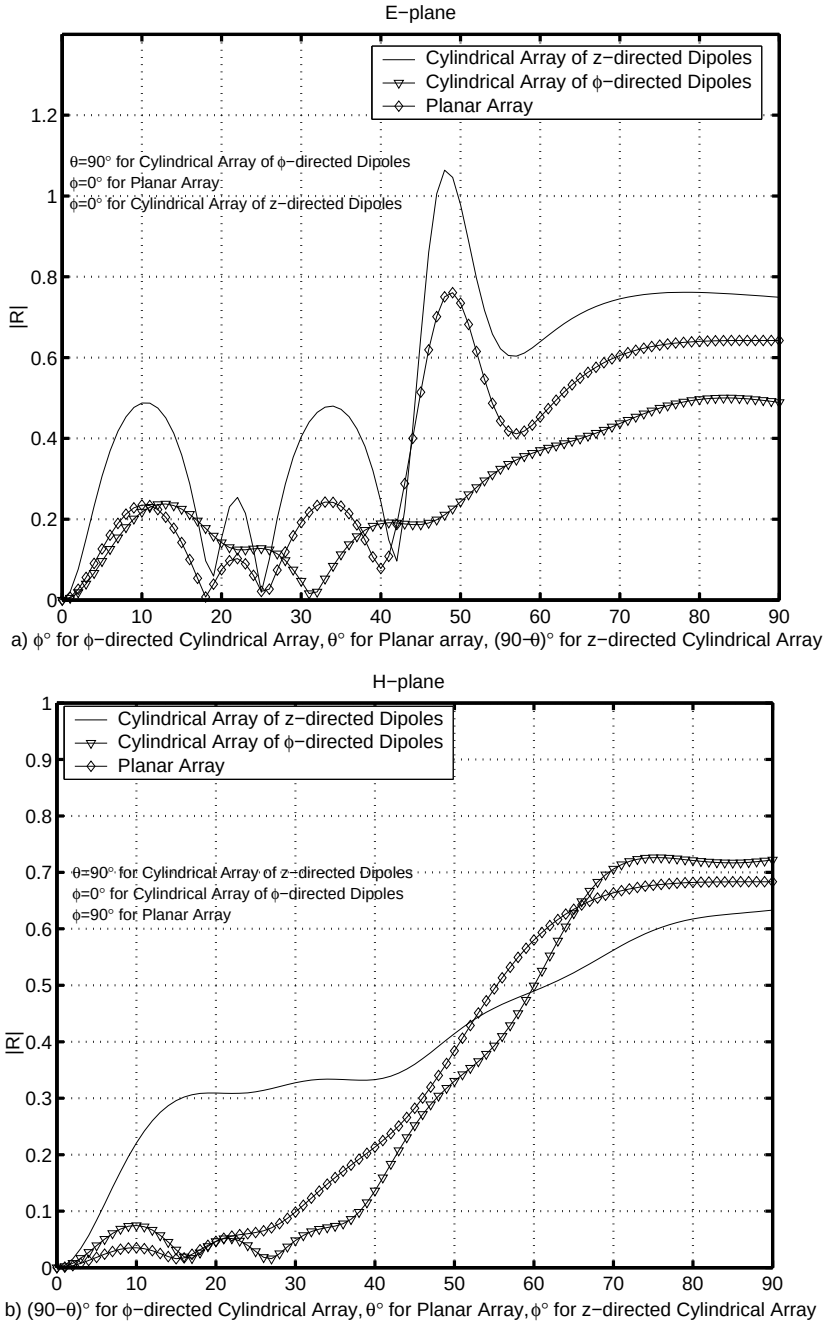

Figure 4.11: Magnitude of reflection coefficient of the middle element vs. scan angle comparison for 11x11 cylindrical arrays of circumferentially and axially oriented dipoles and comparison with a 11x11 planar array in a) E-Plane and b) H-Plane ($l_{dip} = 0.39\lambda_0$, $w_{dip} = 0.01\lambda_0$, $d_z = d_{rl} = d_x = d_y = 0.5\lambda_0$, $a = 3\lambda_0$, $t_h = 0.06\lambda_0$, $\epsilon_r = 3.25$).

oriented dipoles the magnitude of the reflection coefficient in the E-plane is not bigger than 0.5 because of the curvature effects which causes surface waves to be weaker.

Figures 4.13-a and 4.13-b show the same results for the H-plane scan. In this plane, the scan blindness phenomenon is not observed since the surface waves are not strong in this direction as mentioned before. The reflection coefficient for the cylindrical arrays of circumferentially oriented dipoles are slightly bigger in this case than the cylindrical arrays of axially oriented dipoles due to the curvature effects.

In Figure 4.14-a, the magnitude of the active reflection coefficient in the E-plane between 11x11 cylindrical array of circumferentially directed dipoles, 11x11 cylindrical array of axially directed dipoles and 11x11 planar array is compared for a thickness of $t_h = 0.02\lambda_0$, and the radius of the cylinder for cylindrical arrays is $a = 3\lambda_0$. In 4.14-b the same comparison is made in the H-plane. The decrease in the thickness of the dielectric coating reduces the strength of the surface waves and hence scan blindness is not observed for this case.

In Figures 4.15 and 4.16, Figures 4.12 and 4.13 are repeated for $t_h = 0.02\lambda_0$ with all the other parameters being the same. As the radius of the cylinder increases in the plane corresponding to the circumferential direction (E-plane for cylindrical arrays of circumferentially directed dipoles and H-Plane for cylindrical arrays of axially directed dipoles), the coupling and hence the active reflection coefficient increases due to the curvature effect. However, in the axial direction the increase of the radius reduces the coupling as mentioned before, which in turn causes a smaller active reflection coefficient.

In the next figure (4.17), the effect of the array size on the reflection coefficient is observed. Cylindrical arrays of circumferentially and axially oriented dipoles are compared with a planar array of same size in E-plane for array sizes of 7x7, 11x11 and 15x15. The cylinder radius is $a = 4\lambda_0$ and the thickness of the dielectric coating is $t_h = 0.06\lambda_0$. As the array size increases, the surface waves become stronger which causes the elements of the array to have larger reflection coefficients. At $(90 - \theta) = 54°$, scan blindness occur for the 15x15 cylindrical array of

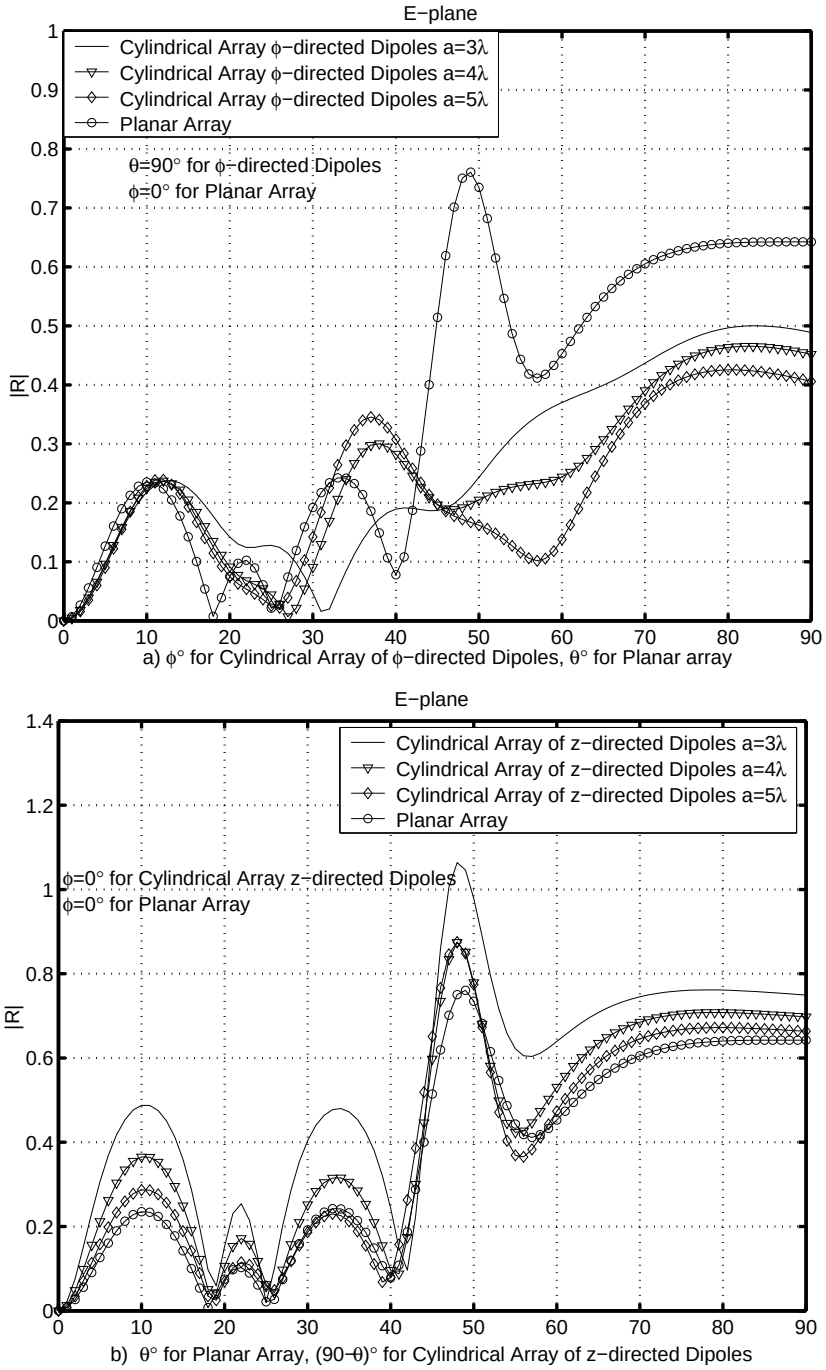

Figure 4.12: Magnitude of reflection coefficient of the middle element vs. scan angle for different radii of a 11x11 cylindrical array of a) circumferentially oriented b) axially oriented dipoles and comparison with a 11x11 planar array in E-Plane ($l_{dip} = 0.39\lambda_0$, $w_{dip} = 0.01\lambda_0$, $d_z = d_{rl} = d_x = d_y = 0.5\lambda_0$, $t_h = 0.06\lambda_0$, $\epsilon_r = 3.25$).

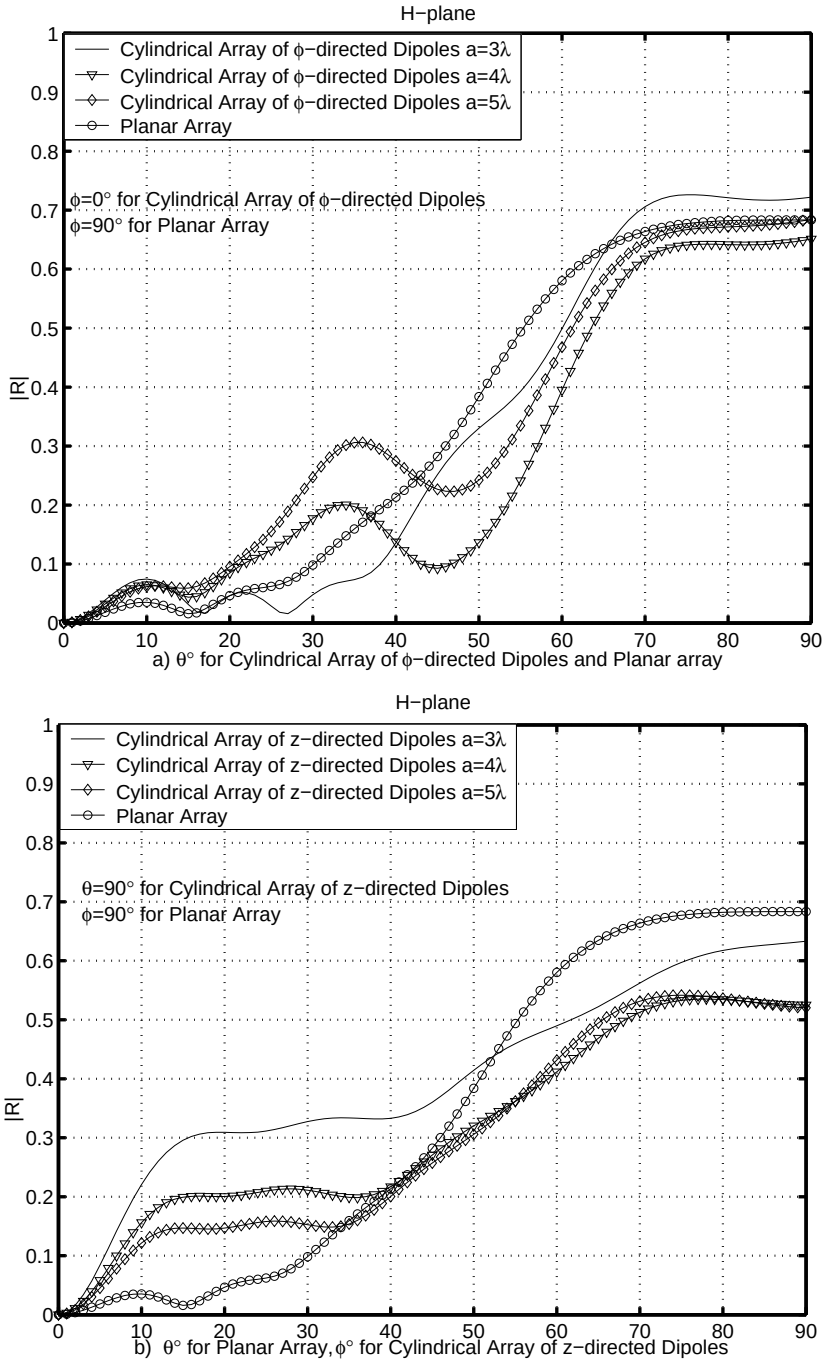

Figure 4.13: Magnitude of reflection coefficient of the middle element vs. scan angle for different radii of a 11x11 cylindrical array of a) circumferentially oriented and b) axially oriented dipoles and comparison with a 11x11 planar array in H-Plane ($l_{dip} = 0.39\lambda_0$, $w_{dip} = 0.01\lambda_0$, $d_z = d_{rl} = d_x = d_y = 0.5\lambda_0$, $t_h = 0.06\lambda_0$, $\epsilon_r = 3.25$).

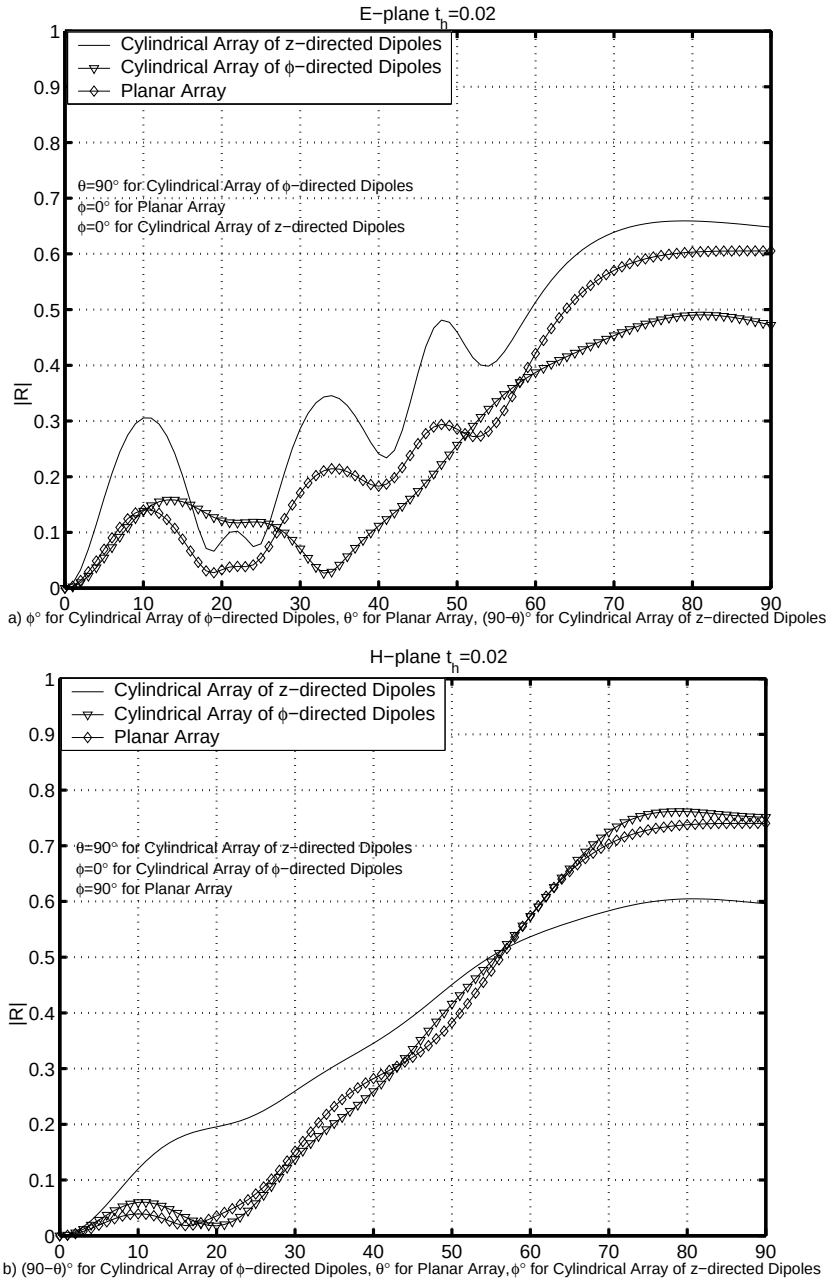

Figure 4.14: Magnitude of reflection coefficient of the middle element vs. scan angle comparison for 11x11 cylindrical arrays of circumferentially and axially oriented dipoles and comparison with a 11x11 planar array in a) E-Plane and b) H-Plane ($l_{dip} = 0.39\lambda_0$, $w_{dip} = 0.01\lambda_0$, $d_z = d_{rl} = d_x = d_y = 0.5\lambda_0$, $a = 3\lambda_0$, $t_h = 0.02\lambda_0$, $\epsilon_r = 3.25$).

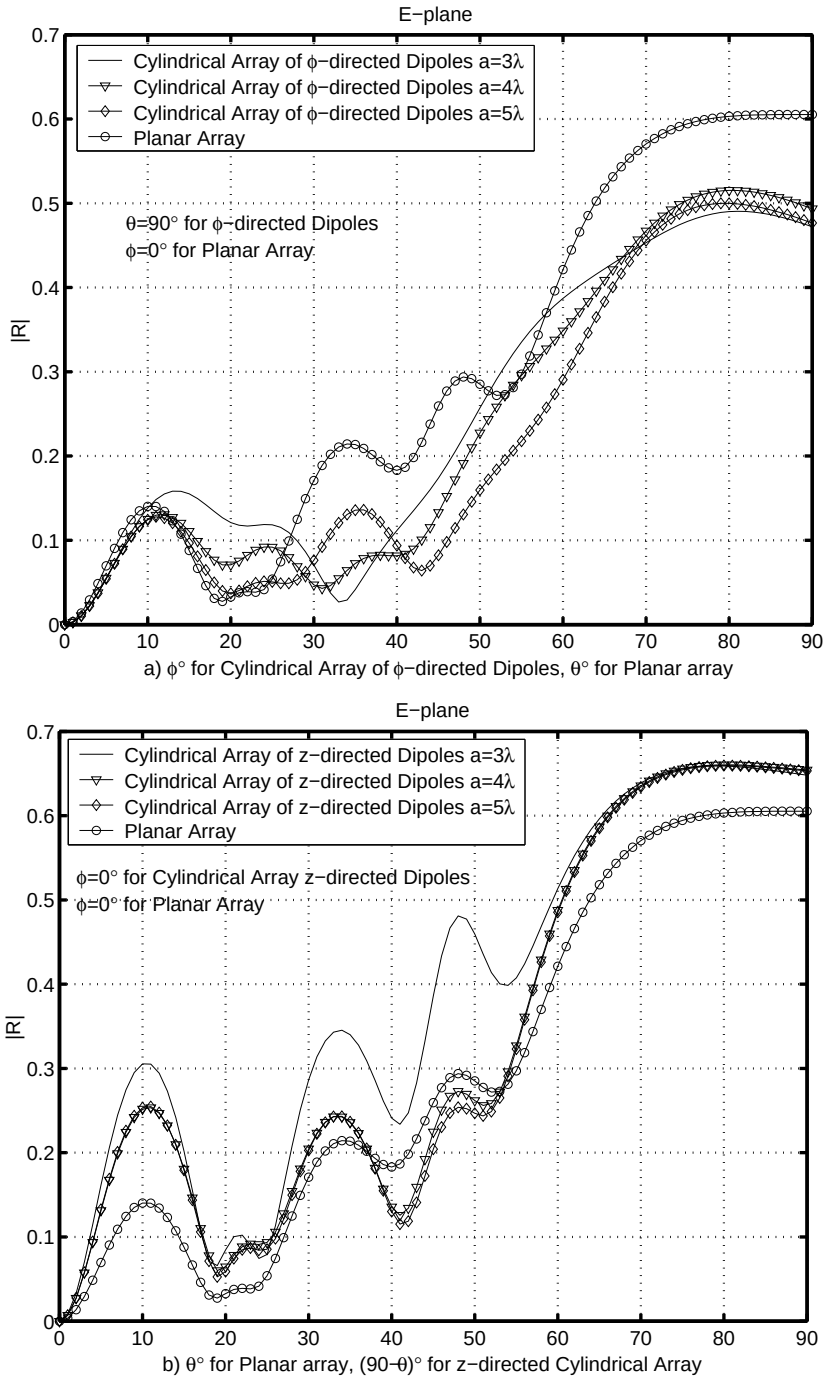

Figure 4.15: Magnitude of reflection coefficient of the middle element vs. scan angle for different radii of a 11x11 cylindrical array of a) circumferentially oriented b) axially oriented dipoles and comparison with a 11x11 planar array in E-Plane ($l_{dip} = 0.39\lambda_0$, $w_{dip} = 0.01\lambda_0$, $d_z = d_{rl} = d_x = d_y = 0.5\lambda_0$, $t_h = 0.02\lambda_0$, $\epsilon_r = 3.25$)).

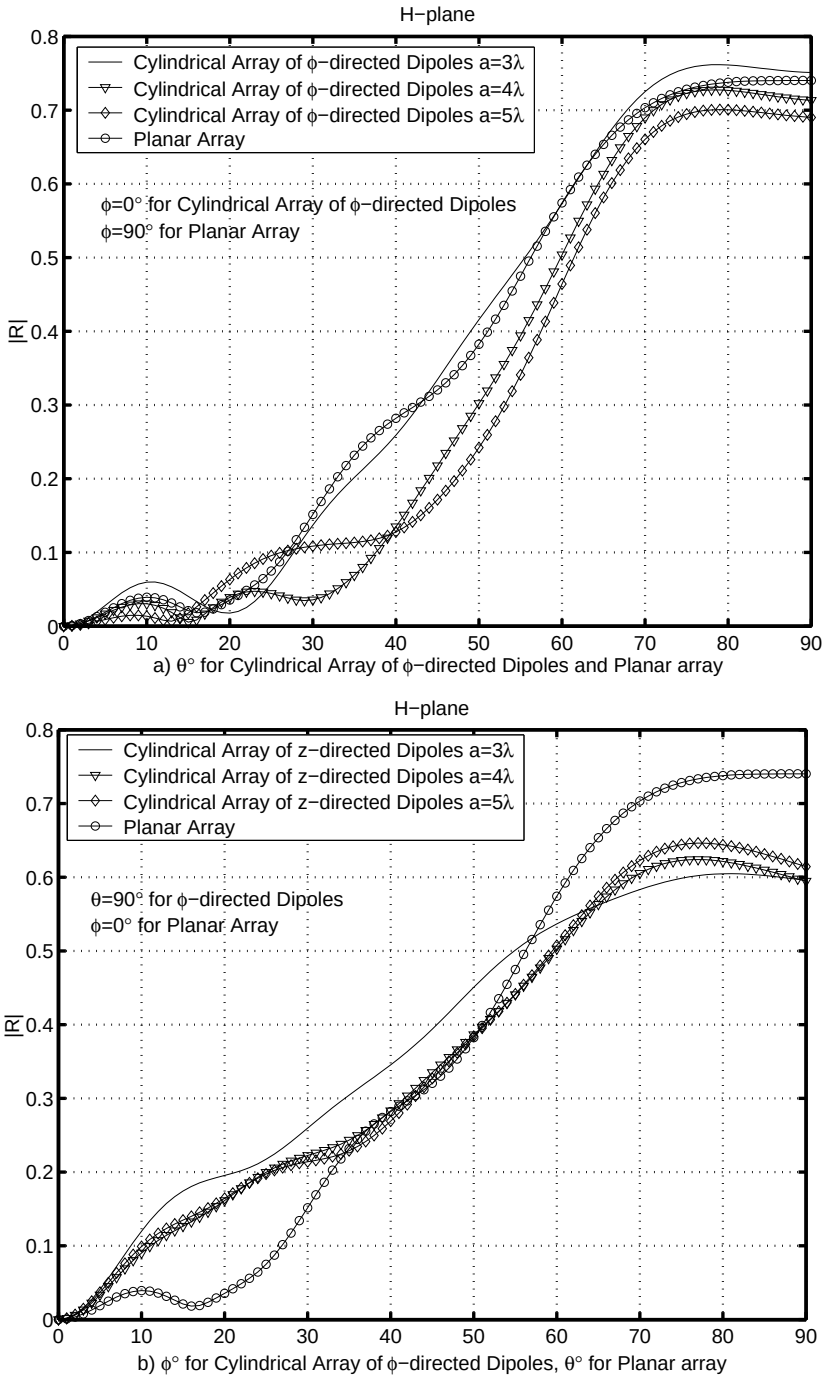

Figure 4.16: Magnitude of reflection coefficient of the middle element vs. scan angle for different radii of a 11x11 cylindrical array of a) circumferentially oriented and b) axially oriented dipoles and comparison with a 11x11 planar array in H-Plane ($l_{dip} = 0.39\lambda_0$, $w_{dip} = 0.01\lambda_0$, $d_z = d_{rl} = d_x = d_y = 0.5\lambda_0$, $t_h = 0.02\lambda_0$, $\epsilon_r = 3.25$).

axially oriented dipoles. However, reflection coefficient for the cylindrical array of circumferentially oriented dipoles does not change dramatically with the change of the array size due to the curvature and thus the scan blindness does not exist.

For the reflection coefficient's magnitude to be greater than or equal to unity, the input impedance of the antenna elements must have negative or zero real parts, respectively. Therefore, the dipoles are open-circuited at scan blindness and hence the array behavior closely resemble a grounded cylindrical dielectric without any printed dipoles on its surface ([42]). The contour of the input impedance is shown in Figures 4.18 (11x11 array, $a = 3\lambda_0$ and $t_h = 0.06\lambda_0$) and 4.19 (15x15 array, $a = 4\lambda_0$ and $t_h = 0.06\lambda_0$) for the two cases, where (it is previously found that) the scan blindness occurs for cylindrical arrays of axially oriented dipoles. As expected, the real part of the input impedance becomes negative around the angle of scan blindness for the cylindrical array of axially oriented dipoles while the real part of the input impedance is always positive for the cylindrical array of circumferentially oriented dipoles.

As explained in section 3.4 in finite arrays, as oppose to the infinite arrays, only certain elements have reflection coefficients whose magnitudes are greater than or equal to unity at the scan blindness angle. This is illustrated in Figure 4.20, where the active reflection coefficient versus the element number is plotted for a 15x15 cylindrical array of circumferentially oriented dipoles at $(\theta = 90°, \phi = 54°)$, 15x15 cylindrical array of axially oriented dipoles at $(\theta = 36°, \phi = 0°)$ and 15x15 planar array at $(\theta = 54°, \phi = 0°)$ with the parameters $a = 4\lambda_0$ and $t_h = 0.06\lambda_0$. From the conservation of power principle, power must be delivered to these elements with reflection coefficients whose magnitudes are greater than unity from the other elements. For the cylindrical array of circumferentially directed dipoles it is seen that reflection coefficients' magnitudes do not exceed unity for any of the elements.

The normalized far-field patterns for 11x11 cylindrical arrays of circumferentially oriented dipoles with different radii and a 11x11 planar array scanned along E-plane is shown in Figure 4.21. The thickness of the cylinder is $t_h = 0.06\lambda_0$. The main beam is in the broadside direction in 4.21-a. Along the main beam, the

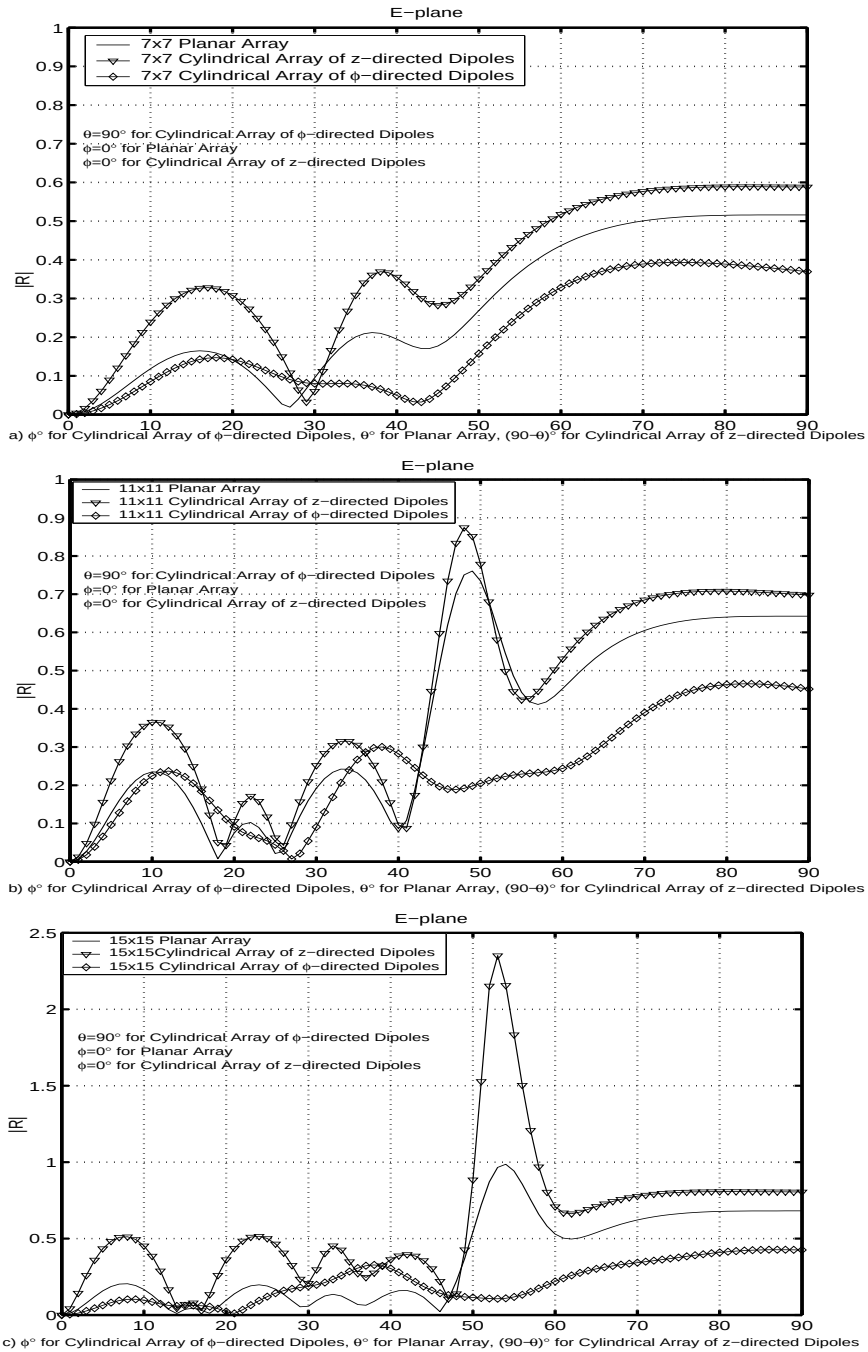

Figure 4.17: Magnitude of reflection coefficient of the middle element vs. scan angle comparison for a) 7x7, b) 11x11 and c) 15x15 cylindrical arrays of circumferentially and axially oriented dipoles and the planar array in E-Plane ($l_{dip} = 0.39\lambda_0$, $w_{dip} = 0.01\lambda_0$, $d_z = d_{rl} = d_x = d_y = 0.5\lambda_0$, $a = 4\lambda_0$, $t_h = 0.06\lambda_0$, $\epsilon_r = 3.25$).

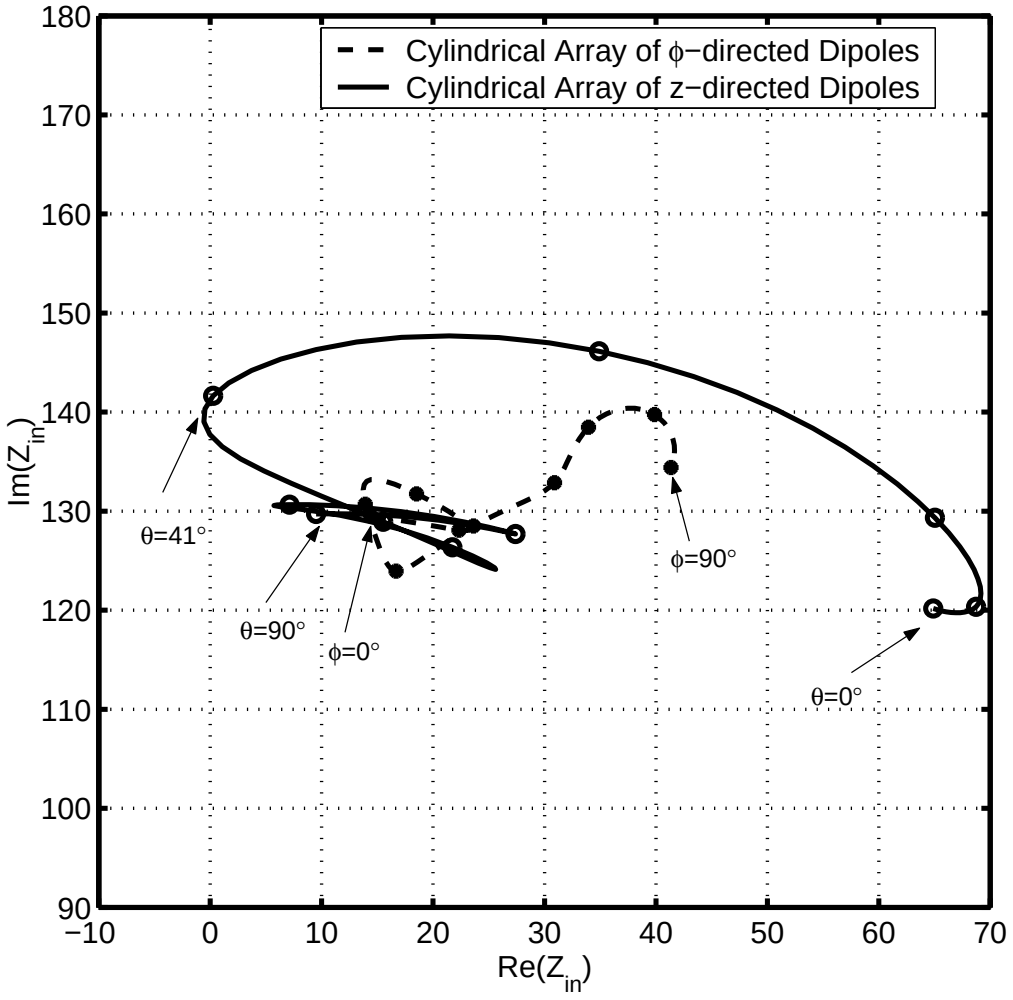

Figure 4.18: Change of input impedance of the middle element w.r.to scan angle for 11x11 cylindrical arrays of circumferentially and axially oriented dipoles ($l_{dip} = 0.39\lambda_0$, $w_{dip} = 0.01\lambda_0$, $d_z = d_{rl} = d_x = d_y = 0.5\lambda_0$, $a = 3\lambda_0$, $t_h = 0.06\lambda_0$, $\epsilon_r = 3.25$).

pattern of the planar array and the cylindrical array are very close to each other. However, away from the main lobe the shape of the patterns loses their similarity due to the curvature effects. Again, when the radius of the cylinder is increased the patterns of planar and cylindrical arrays gets more similar. For cylindrical arrays, high sidelobe levels are obtained in the pattern compared to planar array. This is because some of the element patterns have their peaks other than the intended scan direction due to the curvature on a cylindrical array. When the

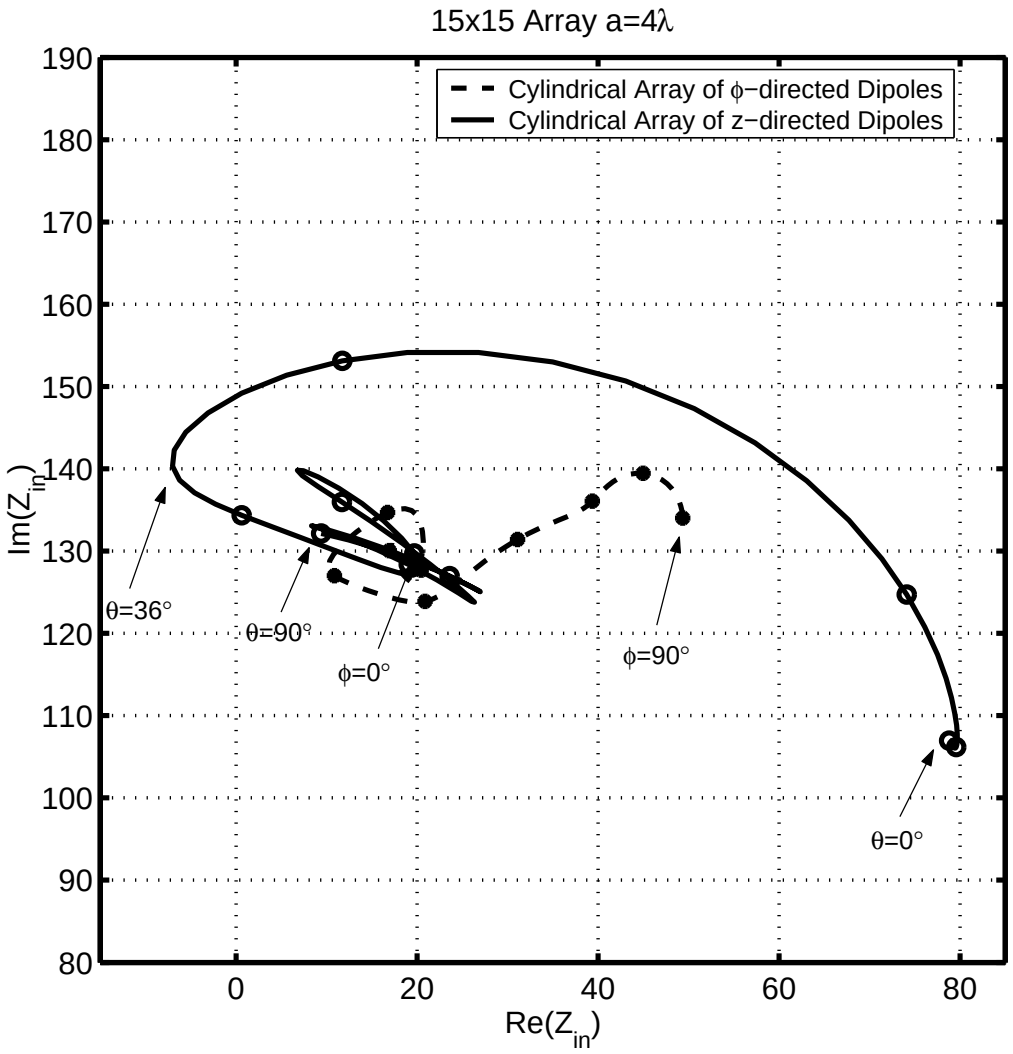

Figure 4.19: Change of input impedance of the middle element wrt. scan angle for 15x15 cylindrical arrays of circumferentially and axially oriented dipoles ($l_{dip} = 0.39\lambda_0$, $w_{dip} = 0.01\lambda_0$, $d_z = d_{rl} = d_x = d_y = 0.5\lambda_0$, $a = 4\lambda_0$, $t_h = 0.06\lambda_0$, $\epsilon_r = 3.25$).

cylinder radius is decreased, the curvature effect increases which explains why the cylinder with $a = 3\lambda_0$ has the highest sidelobe level. In Figure 4.21-b, the scan angle is set to 60°. For the cylindrical arrays, the main beam direction is slightly less than 60° due to the different peak directions of the elements on a curved surface. In Figure 4.22 the results of 4.21 are obtained for a cylindrical array of axially oriented dipoles instead of the cylindrical arrays of circumferentially

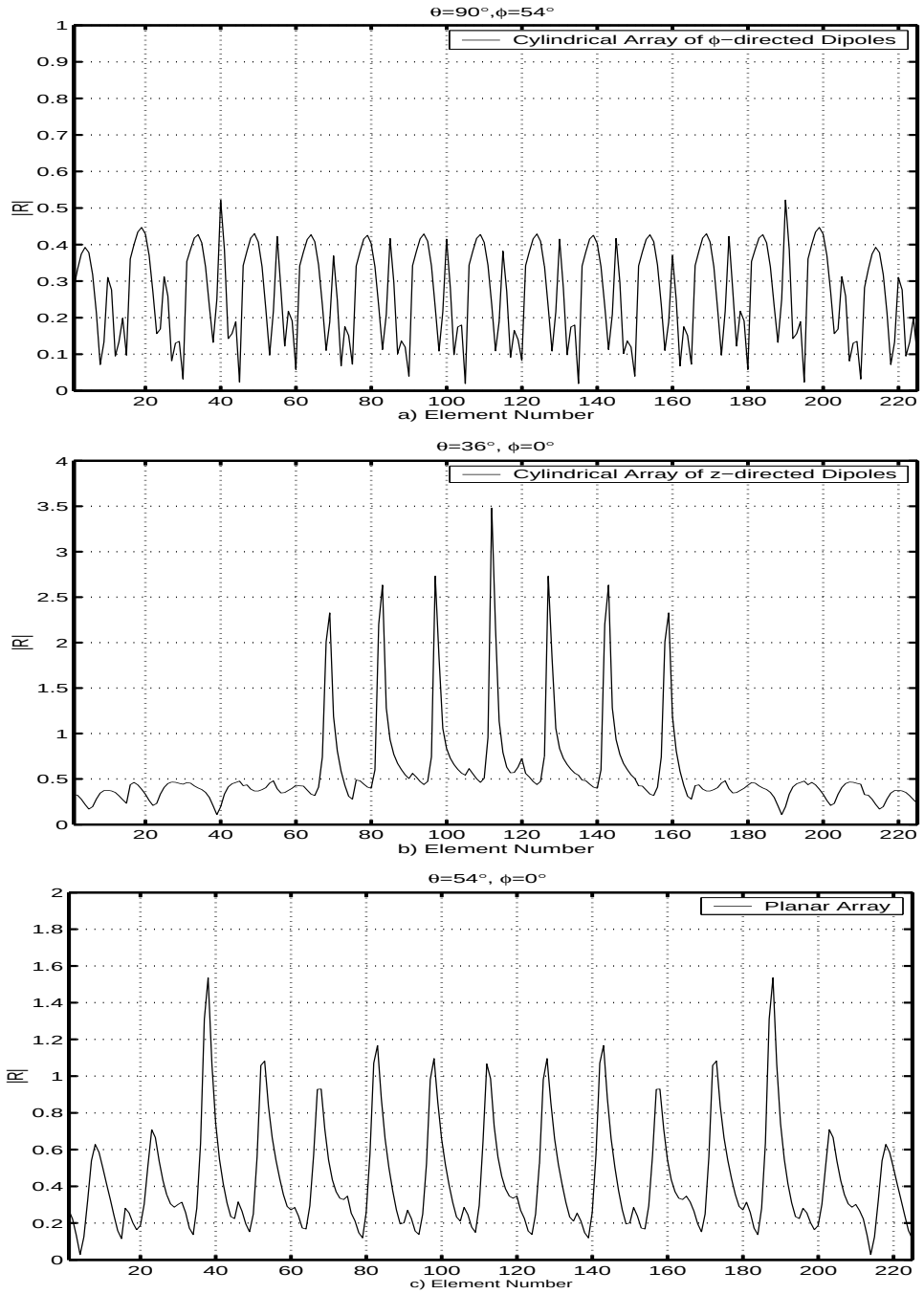

Figure 4.20: Magnitude of the reflection coefficient vs. element number of a) 15x15 cylindrical array of circumferentially oriented dipoles b) 15x15 cylindrical array of axially oriented dipoles and c) 15x15 planar array ($l_{dip} = 0.39\lambda_0$, $w_{dip} = 0.01\lambda_0$, $d_z = d_{rl} = d_x = d_y = 0.5\lambda_0$, $a = 4\lambda_0$, $t_h = 0.06\lambda_0$, $\epsilon_r = 3.25$).

oriented dipoles and H-plane scanning instead of scanning in the E-plane such that the scan is in the circumferential direction for both figures. The sidelobe level in this case is lower than its cylindrical array of circumferentially oriented dipoles counterpart and the pattern more closely resembles the pattern of the planar array. As mentioned before, the coupling for large separations is weak in the H-plane of the cylindrical array of axially oriented dipoles. Hence, predominantly central elements of the array is important in the shaping of the pattern and as a result sidelobe levels are not that high.

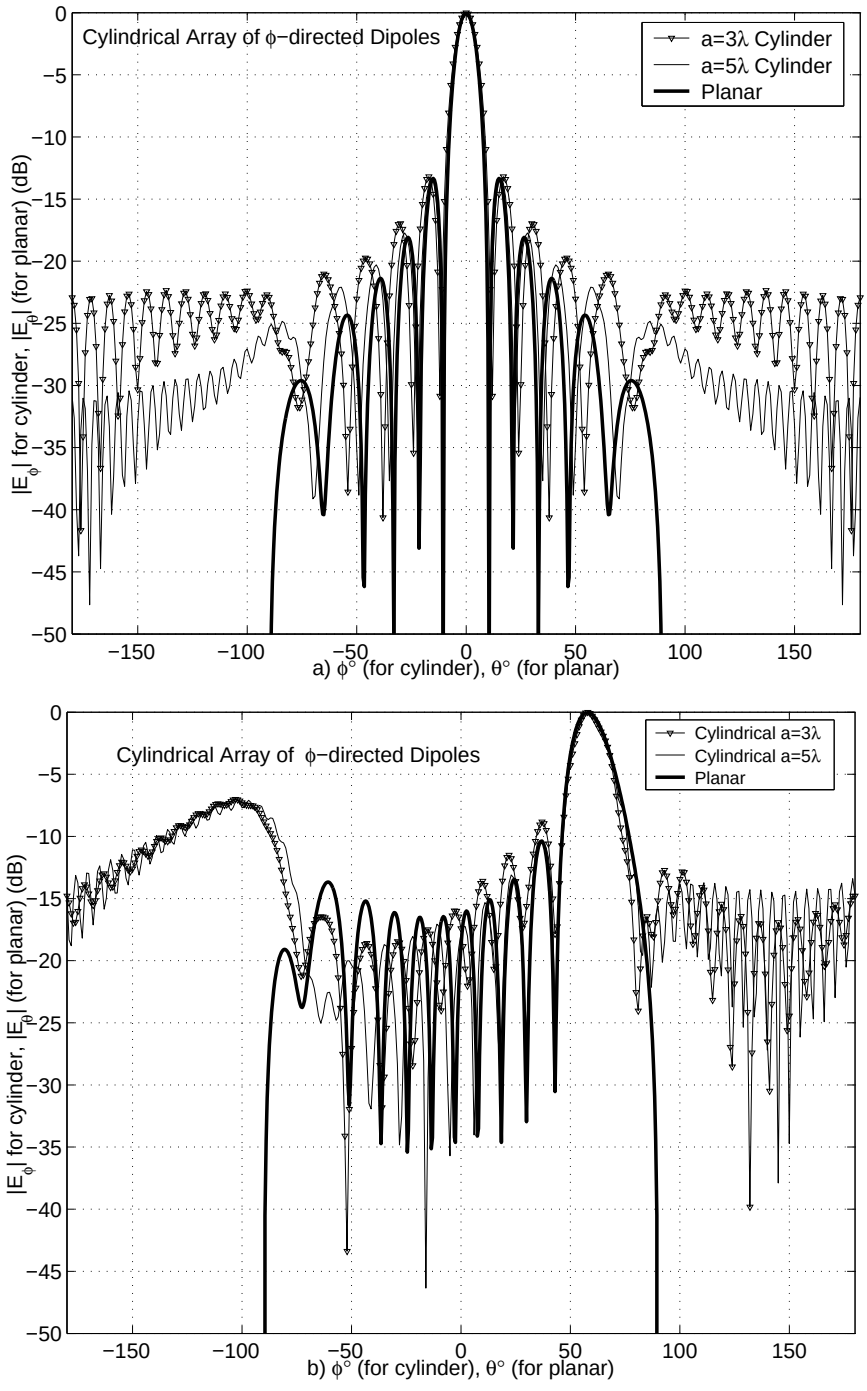

Figure 4.21: Far-field pattern for different radii of a 11x11 cylindrical array of circumferentially oriented printed dipoles and comparison with the planar array for a) broadside and b) 60° scan ($l_{dip} = 0.39\lambda_0$, $w_{dip} = 0.01\lambda_0$, $d_z = d_{rl} = d_x = d_y = 0.5\lambda_0$, $t_h = 0.06\lambda_0$, $\epsilon_r = 3.25$).

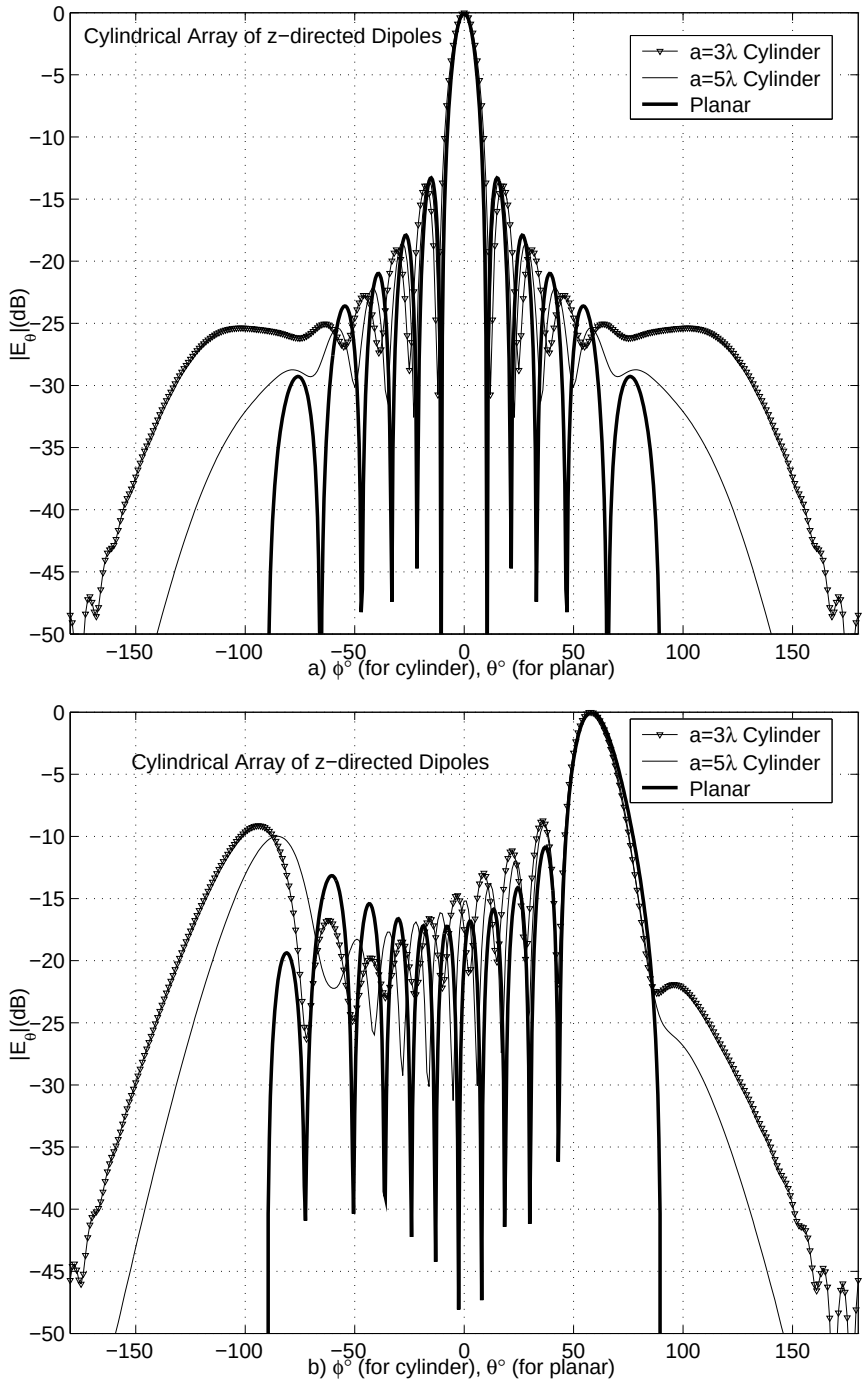

Figure 4.22: Far-field pattern for different radii of a 11x11 cylindrical array of axially oriented printed dipoles and comparison with the planar array for a) broadside scan and b)(60° scan) ($l_{dip} = 0.39\lambda_0$, $w_{dip} = 0.01\lambda_0$, $d_z = d_{rl} = d_x = d_y = 0.5\lambda_0$, $t_h = 0.06\lambda_0$, $\epsilon_r = 3.25$).

Chapter 5

Conclusions

In this thesis, finite, phased arrays of circumferentially oriented printed dipoles conformal to electrically large, coated cylinders are analyzed using the hybrid MoM/Green's method function in the spatial domain. Although these arrays finds prominent usage in the shipborne, airborne and wireless communications applications where conformality is a major issue, there is a lack of efficient and accurate design tools which provides a motivation for this research. A review of the Hybrid MoM/Green's function method in spatial domain developed in [23] is provided in this work. In this method, the appropriate Green's function is the kernel of the EFIE equation which is solved via MoM and possesses the electrical and geometrical properties of the host body. Since, the efficiency and the accuracy of the method relies on the computation of Green's functions, three different high frequency based Green's function representations, which are valid in different but overlapping regions of the cylinder surface, are used interchangeably to achieve this goal. The switching algorithm that leads to the computationally optimum results are explained. Modifications on the method to obtain more accurate results including the revision of the tail integral for the SDP representation and analysis of the possible integration contours are given. Several basic performance metrics are defined and their meanings are explained. The scan blindness phenomenon is described and studies that have been reported previously on this subject are narrated.

Numerical results are presented to assess the accuracy of the Hybrid MoM/Green's function method in the spatial domain and to investigate performance of finite, phased arrays of circumferentially oriented dipoles on electrically large, coated cylinders. The accuracy of the hybrid MoM/Green's function in the spatial domain method has been proven by comparing the mutual coupling and induced current envelope results obtained with those of the spectral domain solutions. This comparison is done for small arrays and/or electrically small separations between source and observation points due to the convergence problems of the spectral domain solution for electrically large cylinders. Then, performance of cylindrical array of circumferentially oriented dipoles is compared to that of cylindrical array of axially oriented dipoles and planar array of printed dipoles with the aid of basic performance metrics. In the current and reflection versus scan results, it is seen that, especially in the circumferential direction where curvature effects become dominant, the reflection characteristics of a cylindrical array differs greatly from that of the planar array. Thus, using a planar array to approximate a cylindrical array is not possible for applications where accuracy is a concern. The change of the system performance with respect to array and host body parameters including array size, radius of the cylinder and the thickness of the dielectric coating are also observed. Special attention is paid to scan blindness phenomenon. This work has been the first study of scan blindness on finite, phased arrays of printed dipoles on electrically large, coated cylinders to the best of my knowledge. It is shown that both array and host body parameters affect the scan blindness. This study also show the importance of the orientation of the dipoles on the scan blindness. According to these results, scan blindness may not occur for cylindrical arrays of circumferentially oriented dipoles while both cylindrical arrays of axially oriented dipoles and planar arrays exhibit it. Hence, the properties of the array elements also affect the scan blindness for cylindrical arrays unlike their planar counterparts.

Appendix A

FS Representation for the G_{zz} Component

A.1 The Derivation of the Surface Fields using Fourier Series for the G_{zz} Component

The G_{zz} component of the Green's function can be expanded as a Fourier Series using its periodicity with respect to ψ as given in (2.64) as follows :

$$G_{zz}(\zeta,\psi) = a_0(\zeta) + \sum_{n=1}^{\infty} a_n(\zeta) cosn2\psi + \sum_{n=1}^{\infty} b_n(\zeta) sinn2\psi \tag{A.1}$$

where

$$a_0(\zeta) = \frac{1}{\pi}\int_T G_{lu}(\zeta,\psi)d\psi \tag{A.2}$$

$$a_n(\zeta) = \frac{2}{\pi}\int_T G_{lu}(\zeta,\psi) cosn2\psi d\psi \tag{A.3}$$

$$b_n(\zeta) = \frac{2}{\pi}\int_T G_{lu}(\zeta,\psi) sin2\psi d\psi \tag{A.4}$$

and $\omega_0 = 2\pi$.

By using the trapezoidal rule to evaluate the Fourier Series' coefficients, the approximate result for the G_{zz} component of the Green's function is found ([23]) as

$$\begin{aligned} G^a_{zz}(\zeta,\psi) &\approx G_{zz}(\zeta,\psi=\frac{\pi}{2}) \\ &\quad + \left[G_{zz}(\zeta,\psi=0) - G_{zz}(\zeta,\psi=\frac{\pi}{2})\right]\left(\frac{1+cos2\psi}{2}\right). \end{aligned} \tag{A.5}$$

Substituting (A.5) into (2.63), the surface field for the G_{zz} component can be written as:

$$\begin{aligned} E_{zz}(\delta,s) &\approx \frac{1}{2\pi}\Bigg[\int_0^\infty G_{zz}(\zeta,\psi=\frac{\pi}{2})\left\{\int_0^{2\pi}\frac{e^{j\zeta scos(\psi-\delta)}}{2\pi}d\psi\right\}\zeta d\zeta + \int_0^\infty \Big(G_{zz}(\zeta,\psi=0) \\ &\quad -G_{zz}(\zeta,\psi=\frac{\pi}{2})\Big)\left\{\int_0^{2\pi}\left(\frac{1+cos2\psi}{4\pi}\right)e^{j\zeta scos(\psi-\delta)}d\psi\right\}\zeta d\zeta\Bigg] \end{aligned} \tag{A.6}$$

A.2 Evaluation of the integrals with variable ψ

The integrals with the integral variable ψ in the equations (2.69) and (A.6) can be evaluated analytically ([23]), i.e.

$$\int_0^{2\pi}\frac{e^{j\zeta scos(\psi-\delta)}}{2\pi}d\psi = J_0(\zeta,s) \tag{A.7}$$

$$\int_0^{2\pi}\left(\frac{1-cos2\psi}{4\pi}\right)e^{j\zeta scos(\psi-\delta)}d\psi = -\frac{1}{\zeta^2}\frac{\partial^2}{\partial r_l^2}J_0(\zeta s) \tag{A.8}$$

$$\int_0^{2\pi} \left(\frac{1 + cos2\psi}{4\pi} \right) e^{j\zeta scos(\psi-\delta)} d\psi = -\frac{1}{\zeta^2} \frac{\partial^2}{\partial z^2} J_0(\zeta s) \tag{A.9}$$

$$\int_0^{2\pi} \frac{sin2\psi}{4\pi} e^{j\zeta scos(\psi-\delta)} d\psi = -\frac{1}{\zeta^2} \frac{\partial^2}{\partial z \partial r_l} J_0(\zeta s) \tag{A.10}$$

where $J_0(\zeta, s)$ is the Bessel function of order zero.

Appendix B

Evaluation of Special Functions

In Section 2.3, some special functions are defined in equations (2.26)-(2.28) that are used in the evaluation of the components of the Green's function. Bessel and Hankel functions are used in these definitions, which raise some numerical problems in their computation. First of all, there are different representations for the Bessel and Hankel functions which are valid in different regions. Hence, it is necessary to switch between different representations to compute Bessel and Hankel functions accurately. Also, when the order or the argument of the Bessel and Hankel functions gets large or become complex, their evaluation becomes a tedious task. Therefore, several approximations are developed in the evaluation of the special functions R_ν, C_ν^e and C_ν^m in [23] which are explained in here.

B.1 Approximations for R_v

In the equation (2.26), R_ν was defined as follows:

$$R_\nu = \frac{H_\nu^{(2)'}(z)}{H_\nu^{(2)}(z)}. \tag{B.1}$$

If this function is evaluated directly by first finding the derivative of the Hankel function of the second kind ($H_\nu^{(2)'}(z)$) and dividing by $H_\nu^{(2)}(z)$, convergence problems are observed for large order and/or large argument values. Instead of this, one can obtain a formula for R_ν by taking the ratio of the approximations used for the Hankel functions like Debye and Olver approximations.

The use of Debye approximations to find an approximate formula to R_ν is explained in [33]. The Debye approximations for $J_\nu(z)$ and $Y_\nu(z)$ and their derivatives with respect to the argument by taking the first two terms in the corresponding series are repeated here for convenience as

$$J_\nu(z) \approx \frac{e^{(\sqrt{\nu^2-z^2}-\nu\, cosh^{-1}(\nu/z))}}{\sqrt{2\pi}(\nu^2-z^2)^{1/4}}\left[1+\frac{u_1(\nu/\sqrt{\nu^2-z^2})}{\nu}\right] \tag{B.2}$$

$$Y_\nu(z) \approx -\frac{e^{-(\sqrt{\nu^2-z^2}-\nu\, cosh^{-1}(\nu/z))}}{\sqrt{\pi/2}(\nu^2-z^2)^{1/4}}\left[1-\frac{u_1(\nu/\sqrt{\nu^2-z^2})}{\nu}\right] \tag{B.3}$$

$$J'_\nu(z) \approx \frac{(\nu^2-z^2)^{1/4}}{\sqrt{2\pi}z}e^{(\sqrt{\nu^2-z^2}-\nu\, cosh^{-1}(\nu/z))}\left[1+\frac{v_1(\nu/\sqrt{\nu^2-z^2})}{\nu}\right] \tag{B.4}$$

$$Y'_\nu(z) \approx \frac{(\nu^2-z^2)^{1/4}}{\sqrt{\pi/2}z}e^{-(\sqrt{\nu^2-z^2}-\nu\, cosh^{-1}(\nu/z))}\left[1-\frac{v_1(\nu/\sqrt{\nu^2-z^2})}{\nu}\right] \tag{B.5}$$

where

$$u_1(t) = \frac{3t-5t^2}{24} \tag{B.6}$$

$$v_1(t) = \frac{-9t+7t^3}{24}. \tag{B.7}$$

Using Debye approximations in equation (B.1) gives

$$R_\nu \approx -\frac{j\sqrt{z^2-\nu^2}}{z} - \frac{z}{2\left(z^2-\nu^2\right)}. \tag{B.8}$$

It should be noted that when $|\nu| > |z|$, the correct choice of branch for the square-root function is

$$\sqrt{z^2-\nu^2} = -j\sqrt{\nu^2-z^2}. \tag{B.9}$$

The Olver approximation for the $H_\nu^{(2)}(z)$ and its derivative with respect to the argument are given in [37] as follows:

$$H_\nu^{(2)}(z) \approx 2e^{j\pi/3}\gamma(\nu,z)\frac{A_i(e^{-j2\pi/3}\nu^{2/3}\zeta)}{\nu^{1/3}} \tag{B.10}$$

$$H_\nu^{(2)'}(z) \approx \frac{4e^{-j2\pi/3}}{z/\nu}\frac{1}{\gamma(\nu,z)}\frac{e^{-j2\pi/3}A_i'(e^{-j2\pi/3}\nu^{2/3}\zeta)}{\nu^{2/3}} \tag{B.11}$$

where ζ and γ are defined as

$$\zeta = (1.5\rho)^{2/3} \tag{B.12}$$

$$\rho = Ln\left(1+\sqrt{1-\left(\frac{z}{\nu}\right)^2}\right) - Ln\left(\frac{z}{\nu}\right) - \sqrt{1-\left(\frac{z}{\nu}\right)^2} \tag{B.13}$$

$$\gamma = \left(\frac{4\zeta}{(1-(\frac{z}{\nu})^2)}\right). \tag{B.14}$$

Therefore, the resulting expression for R_ν is

$$R_\nu \approx \frac{A_i'(x)}{A_i(x)}\frac{1}{\nu^{1/3}}\frac{e^{j\pi/3}}{\left[\frac{(\frac{z}{\nu})^2\zeta}{1-(\frac{z}{\nu})^2}\right]^{1/2}} \tag{B.15}$$

where ζ and ρ are defined in equations (B.12),(B.13) and x is given by

$$x = \zeta \nu^{2/3} e^{-j2\pi/3}. \tag{B.16}$$

The proper choice of branches in equations (B.12), (B.13) and (B.16) is not a trivial matter and explained in depth in [37]. Equation (B.8) is easier to compute but there is a small region that it is not valid where (B.15) is used.

B.2 Approximations for C_v^e and C_v^m

In the evaluation of C_v^e and C_v^m, Debye approximations given by (B.2)-(B.7) are used as explained in [33]. The resulting expressions are

$$\begin{aligned} C_v^e \approx & -\frac{\sqrt{k_{t1}^2 - (\nu/d)^2}}{cot(th\sqrt{k_{t1}^2 - (\nu/d)^2})} \\ & + \frac{1}{2d}\left\{ \frac{k_{t1}^2}{k_{t1}^2 - (\nu/d)^2} - \frac{th^2(\nu/d)^2}{sin^2(th\sqrt{k_{t1}^2 - (\nu/d)^2})} \right\} \end{aligned} \tag{B.17}$$

and

$$\begin{aligned} C_v^m \approx & \frac{\sqrt{k_{t1}^2 - (\nu/d)^2}}{tan(th\sqrt{k_{t1}^2 - (\nu/d)^2})} \\ & - \frac{1}{2d}\left\{ \frac{k_{t1}^2 tan^2(th\sqrt{k_{t1}^2 - (\nu/d)^2})}{k_{t1}^2 - (\nu/d)^2} + \frac{th^2(\nu/d)^2}{cos^2(th\sqrt{k_{t1}^2 - (\nu/d)^2})} \right\} \end{aligned} \tag{B.18}$$

Debye approximations are found to give accurate results for all values of ν, hence no other approximations are needed for C_ν^e and C_ν^m. Also it should be noted that there are no branch-cuts for these equations.

Bibliography

[1] R. C. Hansen, *Phased Array Antennas.*, John Wiley & Sons, Inc. New York 1998.

[2] R. J. Mailloux, *Phased Array Antenna Handbook.*, Artech House, Inc. Boston 1994.

[3] R. J. Mailloux, "Guest editorial special issue on phased arrays", *IEEE Trans. Antennas and Propagat.*, vol. 47, pp. 413-415, Mar. 1999.

[4] Y. T. Lo and S. W. Lee, *Antenna Handbook*, Van Nostrand Reinhold Company, New York 1988.

[5] G. V. Borgiotti and Q. Balzano, "Mutual coupling analysis of a conformal array of elements on a cylindrical surface", *IEEE Trans. Antennas and Propagat.*, vol. 18, pp. 55-63, Jan. 1970.

[6] G. E. Stewart, and K. E. Golden, "Mutual admittance for axial rectangular slots in a large conducting cylinder", *IEEE Trans. Antennas and Propagat.*, vol. 19, pp. 120-122, Jan. 1971.

[7] J. Shapira, L. B. Felsen, and A. Hessel, "Ray analysis of conformal antenna arrays", *IEEE Trans. Antennas and Propagat.*, vol. 22, pp. 49-63, Jan. 1974.

[8] J. K. Hsiao and J. B. L. Rao, "Computer analysis of conformal phased arrays", NRL Rep. 7826, Nov. 1974.

[9] K. L. Wong, Y. H. Liu, and C. Y. Huang, "Generalized transmission line model for cylindrical rectangular microstrip antenna", *Microwave and Optical Technology Letters*, vol. 7, pp. 729-732, 1994.

[10] C. Y. Huang, Y. H. Liu, and K. L. Wong, "Input impedance calculation of cylindrical rectangular microstrip antennas using GTLM theory", *IEEE Antennas and Propagation Society International Symposium Digest*, vol. 4, pp. 1792-1795, June 1995.

[11] C. M. Krowne, "Cylindrical-rectangular microstrip antenna", *IEEE Trans. Antennas and Propagat.*, vol. 31, pp. 194-199, Jan. 1983.

[12] J . S. Dahele, R. J. Mitchell, K. M. Luk, and K. F. Lee , "Effect of curvature on characteristics of rectangular patch antenna", *Electron. Letters*, vol. 23, pp. 748-749, July 1987.

[13] K. M. Luk, and K. F. Lee, "Characteristics of the cylindrical-circular patch antenna", *IEEE Trans. Antennas and Propagat.*, vol. 37, pp. 119-123, Feb. 1989.

[14] W. Yu, N. Farahat, and R. Mittra, "Application of FDTD method to conformal patch antennas", *IEE Proceedings- Microwaves, Antennas and Propagation*, vol. 148, issue: 3, pp. 218-220, June 2001.

[15] J. M. Jin, J. A. Berrie, R. Kipp and S. W. Lee, "Calculation of rediatiion patterns of microstrip antennas on cylindrical bodies of arbitrary cross-section", *IEEE Trans. Antennas and Propagat.*, vol. 45, pp. 126-132, Jan. 1997.

[16] L. C. Kempel and J. L. Volakis, "Scattering by cavity-baked antennas on a circular cylinder", *IEEE Trans. Antennas and Propagat.*, vol. 42, pp. 1268-1278, Sept. 1994.

[17] A. J. Sangster and R. T. Jacobs, "Mutual coupling in conformal microstrip patch antenna arrays", *IEE Proceedins-Microwave, Antennas and Propagation*, vol. 150, issue:4, pp. 191-196, Aug. 2003.

[18] J. Liu and J. M. Jin, "Analysis of conformal antennas on a complex platform", *Microwave and Optical Technology Letters*, vol. 36, no. 2, pp. 139-142, 2003.

[19] N. K. Uzunoglu, P. L. E. Uslenghi, and N. G. Alexopoulos, "Printed circuit antennas on cylindrical substrates", *IEEE Antennas and Propagat. Soc. Int. Symp.*, May 1982.

[20] A. Nakatini, N. G. Alexopoulos, N. K. Uzunoglu, and P. L. E. Uslenghi, "Accurate Green's function computation for printed circuit antennas on cylindrical substrates", *Electromagnetics*, vol. 6, pp. 243-254, July-Sept. 1986.

[21] S. M. Ali, T. M. Habashy, J. F. Kiang, and J. A. Kong, "Cylindrical-rectangular and wrap-around microstrip structures", *IEEE Trans. Microwave Theory Tech.*, vol. 37, pp. 1773-1782, Nov. 1989.

[22] T. M. Habashy, S. M. Ali, and J. A. Kong, "Input impedance and radiation pattern of cylindrical-rectangular and wrap-around microstrip antennas", *IEEE Trans. Antennas and Propagat.*, vol. 38, pp. 722-731, May 1990.

[23] V. B. Ertürk,*Efficient Hybrid MoM/Green's Function technique to Analyze Conformal Microstrip Antennas and Arrays*. PhD thesis, The Ohio State University ,2000.

[24] V. B. Ertürk and R. G. Rojas, "Efficient computation of surface fields excited on a dielectric coated circular cylinder", *IEEE Trans. Antennas and Propagat.*, Vol. 48, No.10, pp. 1507-1516, October 2000.

[25] V. B. Ertürk and R. G. Rojas, "Paraxial space-domain formulation for surface fields on a large dielectric coated circular cylinder", *IEEE Trans. Antennas and Propagat.*, Vol. 50, No. 11, pp. 1577-1587, Nov. 2002.

[26] V. B. Ertürk, K. W. Lee and R.G. Rojas, "Analysis of finite arrays of axially oriented printed dipoles on electrically large circular cylinders", accepted to the *IEEE Trans. Antennas and Propagat.*

[27] D. M. Pozar, "Analysis of finite phased arrays of printed dipoles", *IEEE Trans. Antennas and Propagat.*, vol. 33, pp. 602-610, Oct. 1985.

[28] V.B. Ertürk and B. Güner, "Analysis of finite arrays of circumferentially oriented printed dipoles on electrically large cylinders", *Microwave and Optical Technology Letters*, vol. 42, no. 4, pp. 299-304, Aug. 2004.

[29] S. Barkeshli, P. H. Pathak, and M. Marin, "An asymptotic closed-form microstirp surface Green's function for the efficient moment method analysis of mutual coupling in microstrip antennas", *IEEE Trans. Antennas and Propagat.*, vol. 38, pp. 1374-1383, Sept. 1990.

[30] C. Demirdag and R. G. Rojas, "Mutual coupling calculations on a dielectric coated PEC cylinder using UTD-based Green's function", *IEEE AP-S Digest*, vol. 3, pp. 1525-1528, Canada, July 1997.

[31] V. B. Ertürk and R.G. Rojas, "Efficient analysis of input impedance and mutual coupling of microstrip antennas/arrays mounted on large coated cylinders", *IEEE Trans. Antennas and Propagat.*, Vol. 51, No. 4, pp. 739-749, April 2003.

[32] K.-L. Wong, *Design of Nonplanar Microstrip Antennas and Transmission Lines*. New York: Wiley, 1999.

[33] M. Marin and P. H. Pathak, "Calculation of surface fields created by a current distribution on a coated circular cylinder", Tech. rep. 721565-1, The Ohio State University ElectroScience Lab. Dep. of Electrical Engineering, April 1989.

[34] W. H. Press, S. A. Teukolsky, W. T. Vetterling, and B. P. Flanney, *Numerical Recipies in Fortran 77*. New York: Cambridge University Press, 1986.

[35] P. Persson, and R. G. Rojas, "High frequency approximation for mutual coupling calculations between apertures on a PEC circular cylinder covered with a dielectric layer: Non-paraxial region", *Radio Science*, vol. 38, No. 4, 1079, Aug 2003.

[36] P. Persson, B. Thors, and R. G. Rojas, "An improved numerical apporach for surface field calculations on large dielectric coated circular cylinders", TRITA-TET 03-4, June 2003.

[37] R. Paknys, "Evaluation of Hankel functions with complex argument and complex order", *IEEE Trans. Antennas and Propagat.*, vol. 40, pp. 569-578, May 1992.

[38] J.Ashkenazy, S. Shtrikman, and D. Treves, "Electric surface current model for the analysis of microstrip antennas on cylindrical bodies", *IEEE Trans. Antennas and Propagat.*, vol. 33, pp. 295-300, Mar. 1985.

[39] Federal Standart 1037C: Glossary of Telecommunications Terms. The Institute for Telecommunication Sciences. July 2004 <http://www.its.bldrdoc.gov/fs-1037/>.

[40] R. A. Martin and D. H. Werner, "A reciprocity approach for calculating the far-field radiation patterns of a center-fed helical microstrip antenna mounted on a dielectric-coated circular cylinder", *IEEE Trans. Antennas and Propagat.*, vol. 49, pp. 1754-1762, Dec. 2001.

[41] C. A. Balanis, *Antenna Theory Analysis and Design*, John Wiley & Sons, Inc. New York 1997.

[42] D. M. Pozar and D. H. Schaubert, "Scan blindness in infinite phased arrays of printed dipoles", *IEEE Trans. Antennas and Propagat.*, vol. 32, pp. 602-610, Jun. 1984.

[43] H. Schrank and P. D. Patel, "Approximate location of scan-Blindness angle in printed phased arrays", *IEEE Antennas and Propagat. Magazine*, vol. 34, pp. 53-54, Oct. 1992.

[44] R. F. Harrington, *Time Harmonic Electromagnetic Fields.*, New York: McGraw-Hill, 1961.

[45] M. Abramowitz and I. A. Stegun,*Handbook of Mathematical Functions.* New York: Dover Publications, 1970.

[46] B. Güner and V. B. Ertürk, "Analysis of finite arrays of circumferentially oriented printed dipoles on electrically large cylinders", 2003 IEEE International Symposium on Antennas and Propagation and USNC/CNC/URSI North American Radio Science Meeting, Columbus, OH, June 22-27, 2003.

[47] B. Güner and V. B. Ertürk, "Finite phased arrays of printed dipoles on large circular cylinders: a comparison with the planar case", 2004 URSI EMTS

International Conference on Electromagnetics Theory, Pisa-Italy, vol.2, pp. 972-974, May 23-27, 2004.

[48] V.B. Ertürk, R.G. Rojas, and B. Güner, "Scan blindness of conformal phased arrays of printed dipoles", 2004 IEEE AP-S International Symposium and USNC/URSI National Radio Science Meeting, vol. URSI, pp. 4, Monterey, CA, June 20-25, 2004.

[49] B. Güner, V. B. Ertürk, and O. Bakır, "A parametric analysis of finite phased arrays of printed dipoles on large circular cylinders and comparisons with the planar case", 2004 IEEE AP-S International Symposium and USNC/URSI National Radio Science Meeting, vol. 4, pp. 4116-4119, Monterey, CA, June 20-25, 2004.